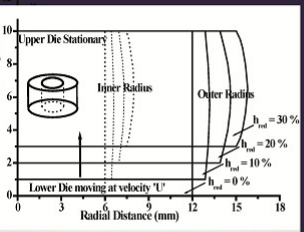

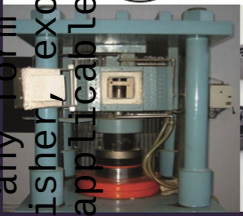

Dr. Saranjit Singh, Ph. D.

MECHANICAL PROCESSING OF SINTERED MATERIALS

PART-1: THEORETICAL ANALYSIS OF SINTER-FORGING PROCESSES

Sciendo

MECHANICAL PROCESSING OF SINTERED MATERIALS

PART-1:
THEORETICAL ANALYSIS
OF SINTER-FORGING PROCESSES

by

Dr. SARANJIT SINGH, Ph.D

School of Mechanical Engineering
KIIT Deemed to be University
Bhubaneswar - 751024 (Odisha), India
2020

ISBN: 978-83-66675-11-7
https://doi.org/10.2478/9788366675124

ACKNOWLEDGMENT

I acknowledge with deep sense of gratitude and profound regards to my guides Dr. S. Kumar and Dr. A.K. Jha for the unlimited support and guidance throughout my research career. Additionally, I am thankful to all my previous colleagues from Department of Production Engineering, BIT Mesra, Ranchi, Jharkhand for their kind co-operation during conduct of the necessary experimental work as shared in the present manuscript.

I also thank my present employer, KIIT Deemed to be University and all my colleagues from KIIT School of Mechanical Engineering for providing me adequate sustenance and inspiration to compile the book.

Last but not the least, I am thankful to my family members for the continuous encouragement to bring up the present book. Without their blessings, the present dream could not have been realized.

(Saranjit Singh)

PREFACE

Mechanical processing of sintered materials in the form of metal powder preforms includes techniques such as sinter-forging, sinter-extrusion, sinter-rolling etc. One technique, which has aroused interest globally for producing high performance components economically, is sinter-forging, which combines the advantages associated with powder metallurgy and conventional forging techniques. The process is attractive because it avoids large number of operations, high scrap losses and energy consumption associated with conventional manufacturing processes. The technology, though have been extensively applied throughout the world for manufacture of numerous components, still requires to be explored from several perspectives.

The objective of the present book is to study, explore and investigate the deformation characteristics during mechanical processing of the sintered materials. The manuscript has been divided into six chapters and considers both theoretical and experimental investigations of the dynamic effects during open-die, flashless closed-die and rotary sinter-forging processes. It also presents the application of Design of Experiment (DOE) and Response Surface Methodology (RSM) techniques for the statistical analysis of sinter-forging processes.

It is expected that the research work presented in the book will be highly useful for the researchers, scientists and practicing engineers in understanding the sinter-forging processes and will assist in carrying further research and development work in the associated field.

CONTENTS

LIST OF FIGURES

LIST OF TABLES

NOMENCLATURE

U_{ij}	associated velocity field
a_{ij}	associated acceleration field
$\dot{\varepsilon}_{ij}$	associated strain rate field
U	die velocity
$\dot{U}$	die acceleration
ΔU	die-workpiece interface relative velocity
t_c	compression time between dies
dz	distance moved by die platen during time t_c
p	die pressure
P_{av}	average die pressure during sinter-forging
F_{av}	average die load during sinter-forging
A_{av}	average cross sectional area of preform
S	surface area
V	volume
W_i	internal energy dissipation
W_f	frictional shear energy dissipation
W_a	inertia energy dissipation
n	constant quantity much greater than unity
η	constant and function of 'ρ_0' only
k, ψ, ν & χ	constant quantities and function of 'η' only
ρ_0	relative density of sintered preform
ρ_i	initial density of preform material
ρ^*	apparent relative density of preform material
μ	coefficient of interfacial friction
ϕ_o	specific cohesion of contact area
τ	interfacial frictional shear stress
σ_0	flow stress of sintered material
σ_m	hydrostatic stress component
β	barreling parameter
ξ	inertia factor
ζ	load factor

J	total external energy supplied by press
J_2'	second invariant of deviator stress
r_m	sticking zone radial distance
x_m	sticking zone axial distance
z_m	sticking zone vertical distance
H_0	initial height of preform
δr	radial bulge of preform vertical surface
C_p	shape factor for hollow preform
C_f	shape factor for truncated conical preform
C_q	shape factor for irregular polygonal preform
r_{hn}	neutral radius of hollow preform
r_{hi}	inner radius of hollow preform
r_{h0}	outer radius of hollow preform
r_{ti}	smaller radius of truncated conical preform
r_{t0}	larger radius of truncated conical preform
r'	radius of elemental strip on conical preform
α'	half cone angle of truncated conical preform
a, b, c, d	dimensions of irregular polygonal preform
θ_1 , θ_2 , θ_3 , θ_4	internal angles on polygonal preform
R_1 , R_2	radius of circles on polygonal preform
R_{i0}'	width of polygonal preform
L	length of polygonal preform
h	height of unfilled region
R_0	flange radius of double-hub flange
R_0'	hub radius of double-hub flange
$H_0 - H_0'$	hub height of double-hub flange
λ	constant and function of flange radius
τ_1	die–preform interfacial frictional shear stress
τ_2	container-preform frictional shear stress
ω	angular velocity of upper conical rotary die
F_{ind}	average indentation load
F_{rot}	average rotary forging load
θ	angular displacement

α	skew angle of upper conical rotary die
R_0	radius of axisymmetric preform
h_i	feed rate of upper conical rotary die
ICR	indented contact rate

Subscripts

r	radial
x	axial
θ	circumferential
y	longitudinal
z	vertical
h	hollow preform
t	truncated conical preform
i	irregular polygonal preform

CHAPTER - 1
INTRODUCTION

Outline of the Chapter: *1.1 Sinter-Forging: An Overview, 1.2 Techno-Economic Aspects, 1.3 Industrial Applications, 1.4 Plasticity Theory for Sintered Materials, 1.4.1 Die-Workpiece Interfacial Friction Conditions, 1.4.2 Densification Behaviour, 1.4.3 Yield Criterion & Compatibility Equations.*

In recent years, the world economy has undergone a process of transformation by globalization of markets, blurring of geographical boundaries, introduction of most modern information technologies, political and trade realignment etc. Innovation, development and management of technology along with factors such as design, quality, productivity, cost, speed to market etc. are some of the factors based on which game of competition is being played today. Technology development and its commercialization are the prime factors for any nation to remain competitive in this environment of global economy and are important for it's all round development. One such technology, which has reached to all general types of industries, is mechanical processing of sintered materials, *e.g.* sinter-forging, sinter-rolling, sinter-extrusion, sinter-drawing etc.

The mechanical processing technology, which has gained considerable importance in the recent past is sinter-forging, which is the subject of study under present thesis. The technique has emerged as an advanced manufacturing technology for the production of precision and high performance components economically. It uses pressed and sintered metal powder preforms as starting material having porosity in the order of 5 to 20 percent, depending upon the processing conditions. The technique is a convenient way of reducing or eliminating this porosity from the traditionally developed powder metallurgy products, which have inherent reduced mechanical and metallurgical properties [*Kuhn et al., 1970; Cull, 1970*].

The present chapter gives a brief overview of operational and techno-economical aspects of sinter-forging technology. A glimpse of its present status throughout the world is presented, which indicates that one can reap huge benefits, if the technology is properly commercialized. At last, the chapter also presents the organization of

present research work and it is expected that the present chapter will be useful in understanding the fundamentals and applications of sinter-forging technology better.

Mark et al. [1971], Fischmeister et al. [1971], Cook [1974], Im & Kobayashi [1986], Wang & Zaidi [1991a; 1991b] investigated the effect of temperature on various deformation characteristics during hot sinter-forging process. *Im & Kobayashi [1985; 1986]* and *Ranek et al. [1988]* applied finite element method technique to simulate and analyze the plastic deformation behavior and densification of metal powder preforms during sinter-forging process. In addition, a considerable amount of research work has been reported on various technological aspects of sintered preforms during sinter-rolling and sinter-extrusion processes also. *Weaver et al. [1979]* analyzed the hot rolling behavior of iron powder preforms. *Singh & Davies [1972], Tabata & Masaki [1975], Dunkley & Causton [1977], Elwakil [1979], Negm & Davies [1974] and Kumar et al. [1985]* reported investigations during cold and hot extrusion of sintered powder preforms and examined the various defects in the final sintered components.

A considerable research work including both theoretical and experimental analysis of closed-die forging of wrought materials have also been carried. *Altan & Fiorentino [1971], Akgerman & Altan [1972], Sagar & Juneja [1980], Stahlberg & Keife [1992], Fereshteh-Saniee & Jaafari [2002], Kwan [2002] and Samolyk & Pater [2004]* carried out numerical analyses of closed-die forging process using upper bound and slip-line field methods for prediction of loads and stresses. *Altan & Henning* [*1971*] and Shen *et al.* [*1989*] analyzed the flash dimension, billet size and material savings during closed-die forging process of round-shape bars. *O'Connell et al.* [*1996*], *Takemasu et al.* [*1996*], *Lee et al.* [*1997*], Akgerman *et al.* [1973] and Kim & Chitkara [*2001*] investigated the metal flow and preform optimization, *i.e.* optimal preform shape and design for improved dimensional accuracy of final forged components during flashless closed-die forging. Altan [*1971*] & Majerus *et al.* [*1992*] carried the computer simulation of precision axi-symmetric closed-die forging process to predict the load, stress and metal flow and compared the results experimentally also. Kwan [*2002*] applied concave circular parallelepiped elements to model and analyze the three-dimensional closed-die forging process and Jolgaf *et al.* [*2004*] developed a CAD / CAM system for the closed-die forging process.

Shivpuri [*1988*] reported information on past development and future trends during rotary or orbital forging processes. *Kubo et al.* [*1973, 1975, 1983], Hayama [1983] and Kobayashi [1984] and Marciniak*

[1984] carried out investigation into sinter-forging of components using rotary-forging press and reported experimental and theoretical research work on warm and cold rotary-forging of axi-symmetric and thin components. *Wang* [*2002*] applied finite element method to carry out the simulation and analysis of rotary-forging of annular ring component. *Liu et al.* [*2004*] gave the insight explanation to the mushroom effect during rotary-forging of cylindrical components.

1.1 SINTER-FORGING: AN OVERVIEW

Sinter-forging is an advanced manufacturing technology for mass production of precision, net-shape and high performance components without machining and virtually without scrap loss at competitive rates. It combines the advantages associated with two well-known techniques, *i.e.* powder metallurgy and conventional forging processes. Powder metallurgy provides sound metallurgical structure to components, as well as, avoids large number of operations, high scrap losses and high-energy consumption associated with conventional manufacturing process [*Davies & Mark, 1972; Antes, 1979*]. The subsequent, sinter-forging under hot or cold conditions provides adequate final mechanical properties like high ductility, tensile, impact and fatigue strength to traditional powder metallurgy products by reducing or eliminating porosity. The recent trend in sinter-forging procedure is to omit the sintering step, where the green preforms are heated to forging temperatures and forged immediately within the closed dies [*Nishino, 1976*]. The mechanical and metallurgical properties of these final sinter-forged products are comparable and in some cases even superior to those of cast and wrought products. Thus, it may be concluded that the present technology presents itself as an alternate route to many conventional manufacturing processes, *e.g.* casting, conventional forging, machining etc. [*Brown & Jones, 1970*].

There are two basic routes for production of sinter-forged components, namely induction heating and furnace heating routes as shown in figure 1.1. The primary difference between these routes is the method of heating green performs prior to sinter-forging operation. During induction heating route, green preforms are sintered and cooled to room temperature and then again heated and sprayed with a protective graphite coating. The coating provides protection against oxidation, as well as acts as lubricant. These coated preforms are then heated within an induction heating system under a protective atmosphere to the required forging temperatures and finally forged on a mechanical press. The toolings are also heated to in order to minimize preform distortion due to chilling. During furnace-heating route, green preforms are

sprayed with protective coating prior to sintering, which are cooled to the required forging temperatures after sintering and finally forged directly out of sintering furnace. The toolings are sprayed with water-based lubricant for cooling action and lubrication. The induction-heating route is preferred for sinter-forging of symmetrical shaped components, *e.g.* bushings and stator clutch races for automatic transmissions, because of its automatic fast-feeding ability. On the other hand, furnace-heating route is more versatile and provides better temperature control and protection of parts in a controlled atmosphere and is preferred for the production of non-symmetrical components [*Lee & Kuhn, 1979*].

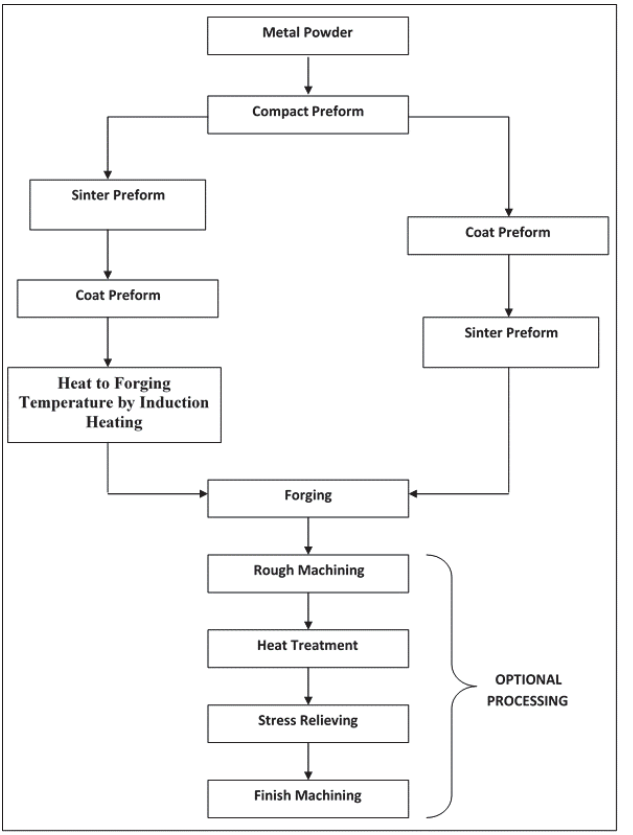

Figure 1.1: Flow diagram of sinter-forging process.

1.2 TECHNO-ECONOMIC ASPECTS

Sinter-forging is a modern technology, which is capable of producing near-net-shape components with very close tolerances having high load bearing capacity. It also ensures the weight control of final sinter-forged components within less than 0.5 percent of the total component's weight. This prevents the damage of forging dies by over-loading and ensures high dimensional accuracy of the final sinter-forged components [*Downey & Kuhn, 1979*].

The ductility, impact and fatigue strength of conventional-forged materials are inferior in the transverse direction, whereas sinter-forged components exhibit uniform properties in all the directions and behave isotropic with reference to the mechanical properties. This is advantageous, because in most applications, the components are subjected under complex multi-axial stress systems [*Pietrocini, 1974*].

Figure 1.2 shows the metal powder, preform and sinter-forged spur gear, whose directional properties are absent. It demonstrates that initially the metal powder is taken loose and then compacted in closed dies to form metal preforms. Finally, these preforms are forged to the required shape and size, either at room or elevated temperature [*Allen et al., 1979*]. The gears made by machining from conventional forged blank leaves transverse grain lines exposed to critical stress directions as shown in figure 1.3. Thus, in general, the properties of sinter-forged components are in mid-way between the anisotropic extremes of the conventionally forged products, which can be further improved by the use of pre-alloyed metal powders and extended sintering cycles within protective or controlled atmosphere [*Morimoto et al., 1974*].

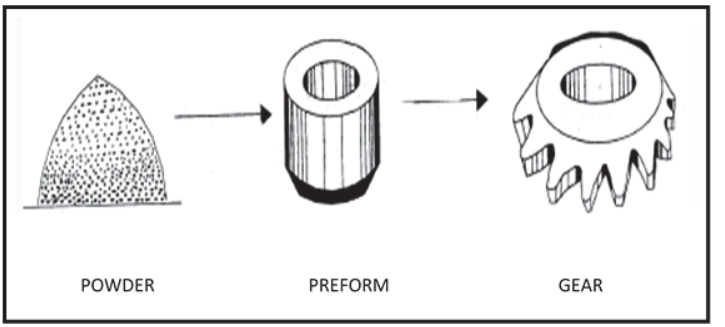

Figure 1.2: Sinter-forging of a gear.

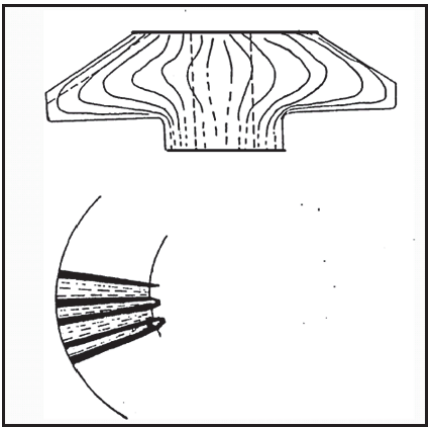

Figure 1.3: Gear made by machining from conventionally forged blank.

In addition to distinct technical advantages, the sinter-forging technology also offers cost advantages over conventional-forged and cast components. The process flow chart for sinter-forging and conventional wrought-forging is illustrated in figure 1.4. The number of operational steps involved in sinter-forging process is considerably less than that of conventional-forging technique. Further, conventional-forged components require large machining at the end and hence, there is a considerable loss of material in the form of scrap, as compared to sinter-forged components [*Antes, 1979*].

The important reasons for cost reduction during sinter-forging process, as compared to conventional-forging technique may be summarized as follows [*Jones, 1970; Wisker & Johns, 1974; Jha A.K. et al., 1994*]:

- Reduction in the number of forging steps.
- Reduction in the forging pressure, allows the use of smaller tools and equipments.
- Reduction in the forging temperatures makes the pre-heating less costly.
- Reduction in the die manufacturing and operational cost.
- Reduction of the scrap due to elimination of flash and secondary machining operations because of improved dimensional control and surface finish.
- Mass production of typical parts at a rate of several hundreds to many thousands per hour.

The simplicity in process and inherent techno-economic advantages has led to better and rapid realization of sinter-forging technology by most of the industries engaged in the mechanical processing of materials.

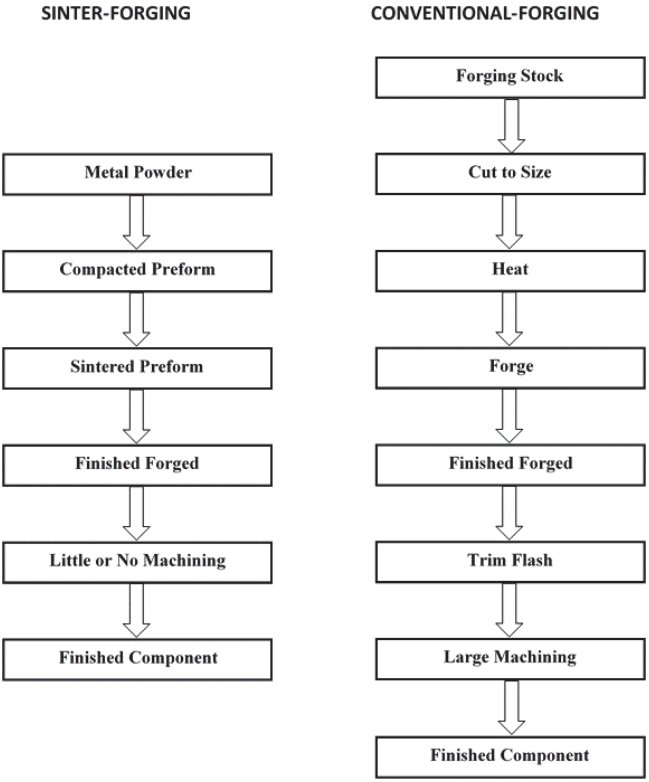

Figure 1.4: Process flow chart for sinter & conventional-forging.

1.3. INDUSTRIAL APPLICATIONS

The interest in powder metallurgy forming has attracted the attention of a large number of research workers, both in the field of powder metallurgy and sinter-forming. Literature survey has indicated that a lot of work has been reported on the production of powder components, which include processes like powder compaction, densification and sintering. *Morgan et al. [1969], Alexander et al. [1971], Shima et al. [1972], Fischmeister [1982], Stein et al. [1964], Wang & Davies [1968], Elwakil & Davies [1972], Vitvaz & Roman [1972] and Kumar et al. [1982]* have studied the isostatic metal powder compaction process and investigated the effect of die speed on compacting pressure, green density, green strength and hardness of metal powder compacts. *Wang et al.* [*1981*], *Biner & Spitzig* [*1990*] and *Kim* [*2002*] have examined the densification mechanism and density distribution

during powder compaction process under different hydrostatic pressures.

Kiyota et al. [1984] and Galanty et al. [2002] studied the compaction and densification behavior of metal powders during rotary-forging and extrusion process respectively. *Hwang & Kobayashi* [*1991*] applied finite element method to analyze the compaction pressures involved during powder metal compaction process. *Zape [1970], Ward & Biullington [1979], Lindskog [1979], Kao & Koczak [1980], Hwang & Kobayashi [1990] and Brakpool [1992]* have studied critically the deformation characterization of metal powders and effect of addition of various additives like lubricants and other alloying metals during powder metal compaction process. *Hamiuddin & Upadhyaya [1980a, 1980b], Borland et al. [1980] and Tengzelius & Blande [1982]* have studied the sintering procedures and effect of temperature and alloying metals on final density, strength and hardness of the metal powder compacts.

Industrial interest in the mechanical processing of sintered materials, especially sinter-forging, sinter-rolling and sinter-extrusion initiated in mid-sixties, when General Motors in America successfully tested connecting rods made out of iron powder. By seventies, several countries like USA, UK, Germany and Japan started developing several machine parts by sinter-forging technology. This interest was gradually extended to variety of steels, ferrous and non-ferrous metals and their alloy powders like brass, aluminum, bronze, super alloys etc. [*Miska, 1979; Brown, 1979*].

The technology of sinter-forming has already reached successfully to many high production sophisticated industries, such as automobile, aerospace, defense, machine tools, electrical, industrial hand tools, atomic energy and other general purpose industries engaged in the production of bicycles, farm equipments, hydraulic pumps, watches, sewing machines, mobile phones, business machines, computers, gadgets etc [*Antes, 1977*].

Materials in the form of sintered preforms not only delivered better physical, chemical and thermal properties, but also made new applications possible. One such pioneering application of sintered material is production of cemented carbide tools, which has revolutionized the machining industry. A large number of components with simple and complex generic shapes are produced on a wide scale by this technology for various applications in automobiles *e.g.* intricate components of engine, transmission, steering, braking and exhaust systems like cam, cam-stator, filter, by-pass system, bi-metal contact, connecting rod, simple gear, balancer gear, ring gear, crankshaft, toothed pulley, valve, valve train components, seat insert, guide, bronze bearing, bearing cap, clutch plate, clutch hub, clutch pressure-plate etc [*Elrich & Neubert, 1992*].

The sinter-forging route offers considerable cost savings and improved performance like large stiffness-to-weight ratio and high durability over conventional-forging process and continues to add value to car and light truck manufacturing units, which are facing enormous cost-reduction pressures. The three big vehicle manufacturers in America, namely General Motors, Ford and Daimler Chrysler on an average consumed 10 kg of powder metallurgy components during early nineties, which have expected to reach about 25 kg recently. Presently, America is engaged in the production of about 4,50,000 tons of powder metallurgy components per year [*Matsumoto, 1978*].

The development in Asia-Oceania region is also not far away. Figure 1.5 shows the industry-wise split-up in India, which shows that automotive industry consumes about 74 percent of Indian industry [*Subarao et al., 1998*]. The automobile industry accounts for about 80 percent of sinter-forged components and has been a fruitful source of application. Thus, evaluating sinter-forging from this perspective is also essential. The maturation of automotive market in India due to advent of number of world-class automobile manufacturers in last decade has led to strong growth of powder metallurgy industry, though foundation for its sustained growth was laid by Mahindra Sintered Products, Siemetals Company, Sundaram Fasteners and Brico Goetz in seventies only. India stands fourth behind China, Korea and Taiwan in powder metallurgy component production in Asia-Oceania region and is presently producing roughly 8000 tons of powder metallurgy parts per year. Table 1.1 also shows that it stands fourth behind China, Korea and Taiwan, as far as the overall infrastructure facilities in terms of powder metallurgy part producers, powder producers, powder

metallurgy tool and equipment manufacturers are concerned [*Singh et al., 2001*].

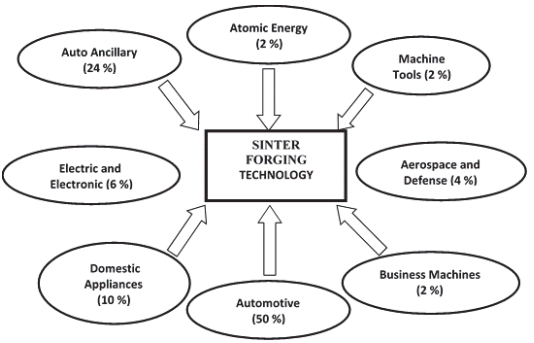

Figure 1.5: Industry-wise sinter-forging application in India.

Table 1.1: Status of powder metallurgy industry in Asia-Oceania region.

Country	Powder Metallurgy Parts Manufacturers	Powder Manufacturers	Tools and Equipment Manufacturers
China	166	38	20
Korea	18	03	08
Taiwan	45	02	10
India	15	10	15

1.4 PLASTICITY THEORY FOR SINTERED MATERIALS

The deformation behavior of sintered materials during mechanical processing is entirely different from that of wrought metals. The present chapter presents important characteristics during plastic deformation of sintered materials, *e.g.* die-workpiece interfacial friction conditions, densification behavior, yield criterion and associated compatibility conditions.

The deformation behavior during metal powders compression is entirely different from the compression of wrought metals, as it is characterized by change in volume due to change in porosity of the compact. A sintered preform with high relative density (pores of small size and number) yields at relatively high stress, whereas a low relative density preform (pores of large size and number) yields at relatively low stress. A lot of researchers have developed plasticity theory and yield criterion for porous solids and reported their investigations about the governing compatibility conditions during metal powder compression process.

Green [1971], Downey & Kuhn [1971], Elwakil [1974], Shima & Oyane [1976] and Lewis & Khoei [2001] have carried extensive investigations during compression of metal powders and established the plasticity upper-bound and slip-line field theories for sintered powder materials. It was found that yielding of sintered materials is sensitive to hydrostatic stresses component imposed, as yield surface closes on the hydrostatic stress axis. *Tabata & Masaki [1978], Thomas [1984], Kim et al. [1990], Lee & Kim [1992], Akisanya et al. [1997], Griffiths et al. [1976] and Justino et al. [2004]* studied the plastic yield behavior of porous metals and proposed the principal strain increments, volumetric strain increments and corresponding yield criterion for powder metallurgy materials. The compatibility conditions were studied critically and various constitutive models for plastic analysis of porous sintered materials were established.

A lot of investigators utilized these plasticity theories, yield criterions and compatibility conditions to theoretically analyze and predict the pressure distribution, deformation load, strain rates, bulged profiles, final density and energy dissipations during problems related to mechanical processing of sintered materials. *Squire [1947], Nakagawa et al. [1971, 1972], Huppmann [1977] and Standring et al. [1980]* studied the deformation characteristics *e.g.* forging load, metal flow and magnitude of strains involved during cold sinter-forging of sintered metal powder preforms with different generic shapes both theoretically and experimentally. *Tabata & Masaki* [*1978, 1980, 1990*] estimated experimentally the measure of coefficient of interfacial friction during sinter-forging and flow stress of porous sintered preforms. *Kim et al. [1988, 1989, 1992] and DeSilva & Ramesh [1997]* carried out the investigations into rate-dependent deformation behavior and strain hardening responses of sintered porous materials under various stress conditions. *Difai [1974], Forguson et al. [1977], Suh & Kuhn [1977], Tiwari et al. [1982], Chitkara & Liaghat [2001]* studied the forgeability, fatigue, fracture and deformation modes of metal powder preform during sinter-forging process and suggested possible preventive criterion.

1.4.1 Die-Workpiece Interfacial Friction Conditions

The interfacial friction conditions during mechanical processing of sintered materials are entirely different from that of machine parts. During sinter-forging processes, the workpiece surface distorts and takes the impression of die surface and the high interfacial pressure and relative velocity between sliding surfaces in combination with complex deformation modes and impact inertia not only increase the preform

relative density, but also creates condition essential for adhesion interfacial friction, in addition to the sliding friction. The magnitude of interfacial sticking friction depends upon the specific cohesion factor and preform relative density. Thus, the interfacial friction between die and workpiece surfaces in contact during sinter-forging process is composite in nature and includes both sliding and sticking frictions.

The metal flow pattern during sinter-forging suggests that two interfacial friction zones exists, *i.e.* an inner zone with no relative movement between die and workpiece surface (sticking friction zone) and an outer zone with sliding of surfaces (sliding friction zone). The frictional shear equation for such composite interfacial frictional conditions during axi-symmetric and plane-strain deformation conditions respectively may be expressed as follows [*Kumar, 1999*]:

$$\tau = \mu\left\{p + \rho_0\varphi_0\left[1-\left(\frac{r_m - r}{nr_0}\right)\right]\right\} \tag{1.1}$$

$$\tau = \mu\left\{p + \rho_0\varphi_0\left[1-\left(\frac{x_m - x}{nl}\right)\right]\right\} \tag{1.2}$$

The first and second terms of above equations denotes the sliding and sticking frictions respectively. It is clearly evident that sticking friction is a function of preform relative density and specific cohesion factor. The sticking zone distances *'r_m'* and *'x_m'* respectively may be approximated by Rook's equation is given as below [*Biswas & Rooks, 1971*]:

$$r_m = r_o - \frac{H_0}{2\mu}\ln\left(\frac{1}{\mu\sqrt{3}}\right) \tag{1.3}$$

$$x_m = l - \frac{H_0}{2\mu}\ln\left(\frac{1}{\mu\sqrt{3}}\right) \tag{1.4}$$

The above equations may be suitably formulated for various sinter-forging processes considered during present thesis as follows:

$$\tau_{hollow} = \mu\left\{p + \rho_0\varphi_0\left[1-\left(\frac{r_{hm} \pm (r_{hn} - r)}{nr_{h0}}\right)\right]\right\} \tag{1.5}$$

$$\tau_{truncated} = \mu\left\{p + \rho_0\varphi_0\left[1-\left(\frac{r_{tm} - r}{nr_{tj}}\right)\right]\right\} \tag{1.6}$$

(j = i and 0 for smaller and bigger ends)

$$\tau_{irregular} = \mu\left\{p + \rho_0\varphi_0\left[1-\left(\frac{r_{im}-r}{nR_j\sec\theta}\right)\right]\right\} \quad (1.7)$$

(j = 1 for zone I and j = 2 for zone III)

$$\tau_{irregular} = \mu\left\{p + \rho_0\varphi_0\left[1-\left(\frac{x_{im}-x}{nL}\right)\right]\right\} \text{ (zone II)} \quad (1.8)$$

$$\tau_{closed-die-preform} = \mu\left\{p + \rho_0\varphi_0\left[1-\left(\frac{r_{cm}-r}{nS}\right)\right]\right\} \quad (1.9)$$

$$\tau_{closed-container-preform} = \mu\left\{p + \rho_0\varphi_0\left[1-\left(\frac{z_{cm}-z}{nH_0'}\right)\right]\right\} \quad (1.10)$$

$$\tau_{rotary} = \mu\left\{p + \rho_0\varphi_0\left[1-\left(\frac{r_{rm}-r}{nR_0}\right)\right]\right\} \quad (1.11)$$

where,

$$r_{hm} = r_{ho} - \frac{H_0}{2\mu}\ln\left(\frac{1}{\mu\sqrt{3}}\right) \quad (1.12)$$

$$r_{im} = R_j\sec\theta - \frac{H_0}{2\mu}\ln\left(\frac{1}{\mu\sqrt{3}}\right) \quad (1.13)$$

$$r_{cm} = S - \frac{H_0'}{2\mu}\ln\left(\frac{1}{\mu\sqrt{3}}\right) \quad (1.14)$$

$$z_{cm} = H_0' - \frac{R_0}{2\mu}\ln\left(\frac{1}{\mu\sqrt{3}}\right) \quad (1.15)$$

$$r_{rm} = R_0 - \frac{h_i}{2\mu}\ln\left(\frac{1}{\mu\sqrt{3}}\right) \quad (1.16)$$

1.4.2 Densification Behaviour

The investigation during mechanical processing of sintered materials revealed that compressive forces gradually close down the inter-particle pores within the preforms leading to decrease in volume and subsequent increase in its relative density. The increase in preform relative density depends upon the processing conditions such as die-speed and interface surface conditions, where the real area of contact grows and approaches to apparent one, as shown in figure 1.6. This approach may probably be an asymptotic one [*Kumar, 1976*]. It is also observed that preforms with high relative density, *i.e.* smaller pores

yields at relatively higher stress, as compared to preform with low relative density, *i.e.* larger pores. The density distribution is also not uniform throughout the preform. It is high at central region and low at the edges of preform surface. It is more uniform for smaller coefficient of interfacial friction and higher initial relative density of sintered preforms. The empherical relationship between external die pressure and preform relative density during sinter-forging process may be given as [*Sutradhar et al., 1995*]:

$$\left(\frac{p}{\sigma_0}\right) = -\left[\left(\frac{2}{3}\right)\ln(1-\rho_0)\right] \tag{1.17}$$

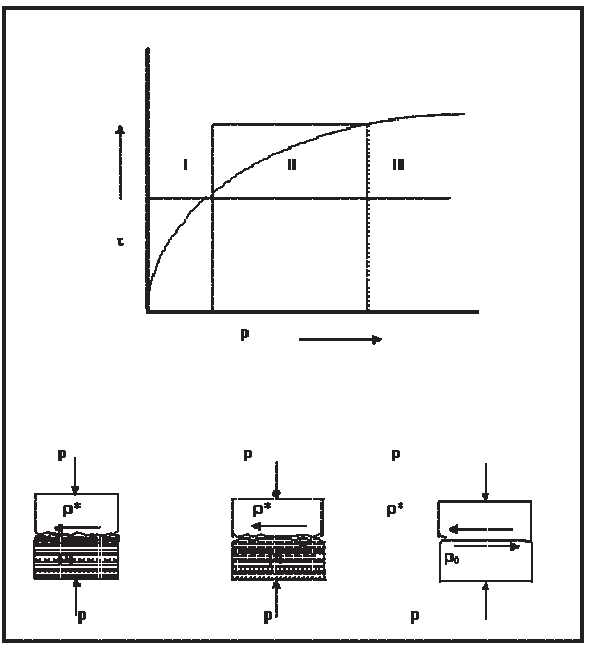

Figure 1.6: Regimes of preform density variation during sinter forging process.

1.4.3 Yield Criterion & Compatibility Equations

The analysis during conventional-forging of wrought metal assumes volumetric constancy, which cannot be made during mechanical processing of sintered materials, where density does not remain constant due to the imposed hydrostatic stress component. Tabata & Masaki suitably formulated and proposed a yield criterion and an expression for principal strain increments during mechanical processing of sintered porous materials, which are given as follows respectively [*Tabata & Masaki, 1978*]:

$$\rho_0^k \sigma_o = \left[\sqrt{3J_2'} \mp (3\eta\sigma_m) \right] \tag{1.18}$$

$$d\varepsilon_{ii} = \left\{ d\lambda \left[\frac{3(\sigma_{ii} - \sigma_m)}{2\sqrt{3}J_2'} \pm \eta \right] \right\} (i = 1,2,3) \tag{1.19}$$

The upper negative sign is assumed for compressive nature of hydrostatic stress ($\sigma_m \le 0$), whereas the lower positive sign is for tensile nature of hydrostatic stress ($\sigma_m > 0$). Figure 1.7 shows the Tabata & Masaki yield surface for sintered porous materials given by the equation (1.13), which consists of two cones, whose height increases with increase in the relative density of preform [*Tabata & Masaki, 1978*]. When $\rho_0 \cong 1$, *i.e.* a pore-free metal, the cone becomes a cylinder and equation (1.13) reduces to Von-Mises yield criterion. The values of *'η'* and *'k'* are experimentally determined from the simple compression and tension tests conducted on sintered metal powder preforms. The values of *'η'* and *'k'* for Aluminium metal powder preforms are given as follows [142]:

$$\eta = \left[0.54(1-\rho)^{1.2} \right] \quad \text{for} \quad \sigma_m \le 0 \quad \text{and} \quad k = 2 \tag{1.20}$$

$$\eta = \left[0.54(1-\rho)^{0.83} \right] \quad \text{for} \quad \sigma_m > 0 \quad \text{and} \quad k = 2 \tag{1.21}$$

These values may also be used for other porous metal powder preforms, provided such preforms exhibit similar plastic deformation behavior. The basic compatibility equations during axi-symmetric and plane-strain conditions of sinter-forging as derived from the equations (1.15) and (1.16) respectively are given as follows (Refer Appendix A):

$$\dot{\varepsilon}_{rr} + \dot{\varepsilon}_{\theta\theta} + \left(\frac{1-2\eta}{1+\eta} \right) \dot{\varepsilon}_{zz} = 0 \tag{1.22}$$

$$\dot{\varepsilon}_{xx} + \left[\frac{(1+2\eta^2) - 2\eta\sqrt{3(1-\eta^2)}}{(1-4\eta^2)} \right] \dot{\varepsilon}_{zz} = 0 \tag{1.23}$$

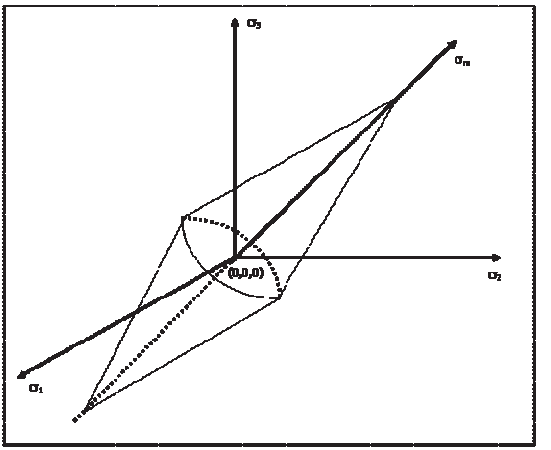

Figure 1.7: Tabata and Masaki yield surface for porous metal powder preforms.

CHAPTER - 2
BASIC EXPERIMENTAL ANALYSIS DURING SINTER-FORGING

Outline of the Chapter: *2.1 Fabrication of Powder Compaction & Forging Dies; 2.2 Fabrication of Powder Preforms; 2.3 Measures of Sinter-Forging Characteristics*

Dean et al. [1971] & Jones et al. [1971] carried out both theoretical and experimental investigations of dynamic effects in high-velocity compression of electrolytically pure copper specimens under plane strain and axi-symmetric conditions. The experiments were carried on an explosively driven compression-testing machine up to strain rates as high as 4000/s with an objective to study dynamic aspects *e.g.* strain rates and inertia effects. The analysis assumed free-flight of moving press platen prior to impact. The plastic wave propagation effects were neglected. The investigations concluded that experimental strain rate variations were in reasonable agreement with the theory. The material work hardens during deformation at ambient temperature and thus, produces higher strain rates than a perfectly plastic material. The stress-strain curves obtained during high-velocity plane strain and axi-symmetric compression, although similar in level, were markedly different in shape. The high-speed plane strain compression compared with upsetting operation produces increased stresses at low strains and lower stresses at intermediate strains, which tend to increase with increase in billet size. It was demonstrated that the effects of billet inertia on flow stress are considerably more pronounced in plane strain than in axi-symmetric compression. Finally. It was concluded that experimental strain rate variations are in reasonable accord with the analysis, however, inertial theory was in qualitative agreement with results of high-velocity plane strain and axi-symmetric compression tests.

In order to investigate the dynamic effects during mechanical processing of sintered materials and to establish the plasticity theory for sintered materials, experiments have been conducted on sintered metal powder preforms under cold conditions. The preforms have been fabricated by compacting metal powders in closed cavity powder compaction dies and subsequently sintering in a muffle-type furnace.

These preforms were later forged in a mechatronic press. The basic experimental work consists of preparation of powder compaction and forging dies, powder preforms and measurements of deformation characteristics during various sinter-forging processes under consideration.

2.1 FABRICATION OF POWDER COMPACTION & FORGING DIES

Different closed-cavity powder compaction die sets of alloy steel with good surface finish have been fabricated, according to different shapes of preforms to be produced. Figure 2.1 shows the

For production of cylindrical, truncated conical and hollow disc metal powder preforms, a closed circular-cavity powder compaction die set with bore diameter equal to 30 mm has been fabricated as shown in figure 2.1 (a). A closed square-cavity powder compaction die with cavity side length equal to 35 mm has been fabricated for production of irregular polygonal preforms as shown in figure 2.1 (b). Both the die sets were fabricated in three separate parts, namely, flat upper punch, lower counter punch with obtrude recess and a central container to house punch and counter-punch. Various die-sets having different diameters are shown in figure 2.1 (c).

Die set of alloy steel with good surface finish has been fabricated for performing experimentation associated with closed-die sinter-forging and rotary sinter-forging processes. The closed-die set comprising of moving upper and stationary lower counter punches housed in a container has been used to conduct experiments during flashless closed-die sinter-forging of cylindrical preform into double-hub flange component as shown in figure 2.2. Both the punches have cylindrical recess-cavities, with depth and diameter respectively equal to length (5.0 mm) and diameter (20.0 mm) of hubs of the required double-hub flange component. These cavities also minimize the variability and difficulty in preform location within the closed-die set. An upper conical die has also been fabricated to conduct experiments during rotary sinter-forging with cone axis inclined at an angle of 10^0 with vertical axis, *i.e.* cone apex angle equal to 160^0. Figures 2.3 (a) & (b) show schematic line drawing and illustration of upper conical die set. The inner walls of all the die sets has been finished to good surface finish with polishing paste.

Figure 2.1 (a): Closed circular-cavity powder compaction die set.

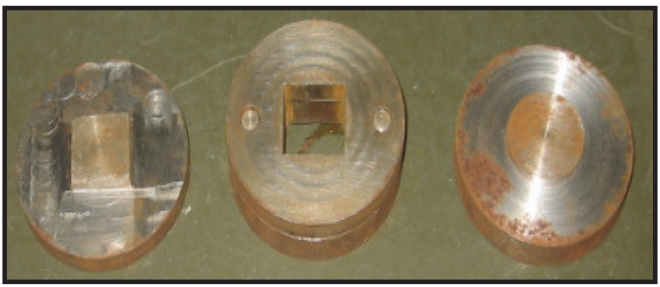

Figure 2.1 (b): Closed square-cavity powder compaction die set.

Figure 2.1 (c): Powder compaction die sets with varying diameters.

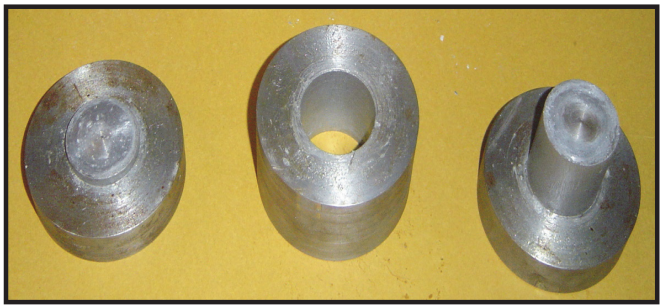

Figure 2.2: Die set for closed-die sinter-forging.

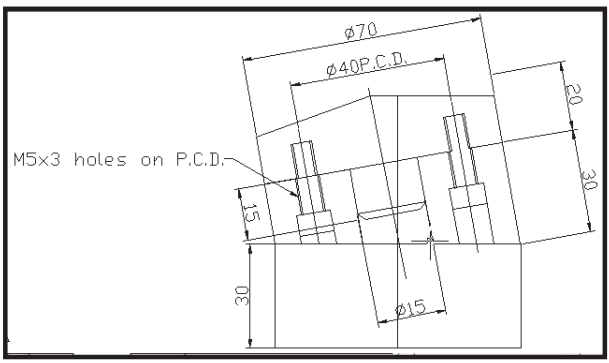

Note: All dimensions are in mm.

Figure 2.3 (a): Line diagram of upper conical rotary die.

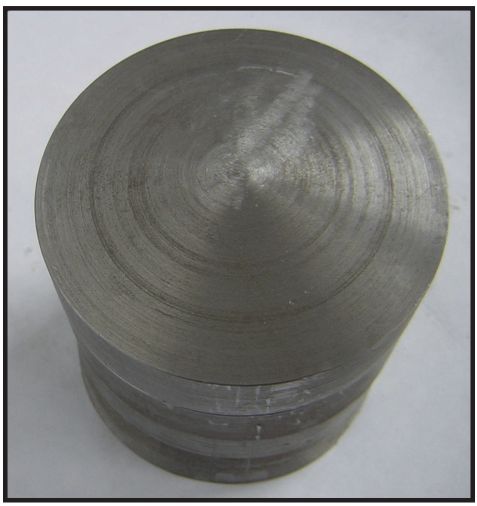

Figure 2.3 (b): Upper conical die for rotary sinter-forging of powder preforms.

2.2 FABRICATION OF POWDER PREFORMS

Two different metal powders has been used to fabricate powder preforms with required shapes. Electrolytic copper metal powder having purity more than 99% and particle size less than 350 mesh size has been used to fabricate hollow disc preforms. Atomized Aluminium metal powder having purity and particle size more than 99% and 13.0 microns respectively has been used to fabricate cylindrical, truncated conical and irregular polygonal preforms. The physical characteristics, such as particle sizes, apparent and tap densities along with the chemical characteristics for Copper and Aluminium metal powders are shown in tables 2.1 and 2.2 respectively [*Jha et al., 1983*].

Table 2.1: Physical and chemical characteristics of electrolytic Copper metal powder.

Sieve Analysis (BS Sieves)	Wt. Retained (%)	Chemical Analysis	Wt. (%)
+ 100 mesh	0	Copper	99.80
- 100 + 150 mesh	35.00	Phosphorus	< 0.001
- 150 + 200 mesh	15.00	Iron	< 0.006
- 200 + 240 mesh	14.50	Silicon	< 0.002
- 240 + 350 mesh	20.00	Apparent density	2.5 gm / c.c.
- 350 mesh	14.50	Tap density	4.0 gm / c.c.

Table 2.2: Physical and chemical characteristics of atomized Aluminium metal powder.

Particle size (microns)	Weight Under (%)	*Chemical Analysis*	Weight (%)
118.0	100.0	Aluminium	99.500
88.1	98.9	Iron	< 0.1700
65.6	95.5	Silicon	< 0.1313
48.8	88.8	Zinc	< 0.0053
36.3	79.0	Manganese	< 0.0023
27.0	65.8	Magnesium	< 0.0016
17.4	40.1	Apparent density	1.25 gm / c.c.
13.0	25.5	Tap density	1.50 gm / c.c.

Figure 2.4 shows the schematic representation of the compaction of the metal powder within the compaction die sets as fabricated above. The metal powders were compacted in respective closed circular and square-cavity compaction dies using a 150-ton hydraulic compaction press as shown in figure 2.5. The compaction of copper and Aluminium metal powders has been performed at pressures of 25-30 tonf and 15-20 tonf respectively. In both the cases, the die walls have been lubricated with graphite paste prepared by mixing fine graphite powder and

mineral oil. The copper powder green compacts were sintered at about 600^0 C temperature for three hours, whereas Aluminium metal green compacts were sintered at 400^0 C temperature for four hours in an endothermic sand atmosphere. The sintering operations were carried in order to develop mechanical strength in the metal powder compacts. Subsequently, these compacts were wrapped in a *'Teflon'* sheet and repressed at the same compaction pressure in the same die and again re-sintered at the same temperature for same duration of time, to obtain uniform density distribution. All the sintering operations has been carried in a P.I.D. controlled muffle-type silicon carbide furnace, which is capable of providing temperatures up to 1500^0 C accurately in various segments as shown in figure 2.6.

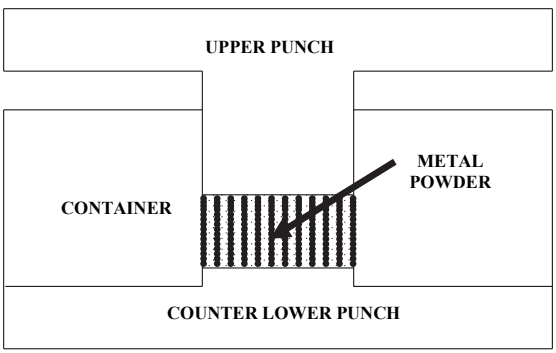

Figure 2.4: Schematic diagram of compaction of metal powder within compaction die set.

Figure 2.5: Powder compaction press.

Figure 2.6: PID controlled furnace.

The sintered compacts were finally machined to the required dimensions and polished with coarse and fine emery papers. The preform actual density has been calculated simply by measuring its dimensions and weight. The relative density has been obtained as the ratio of actual density of preform to the density of corresponding solid metal. The copper metal powder compacts (30.0 mm initial diameter) has been machined to obtain hollow disc preforms with 12.0 mm outer radius, 10.0 mm height and different inner radius, *e.g.* 6.0, 7.5, 8.0 and 10.0 mm. The truncated conical preforms has been obtained by machining Aluminium metal powder cylindrical compacts with 30.0 mm initial diameter and 12.0 mm large radius and 17.0 mm height. Three different smaller radii of truncated conical preform, *i.e.* 7.5 mm, 9.0 mm and 11.0 mm corresponding to half cone angles 15^0, 10^0 and 5^0 respectively has been obtained by machining as shown in figure 2.7. The irregular polygonal preform has been obtained by machining Aluminium metal powder square compacts (35.0 mm initial side-length) to the required dimensions depending upon the shape-complexity factors considered under present study.

The Aluminium metal powder cylindrical preforms have been machined to the required dimensions of 15.0 mm radius with heights equal to 30 mm, 22.5 mm, 15 mm and 6.0 mm corresponding to the preform aspect ratio of 1.0, 0.75, 0.50 and 0.20 respectively for flashless closed-die sinter-forging operation. The Aluminium metal powder axi-symmetric disc preforms required for rotary sinter-forging has been obtained by machining cylindrical compacts to 15 mm diameter and 10 mm height. The dimensions of all metal powder preforms used for experimental investigation of dynamic effects during mechanical processing of sintered materials is summarized in table 2.3.

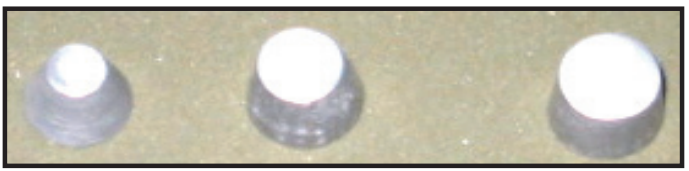

Figure 2.7: Truncated conical Aluminium metal powder preforms.

Table 2.3: Initial Relative Density (approx.) & Dimensions (mm) of Sintered Preforms

1). Open-Die Sinter-Forging							
Hollow Preform: $\rho_0 = 0.80$; $r_{h0} = 12.0$; $H_0 = 10.0$							
$C_p = \frac{r_{h0}}{r_{hi}}$	r_{hi}						
2.0	6.0						
1.6	7.5						
1.5	8.0						
1.2	10.0						
Truncated Conical Preform: $\rho_0 = 0.80$; $r_{t0} = 12.0$; $H_0 = 17.0$							
$C_p = \frac{r_{t0}}{r_{ti}}$	α	r_{ti}					
1.1	5^0	11.0					
1.3	10^0	9.0					
1.6	15^0	7.5					
Irregular Polygonal Preform: $\rho_0 = 0.75$; $H_0 = 10.0$							
$C_q = \frac{R_1}{R_2}$	a	b	c	d	L	R_1	R_2
0.85	6.5	5.5	16.0	14.0	0.8	9.2	10.8
0.60	4.6	4.4	15.6	14.4	3.6	7.5	12.5
0.30	2.6	2.4	15.4	14.6	6.0	4.5	15.5
2). Closed-Die Sinter-Forging							
Cylindrical Preform: $\rho_0 = 0.75$; $R_0 = 15.0$; $R'_0 = 10.0$; $H_0 = 20.0$; $(H'_0 / R_0) = 0.25$, 0.50, 0.75 and 1.0							
3). Rotary Die Sinter-Forging							
Axi-Symmetric Disc Preform: $\rho_0 = 0.70$; $R_0 = 15.0$; $H_0 = 10.0$							

2.3 MEASURES OF SINTER-FORGING CHARACTERISTICS

The experiments and measurement of deformation characteristics to analyze dynamic effects during mechanical processing of sintered materials have been conducted using appropriate dies on 150-ton computer controlled hydraulic press as shown in figure 2.8. The press has stationary upper die platen, whereas lower die platen moves upward with metal powder preforms of known dimensions and relative density kept on it. The computer control of press enables precise control and record of various deformation characteristics during mechanical processing of sintered materials.

The forgeability of copper and Aluminium metal powder preforms has been evaluated by applying known compressive loads and observing the occurrence of external cracks. The preforms with different initial relative densities and shape-complexity factors were forged on the mechatronic press under varying die speed and interfacial friction condition at room temperature and the respective dimensional changes were recorded. The maximum height reduction without the occurrence of external cracks has been observed to be about 42% under lubricated (vaseline) conditions at die speed of 0.25 m/s (highest speed available on the mechatronic press). For lower die speeds and high interfacial friction conditions, the formability has been observed to be low, *i.e.* 30 to 35% of preform height reduction. Figures 2.9 (a) (b) shows various preforms after sinter-forging operations.

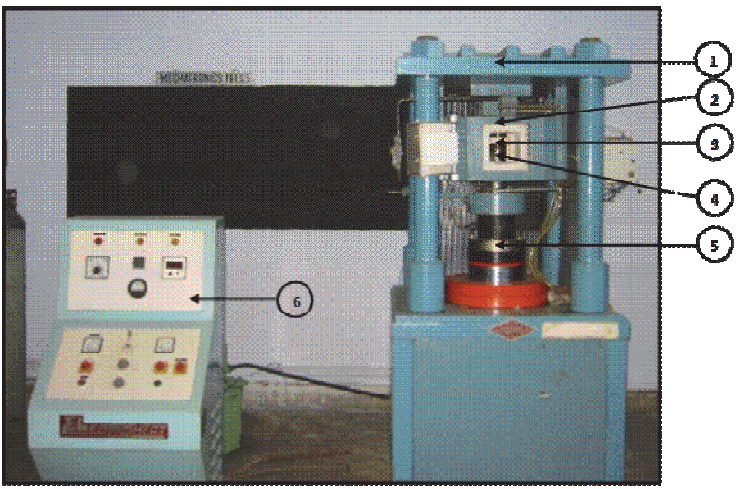

Figure 2.8: Computer controlled mechatronic hydraulic press.
1. Press Frame; 2. Heating Chamber; 3. Preform; 4. Die platen; 5. Load Cell; 6. Control Panel

Figure 2.9 (a): Aluminium metal powder compacts with varying l /d ratio.

Figure 2.9b: Copper metal powder preforms after forging under (i) lubricated conditions; (ii). dry conditions

Figure 2.10 shows the variation of perform relative density with powder particle size. It is evident from the figure that preform relative density increases with decrease in powder particle size. This due to better consolidation of powder particles, when they are in small size, in the order of 40 microns or less, which is also confirmed by *Borland [1980]* in his studies on the compaction behavior of powder performs with respect to different particle size and shape. Figure 2.11 shows the variation of perform relative density with respect to the compaction pressure during preparation of the metal powder preforms. It was found that relative density of the perform increases with increase in compaction pressure. This is because high compaction pressure leads to better consolidation of the powder particles and decreases the inter particles pores within the preforms, which is confirmed with the research works of *Kao & Koczak [1980]*, who carried out extensive investigation to the compacting behavior of ferrous powders.

Figure 2.12 shows the variation between preform relative density with sintering temperature for different compaction pressures. It is evident from the figure that relative density increases with increase in sintering temperature and the corresponding values of relative density is higher for higher compaction pressure. The result is completely agrees with the work of *Standring et al. [1980]*. The increase in relative density is attributed due to some kind of diffusion process happening within the performs during sintering, which leads to better bonding between the powder particles, as well as, decreases the inter particle pores size. This is also confirmed by work carried out by *Difai [1974]*.

Figure 2.13 shows the variation of relative density of perform with height reduction of the specimen during forging. It is evident that relative density increases with increase in height reduction and becomes comparable to that of wrought materials at the end operation. The lubricated performs exhibit better densification than the unlubricated ones (dry conditions). Also the preforms with higher l/d ratio become more densified as compared to the ones having smaller l/d ratio. This is so because of flow of preform material is better in case of

slender performs and at lubricated conditions. This completely agrees with the work of *Fischmeister et al. [1971]*.

Figure 2.14 shows the variation of radial & axial strains with preform height reduction under lubricated and dry frictional conditions. As it is evident from the figure the radial & axial strain increases with the preform height reduction, more or less exponetionally, which also detected by work of *Kuhn et al. [1970]*. It can also be seen that the strains during lubrication friction condition is higher as compared to the dry condition due to better flow of the material. Figure 2.15 shows the variation of Poisson's ratio with preform height reduction. The theoretical curve for Poisson's ratio represents the relation between radial and vertical strains for a fully dense material (slope of one half, *i.e.* $\nu = 0.5$) or wrought materials. The curves for porous materials are below the theoretical curve (slope less than 0.5) but gradually become parallel to it, as full density is approached. The variation of Poisson's ratio for sintered materials may be plotted from this curve. The theoretical variation of Poisson's ratio may also be plotted by empherical equation, $\nu = 0.5\ \rho_0^2$ given by *Elwakil & Davies [1972]*. It can be seen that the Poisson's ratio is higher for the lubricated conditions due to the better flow of material.

Figure 2.16 it shows relationship between Poisson's ratio with Preform Relative Density under lubrication condition. It is evident that as deformation proceeds, the compaction of the preform takes place simultaneously with the deformation. Therefore, the relative density of preform increases, as well as, the Poisson's ratio also increases approaches the theoretical value, *i.e.* $\nu = 0.5$, as shown by the extrapolated line on the graph. Figure 2.17 shows the forgeability evaluation on the sintered performs. It is evident from the figure that forgeability is better in lubricated conditions and higher for performs with higher l/d ratio. The forgeability is measured by the maximum possible height reduction of the preform just before start of the cracks on the equatorial regions. This is also confirmed by the work of *Tiwari et al. [1982]* and results completely agree with it.

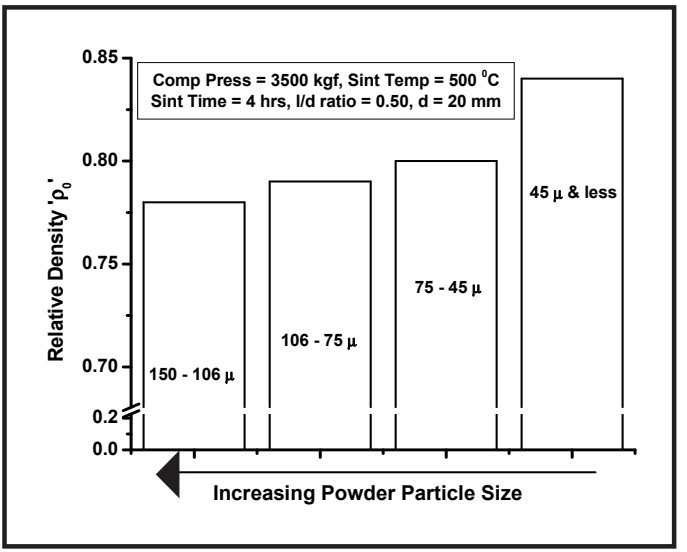

Figure 2.10: Variation of relative density of preform with particle size.

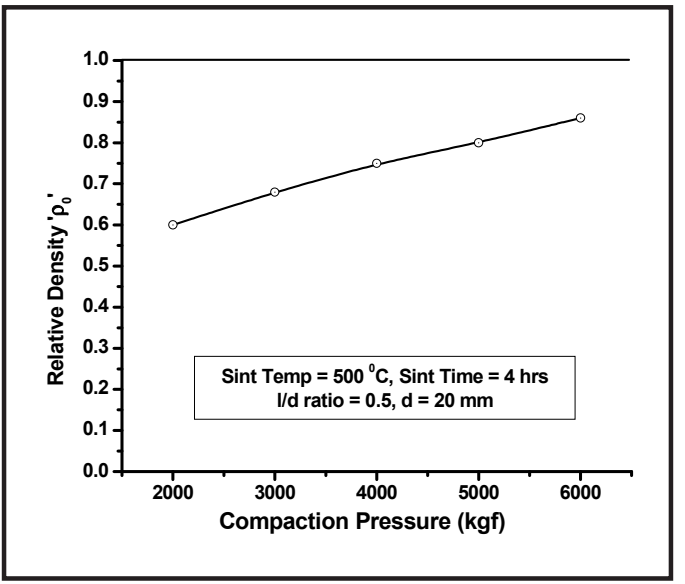

Figure 2.11: Variation of relative density of preform with compaction pressure.

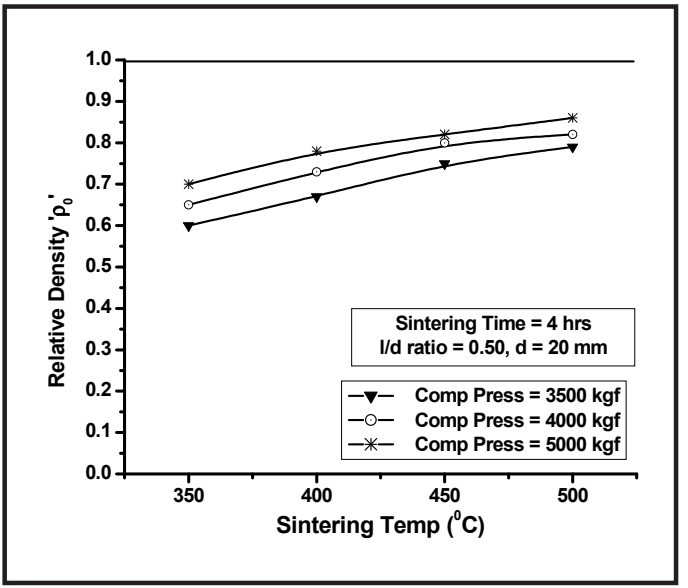

Figure 2.12: Variation of relative density of preform with sintering temperature.

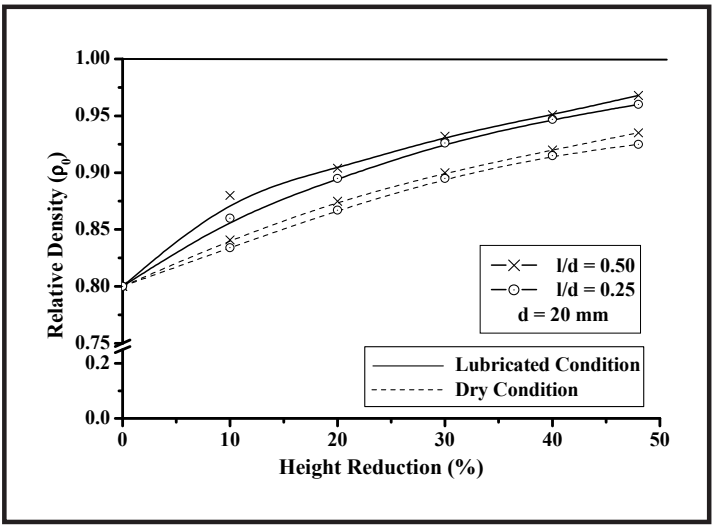

Figure 2.13: Variation of relative density of preform with preform height reduction.

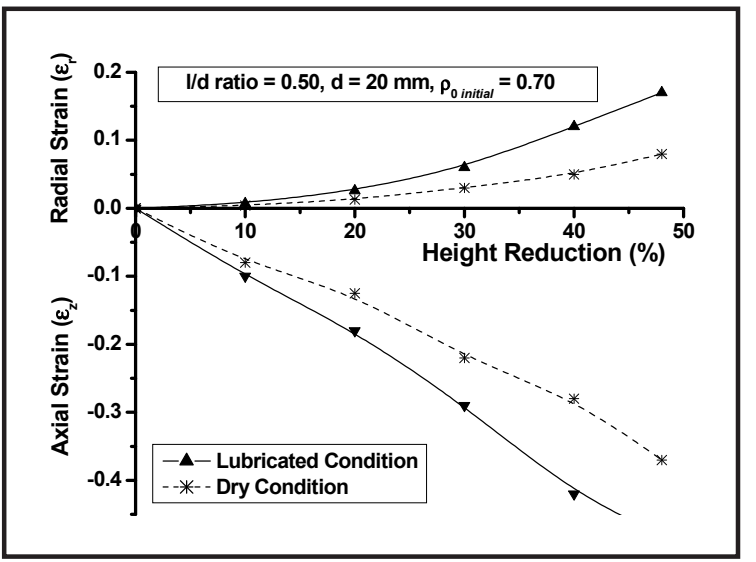

Figure 2.14: Variation of radial & axial strains with preform height reduction.

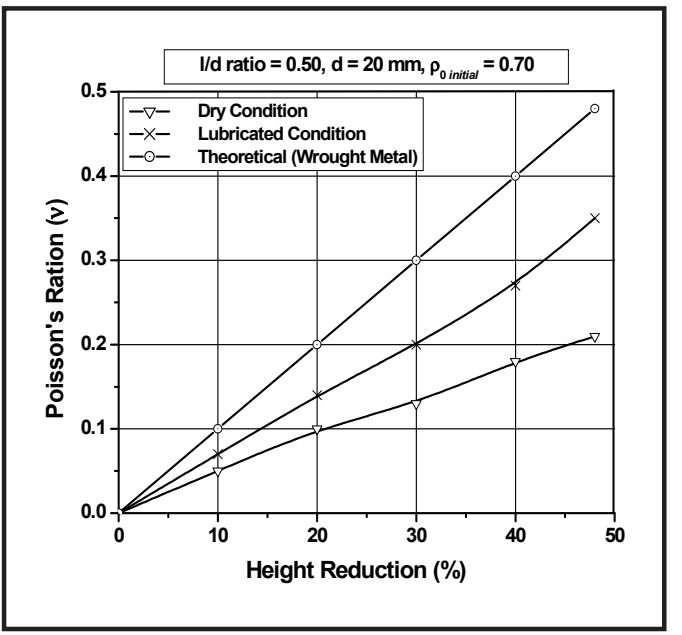

Figure 2.15: Variation of Poisson's ratio with preform height reduction.

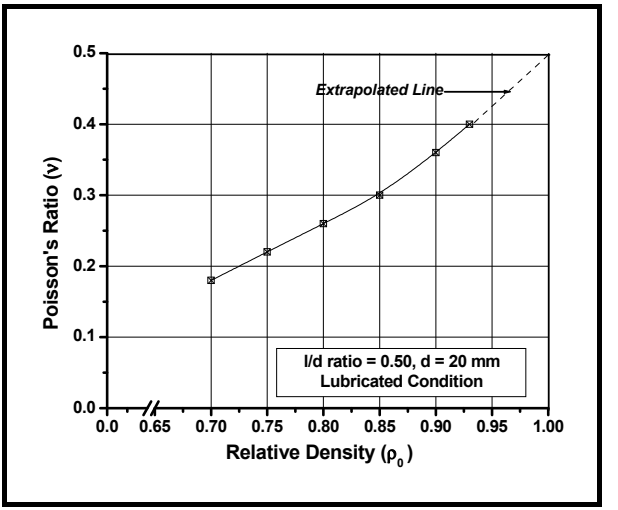

Figure 2.16: Variation of Poisson's ratio with preform relative density.

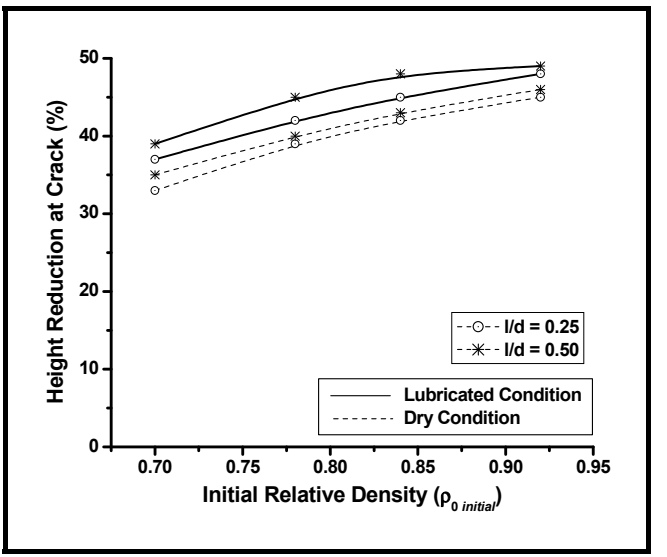

Figure 2.17: Variation of forgeability of preforms with initial relative density.

Figure 2.18 shows that the densification rate with preform relative density. Densification rate is defined as the ratio of change in preform relative density with change in axial strength. The densification rate decreases with increase in relative density. This is because as preform are more densified; their resistance to further deformation increases at same forging condition leading to decrease in the rate of densification.

Figure 2.19 it is variation of axial strain with forging load. It can be seen from figure that axial strain increases with the forging load but the curve is not similar to that of wrought materials and steels. The curve is below the curve for steels, which is due to the porosity present in the powder performs. During the sinter forging process, the compaction of preform occurs simultaneously with the compression, where compaction leads to closing of pores and preform densification, whereas, compression leads to deformation of the preform. It is due to this phenomenon, some amount forging load and energy are expended for the densification of the preform, which is also confirmed by *Huppmann [1977]*.

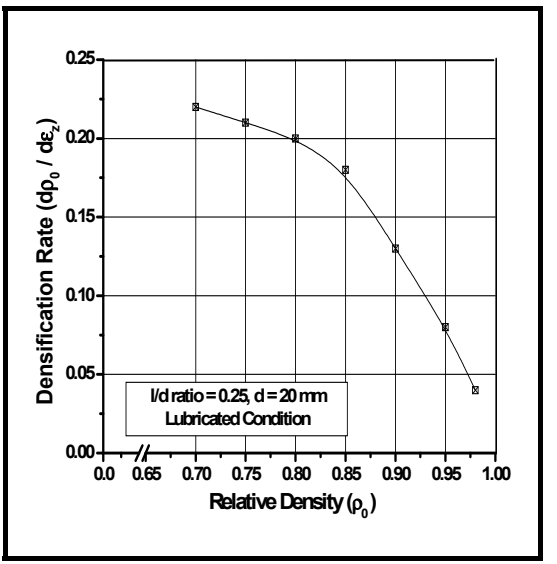

Figure 2.18: Variation of densification rate of preforms with relative density.

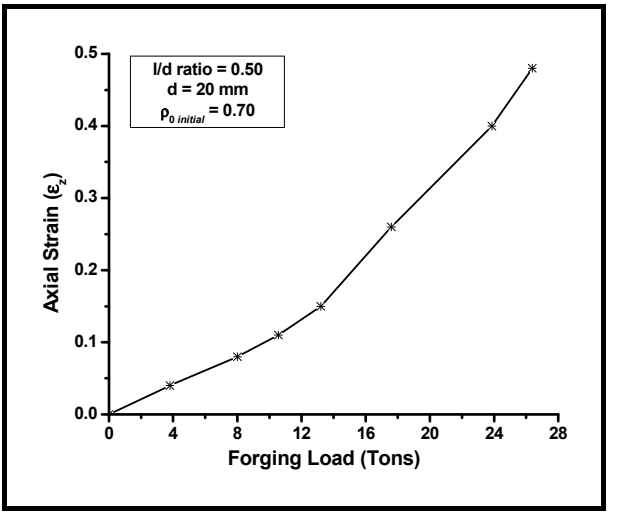

Figure 2.19: Variation of axial strain with forging load.

Figure 2.20 (a) & (b) shows the variation of outer and inner diameters with height reduction during open-die sinter-forging of hollow disc preform. It is evident from the figures that percent change in diameters of hollow disc preform decreases with increase in die velocity. This is because higher die velocity results into impact loading due to small contact time and leads to higher densification of preform, as compared to sinter-forging operations at slow speeds. Also, the percent change in inner radius of hollow disc preform is observed to be small at low interfacial friction condition. This is so because, the position of neutral radius is in between outer and inner radii of hollow disc preform for low interfacial friction condition and the preform material in between inner and neutral radii, flows inwards and the rest flows outwards, resulting into small change in the inner radius. This has also been confirmed by recording and tracing the bulged profiles of hollow disc preforms by an optical projector with 10X magnification under dry and lubricated friction conditions as shown in figures 2.21 (a) & (b).

Figure 2.22 shows the variation of small and large radii with height reduction during open-die sinter-forging of truncated conical preform. It can be seen from the figure that percent change in smaller diameter is higher than that of larger diameter for same die velocity. It is due to higher interfacial friction at the larger end of preform. Thus, it is concluded that the deformation during sinter-forging of truncated conical preform is primarily concentrated at its smaller radius. The percent changes in the dimensions has been observed to be lower for higher deformation speeds, which indicates that compression dominates

over compaction during sinter-forging operations, especially at higher die velocities.

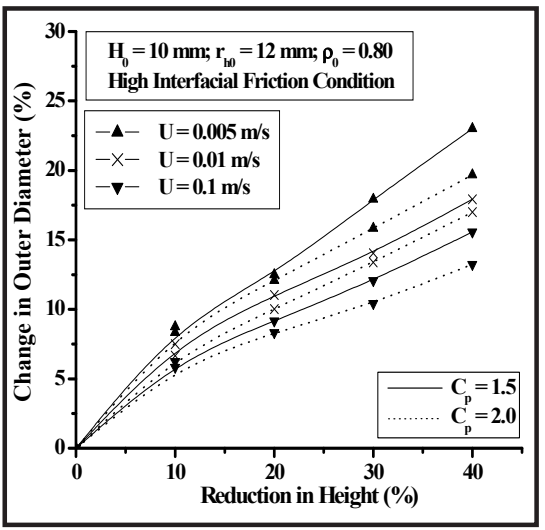

Figure 2.20 (a): Variation of outer diameter with height reduction during open-die sinter-forging of hollow disc preforms.

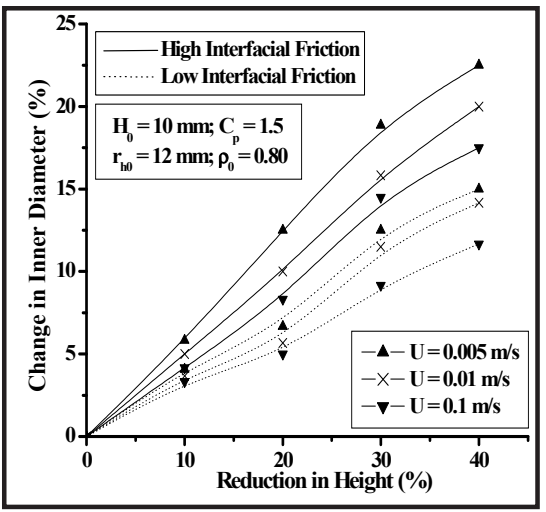

Figure 2.20 (b): Variation of inner diameter with reduction in height during open-die sinter-forging of hollow disc preforms.

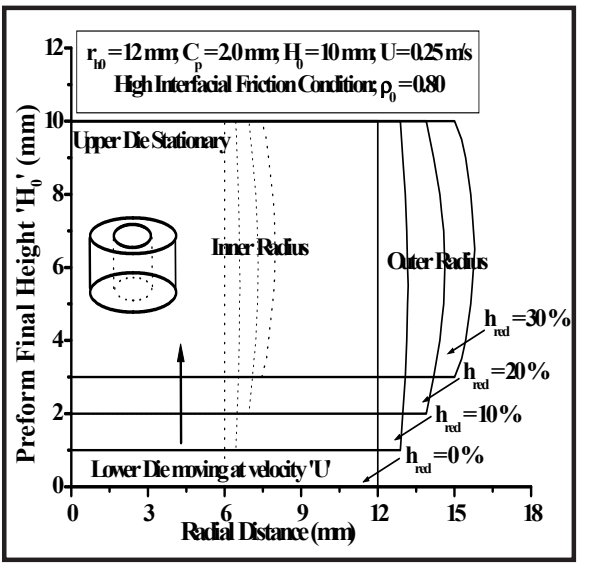

Figure 2.21 (a): Bulged profile of hollow disc preform during open-die sinter-forging under high interfacial friction condition.

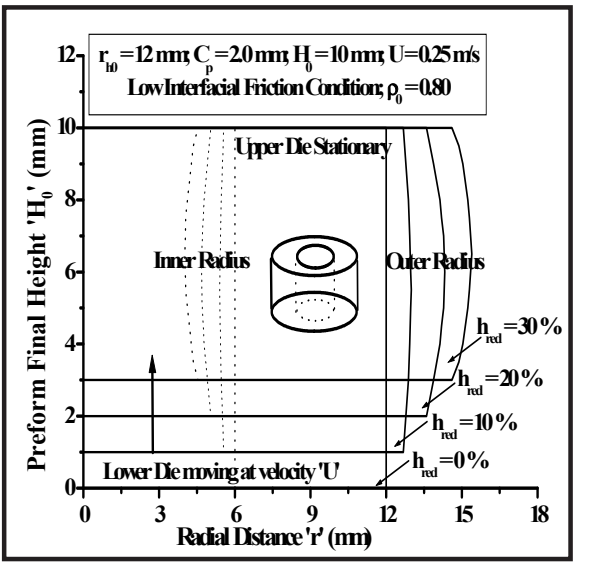

Figure 2.21 (b): Bulged profile of hollow disc preform during open-die sinter-forging under low interfacial friction condition.

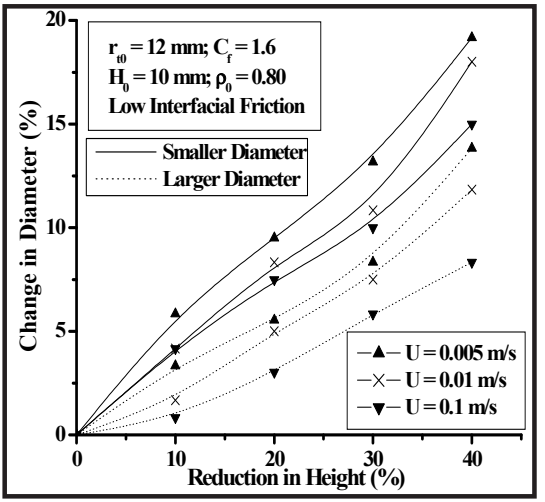

Figure 2.22: Variation of small & large radii with reduction of height during open-die sinter-forging of truncated conical preform.

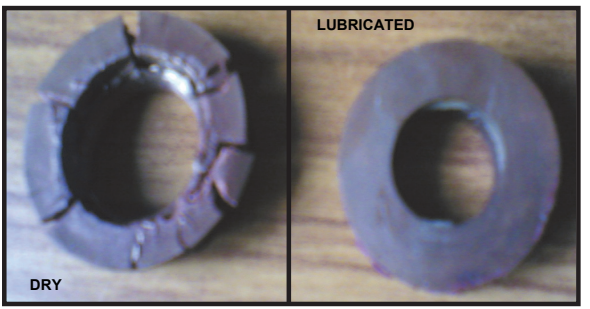

Figure 2.23: Electrolytic copper metal powder hollow disc preforms sinter-forged under dry & lubricated interfacial friction conditions.

Figure 2.24: Aluminium metal powder truncated conical preforms sinter-forged under dry & lubricated interfacial friction conditions.

The copper metal powder hollow disc and Aluminium metal powder truncated conical preforms sinter-forged under dry and lubricated interfacial friction conditions respectively are illustrated in figures 2.23 & 2.24 respectively. It is clearly seen that the sintered preforms forged under dry interfacial friction conditions exhibits considerably reduced metal flow and severe cracking. Figure 2.25 shows the illustration of Aluminium metal powder irregular polygonal preforms before and after open-die sinter-forging respectively under lubricated interfacial friction conditions. It has been observed during experimentation that the initial shapes of regions inscribed on the preform surface remains unchanged after deformation, which confirmed that there is no velocity jumps or discontinuities across the proposed regions. During flashless closed-die sinter-forging of double-hub flange components, cylindrical preforms with known initial relative density of 0.75 approximately were kept inside the closed-die set and compressed on an ultimate tensile machine. The cylindrical recess-cavities on upper and lower punches of die set assured correct centric location of preforms and avoided the application of eccentric die loads.

The variation in height reduction with die velocity for different preform aspect ratio during flashless closed-die sinter-forging has been recorded and is displayed in figure 2.26. It is evident from figure that preform height reduction increases with die velocity. Also, the preform with higher aspect ratio exhibits higher percent reduction in height. This indicates that during uniaxial compression, slender preforms deforms comparatively more than shorter preforms under same die loads.

Rotary sinter-forging of axi-symmetric disc with known initial relative density of 0.70 has been performed using an upper conical die with skew contact angle of 10^0 as shown in figure 2.27. The variation of indentation load with indentation depth for different die velocity has been recorded and shown in figure 2.28. It can be seen from the figure that die load increases with indentation depth because higher loads are required by upper conical die to penetrate into the preform surface. It has been observed that the die load requirement decreases with increase in die velocity due to shorter contact times under deformation.

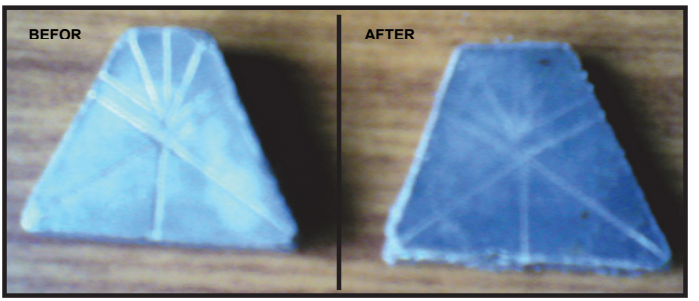

Figure 2.25: Aluminium metal powder irregular polygonal preforms before & after sinter-forging under lubricated interfacial friction conditions.

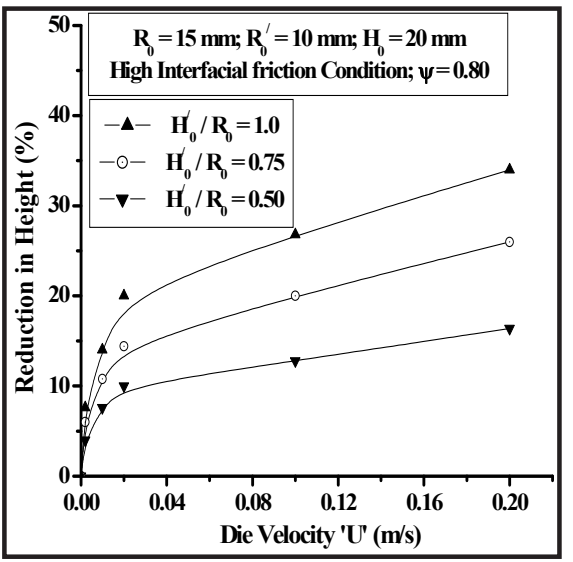

Figure 2.26: Variation of height reduction with die velocity during flashless closed-die sinter-forging operation.

Figure 2.27: Rotary sinter-forging of powder preform.

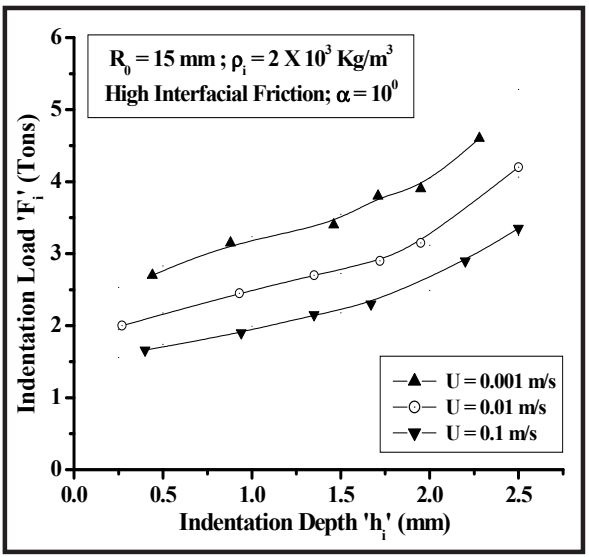

Figure 2.28: Variation of indentation load with indentation depth for different die velocity during rotary sinter-forging.

Figure 2.29 (a) & (b) are the illustrations showing variations of indented area on the preform surface during indentation and rotary phases of rotary sinter-forging respectively. It is clearly evident from the figures that indented areas grow in size with increase in die load, as the upper conical die sweep through the preform surface.

Figures 2.20 shows the photomicrograph of pores on top surface of Aluminium powder preforms sintered at 400^0 C temperature for four hours at 0, 15, 30 and 40 percent of height reductions respectively. It is clearly apparent from the figures that powder particles consolidate and pores close down with the application of compressive load during progress of sinter-forging process. Also, the compaction *i.e.* densification of preform takes place simultaneously with the compression, *i.e.* deformation.

The densification behavior of metal powder preforms has been investigated by noting the changes in relative density of preforms at regular intervals of die load increment and height reduction. Figure 2.31 shows the variation in preform relative density with height reduction for different die velocity and shape-complexity factor during open-die sinter-forging of hollow, truncated conical and irregular polygonal preforms. It is evident from the figure that preform relative density increases with percent height reduction and die velocity and becomes almost comparable to that of the corresponding wrought materials at the end of sinter-forging operation. The sinter-forging process at high die speeds gives impact loading to preforms resulting into better densification, as compared to preforms forged at lower die speeds. This demonstrates the predominance of compaction over compression during sinter-forging processes, especially at higher die velocities. Also, the magnitude of densification has been seen to vary from high to low, in the sequence of irregular polygonal, truncated conical and hollow disc preforms respectively. This is so because, hollow preform exhibits better metal flow in lateral or radial direction, as compared to the truncated conical and irregular polygonal preforms.

Figure 2.29 (a): Indented area after indentation phase of rotary sinter-forging.

Figure 2.29 (b): Indented area after rotary phase of rotary sinter-forging.

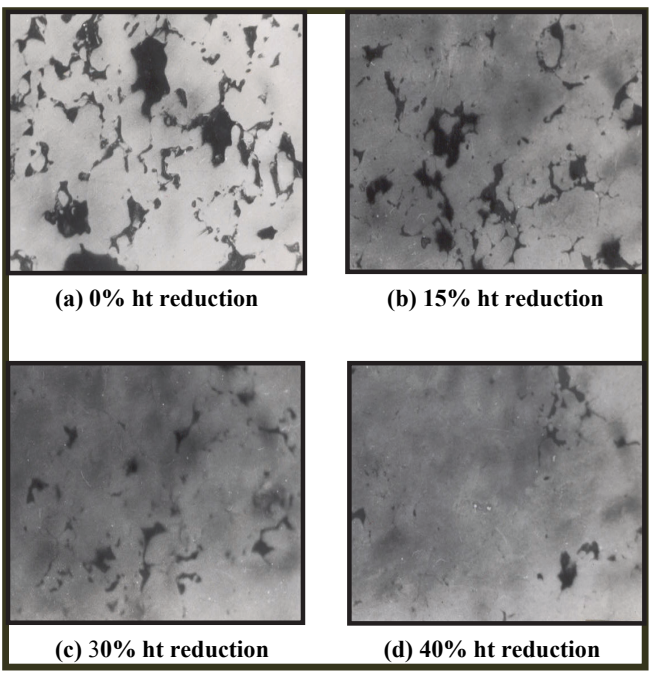

Figure 2.30: Photomicrographs of pores on the top surface of Aluminium powder preforms with different percent of height reductions.

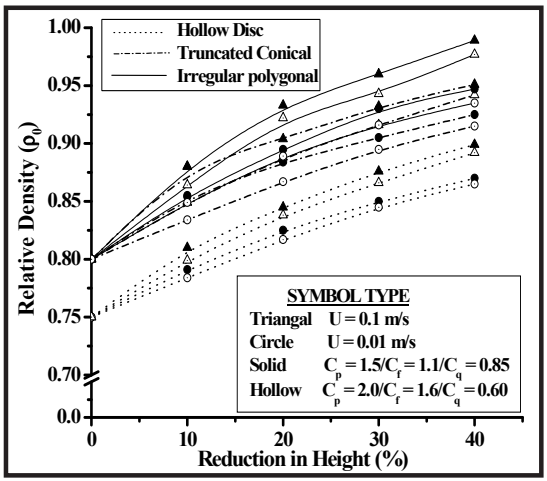

Figure 2.31: Variation of relative density with height reduction for hollow disc, truncated conical and irregular polygonal preforms for different die speed & shape-complexity factor.

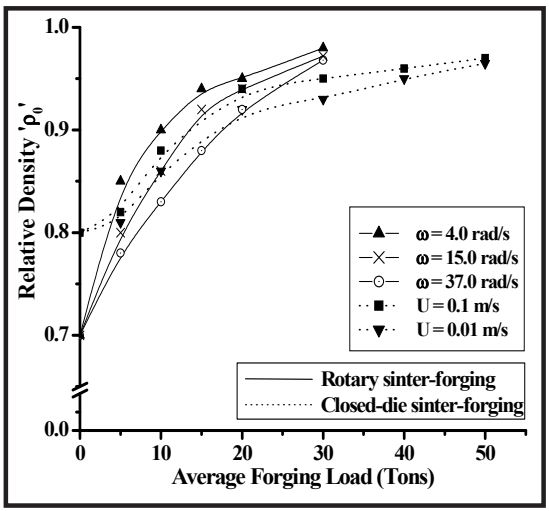

Figure 2.32: Variation of relative density with height reduction during closed-die & rotary sinter-forging operations.

The changes in relative density and percent reduction in the height along with the corresponding die loads during closed-die and rotary sinter-forging has been recorded and is displayed graphically in figure 2.32. The relative density of preform is found to increase with die load and die-cavity fills, as it flows along the container and die-wall constraints during closed-die sinter-forging operation. It is also evident from the figure that relative density of preforms increases with decrease in angular velocity of upper conical die, which is attributed due to the predominant dynamic effects exhibited during the rotary sinter-forging process.

Figure 2.33 shows the variation of final die load with die velocity for hollow, truncated conical and irregular polygonal preforms under dry interfacial friction conditions. It can be seen that die load decreases with increase in die velocity. Sinter-forging operations with higher die speeds are characterized by very small contact time under deformation. The low duration of intimate contact between preform and die restricts the internal heat generated due to plastic working to dissipate quickly and hence, reduces the preform resistance against deformation. It is observed that irregular polygonal preform requires higher die load to deform than truncated conical preform, which in turn needs still higher load than hollow disc preform. Also, the die loads required to deform square, cylindrical and solid disc preforms is high as compared to triangular, conical and hollow disc preforms respectively for the same amount of material.

The variation in die load to completely fill the die cavity impressions during closed-die sinter-forging for different die velocity and preform aspect ratio of 0.5 and 1.0 has been recorded and is shown in figure 2.34. The unfilled volumes of die cavity were calculated by measuring unfilled corners of deformed preforms. It is clearly apparent from the figure that die load increases exponentially during final stages of die fill due to high constraint deformation and resistance against metal flow. Also, the die load required for complete die fills is higher for slender preforms, as compared to shorter preforms. This appears to be mainly of two prominent consequences. First, the corner geometry differs with preform aspect ratio, due to difference in barrelling during free upsetting stage of deformation. Second, the preform with lower aspect ratio has lower contact areas with container walls and hence, exhibits lower frictional resistance during deformation. It can also be noted that die load decreases with increase in die velocity, *i.e.* dynamic effects.

The present experimental study has revealed that preform formability, die load and die velocity are related to each other in a complex manner during sinter-forging processes. This necessitates an investigation to study the effect of die velocity, *i.e.* dynamic effects on the preform height reduction and die load simultaneously. To study this effect, a factor *'Load Ratio'* has been introduced in the present work, which has been defined as the ratio of die loads at U = 0.001 and 0.25 m/s respectively (minimum and maximum die speeds available on the mechatronic press used in the present study).

Figure 2.35 shows the variation of load ratio with percent height reduction of preform, up to 42% of height reduction, which is the maximum formability of sintered materials observed during present study. It is clearly evident from the figure that load ratio increases with percent height reduction and reaches to unity at about 20% height reduction. The values of load ratio higher than unity indicates that die load at U = 0.25 m/s is smaller than die load at U = 0.001 m/s for all other deformations conditions remaining same. This indicates that die loads are higher for higher die velocity, *i.e.* U = 0.25 m/s, as compared to the die loads at U = 0.001 m/s, till 20% of preform height reduction. Thereafter, there is drastic decrease in the die load with increase in the die velocity. This is due to the predominance of strain rate effect and reduced chilling during preform height reduction more than 20%. The rate of decrease in die load also slightly decreases about maximum preform formability, probably due to the onset of fracture. In the present case, the reductions in the die loads is significant only after 20% of preform height reduction, which may vary with the two limits of the die velocities considered to define the load ratio. The above two die velocities were selected merely on the basis of availabity of die speeds on the mechatronic press considered during present investigations.

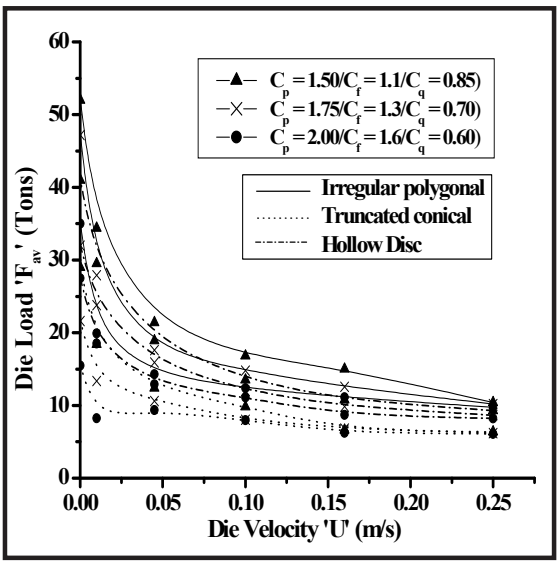

Figure 2.33: Variation of die load with die velocity for hollow disc, truncated conical & irregular polygonal preforms during open-die sinter-forging operation.

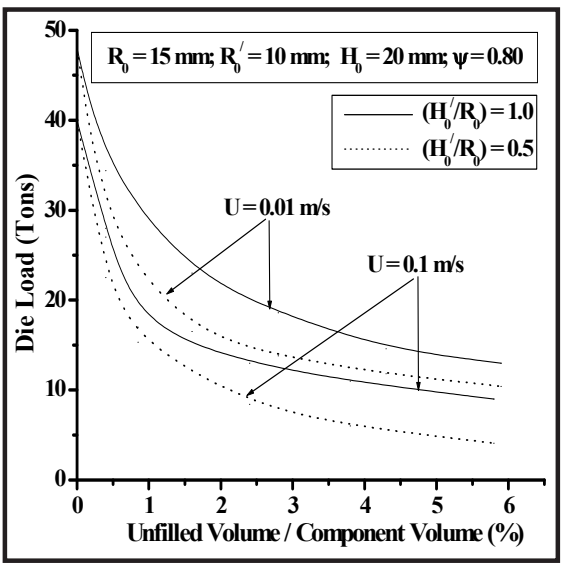

Figure 2.34: Variation of die load with ratio of unfilled volume to component's actual volume during flashless closed-die sinter-forging operation.

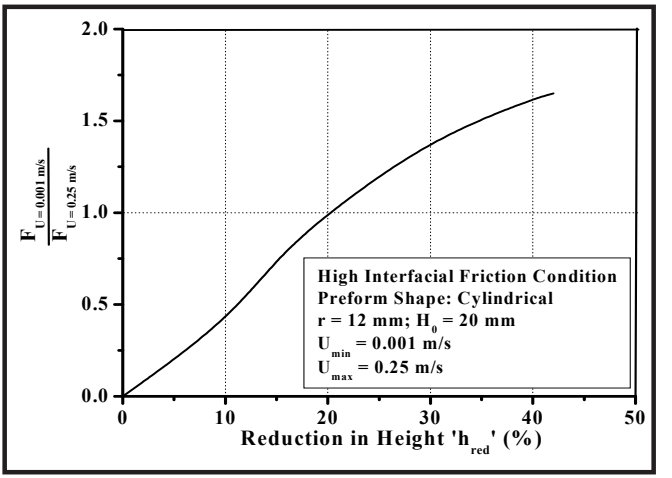

Figure 2.35: Experimental variation of load ratio with percent height reduction during open-die sinter-forging of cylindrical preform.

CHAPTER - 3
OPEN DIE FORGING OF SINTERED PREFORMS

Outline of the Chapter: *3.1 Sinter-Forging of Truncated Conical Powder Preform; 3.1.1 Velocity Field & Strain Rates*
3.1.2 Energy Dissipations & Average Die Load; 3.1.3 Average Bulged Profile; 3.1.4 Results & Parametric Discussion; 3.2 Sinter-Forging of Irregular Polygonal Powder Preform; 3.2.1 Velocity Field & Strain Rates; 3.2.2 Energy Dissipations & Average Die Load; 3.2.3 Results & Parametric Discussion

The deformation pattern during sinter-forging process is influenced by several important factors like preform density, strength, elongation, barreling, shape-complexity, temperature, flow stress and die-workpiece interface frictional conditions, die velocity and acceleration, as well as factors related to forging equipment, like deformation speed and contact times under load. The problem lies in recognition of these important factors, which interact with each other in a complex manner and estimation of dynamic effects, which critically influence the average die load involved during sinter-forging process, especially at higher die velocities.

A very few investigators have carried out research into dynamic effects during mechanical processing of wrought materials. *Lippmann* [*1966*] carried research to generalize the elementary theory of plasticity for the case of forging with high acceleration, when inertia effects can no longer be neglected. The analysis based on equilibrium approach considers high-speed compression of a specimen between plane rigid parallel platens of a hydraulic press up to relative die velocity of about 7 m/s. According to investigations, the dynamic effects can occurs in three ways. Firstly, when die with a certain relative velocity before the beginning of deformation loses a part of it by the impact, during which the specimen gets the kinetic energy. In this case, the entire forging operation is considered as one plastic impact. Secondly, during the real deformation processes, the die velocity reduces to zero and initially accumulated kinetic energy supports the plastic flow with diminishing forging force. Lastly, the negative forces have also formally generated, which in reality has moved the specimen away from the dies and thus, deformation proceeds only by means of specimen's own kinetic energy.

Hilllier [*1966*] estimated the dynamic forces in case of very high-speed impact forging of disks and slabs under axi-symmetric and plane strain condition respectively with both smooth and perfectly rough dies. The analysis considered coulomb friction law and three methods of analysis, *e.g.* approximate equilibrium approach, energy method and upper-bound approach based on kinematically admissible velocity field. The strain hardening, strain rate and temperature effects were neglected. The material was assumed to be homogeneous and isotropic and yield stress value was adjusted to take into account of strain rate, strain hardening and temperature suitably for all practical purposes. The material was considered to be incompressible, *i.e.* elastic strains were neglected and obeys Von Mises yield criterion. The inertia forces normal to the die face were considered to be negligible compared to inertia forces parallel to the die face. The dynamic effects were illustrated by calculating the die velocity required to double the maximum die pressure, as compared with a slow static forging.

Osakada K. *et al.* [*1971*] carried experimental investigations to study the impact of dynamic effects on the mechanical properties of mild steel specimen during cold and warm high-speed forging under plane strain condition. The effect of deformation speed, strain and temperature on yield stress, flow stress, ultimate tensile stress, work hardening, elongation, cross-section reduction and hardness of mild steel specimen during high-speed forging were critically studied, discussed and results were compared with those after low-speed forging. It was concluded from the investigations that at room temperature, high-speed forging showed lower yield stress, ultimate tensile stress and hardness than low-speed forging. Consequently, higher values of elongation, reduction in area and impact strength was obtained. The impact strength values of high-speed forging are greater than those of low-speed forging with same hardness, although the tensile test results exhibit same values for the same hardness. It was observed that yield stress and hardness of high-speed forging were lower than those of low-speed forging at forging temperatures up to 400^0 C and the relation was reversed at temperatures above 400^0 C.

Chitkara & Bhutta [*2001*] estimated the dynamic forces during high-speed impact forging process. *Dean* [*1970*] reported investigations into influence of billet inertia and dry friction during forging processes using a simple energy approach. *Jain and Bramley* [*1968*] carried extensive study of the characteristics of high-speed forging process. It was found that high-energy rate forging and its conventional counterpart should be compared on the basis of five factors, *e.g.* cycle time, efficiency of energy transfer, dwell time, die bounce

characteristics and die closing speed. In case of high-speed forging deformation is completed in shorter time and frictional resistance is found to reduce and hence, lubrication at high-speed is found to be more effective. The high die closing speed is the most significant factor in case of high-energy rate forging machines, which is in the order of 12-25 m/s. It was found that energy absorbed by the billet during high-speed forging is approximately 50 m-kgf higher than that at low-speed forging for 40 percent height reduction of billet. Also, the maximum loads at high-speed deformation are higher than low-speed deformation.

Tobias et al. [*1968a, 1968b*] studied the effect impact of die speed and lubrication conditions on interfacial friction conditions, die pressure, metal flow pattern, die cavity fill and required forging load during high-speed hot forging process. Four different interfacial friction conditions were considered using copaslip, graphite, clean dry dies and lightly oxidized billets. Ring test were employed to determine the frictional restraints at billet-die interface during metal flow. It was concluded from the investigations that for a given condition of lubrication, the coefficient of friction decreases with increased with impact velocity and depends modest on the change in die velocity during deformation. The frictional forces are lowest for copaslip and graphite lubricants in case of Petro-Forge machines and hydraulic press respectively, though pressure rise was observed highest using copaslip. The deformation load required to upset ring specimens increases with interfacial friction and lower upsetting load were required using copaslip than graphite lubricant.

The above literature survey suggests that lots of researchers have carried extensive investigation for the estimation of dynamic effects during forging of wrought metals. Also, many researchers have addressed the problems of mechanical processing of sintered porous materials having different simple shapes from various technical aspects, but not much systematic attempt has been made so far to study the dynamic effects involved during sinter-forging of components, especially at higher die velocities with complicated generic shapes. Since, die speed and acceleration are the most significant factors, attention should be to study the effect of these factors on overall die load and associated strain rates. Thus, it could be understood that there is a need to carry a systematic research to analyze dynamic effects during mechanical processing of sintered materials. The present chapter is an attempt to analyze these dynamic effects during various sinter-forging processes at cold conditions.

The chapter deals with *'Upper Bound'* analysis of open-die forging, flashless closed-die forging and rotary sinter-forging of metal powder preforms at high deformation speed. Preforms with two different generic shapes *i.e.* truncated conical and irregular polygonal have been considered under open-die sinter-forging process in the first section of the chapter. The second and third sections deal with flashless closed-die sinter-forging of cylindrical preforms into double-hub flange components and rotary sinter-forging of axi-symmetric preforms respectively.

In all the cases, the exponential velocity field and corresponding strain rates have been formulated within the deforming preforms based on boundary conditions and compatibility equations established in the first chapter. Thereafter, the generalized expressions for internal, frictional shear and inertia energy dissipations based on *'Upper Bound'* approach have been established. Finally, the average die load required to deform the preforms has been computed during respective sinter-forging processes.

The influence of die velocity, acceleration, preform aspect ratio and skew contact angle of upper conical die on inertia energy dissipations, die loads, final bulged shape of preforms, strains at preform free surfaces, respective strain rates and their interrelationships, die cavity fills and indentation depths have been investigated and displayed graphically. The theoretical results of dynamic effects, *i.e.* effect of die velocity and acceleration on the die load requirements during sinter-forging processes have been compared with corresponding experimental results and are found to be in close agreement. The preform shape variations have been incorporated in the present study by introducing shape-complexity factors, so that the effect of preform shape variations on various deformation characteristics during sinter-forging processes could be studied.

To study and investigate the dynamic effects of die velocity and acceleration during mechanical processing of sintered materials, two vital factors, *i.e.* inertia factor *'ξ'* and load factor *'ζ'* have been introduced in the present analyses. The inertia factor has been expressed as the ratio of inertia energy dissipation to total external energy supplied by press die platens and gives the measure of proportionate change in inertia energy dissipated with respect to total energy supplied by the external die platens. The load factor has been defined as the ratio of difference of die loads with and without dynamic effects to die load with dynamic effects.

It has been found that magnitude of inertia factor increases exponentially with die velocity and hence, inertia energy dissipation becomes comparable with other energy dissipations considered during sinter-forging operations. Thus, it has been concluded that inertia energy dissipations should be considered during analysis of sinter-forging processes, especially at higher die velocity for accurate and realistic measure of die loads. The load factor has been found to decrease with die velocity, which indicates that die load required for deformation of sintered preforms decreases with die velocity. This is attributed due to very low die-preform contact time under die load due to high deformation speed, which restricts the dissipation of internal heat generated due to plastic working of preforms and leads to decrease in the resistance of sintered materials against deformation.

The present analyses involves some assumptions related to sinter-forging processes, in addition to usual assumptions considered during conventional-forging operation, which are as follows [*Jha, 1996; Sutradhar et al. 1997*]:

a. The deformation behavior during sinter-forging is inhomogeneous and bulging of preform's vertical sides has been considered during analyses by including a barreling parameter in exponential velocity fields within the deforming preforms.

b. The interfacial friction due to adhesion is a function of relative density and adhesion factor only, which increases asymptotically with the increase in real area of contact between preform and die during sinter-forging operations.

c. The compression (yielding) of sintered preforms takes place simultaneously with the compaction (closing of pores) and hence yielding is sensitive to the imposed hydrostatic stress component. Thus, a yield criterion sensitive to hydrostatic stress component and suitably applicable during mechanical processing of sintered materials, *i.e.* Tabata & Masaki yield criterion has been considered.

d. The change in preform volume during mechanical processing of sintered materials due to closing of the pores, rules out the application of volume constancy principle. Therefore, the compatibility equations have been derived from volume inconstancy principle using Tabata & Masaki yield criterion and strain increment equations.

e. The lateral or circumferential flow of preform sides has been neglected during the sinter-forging analyses.

f. The stress wave propagation effect has been neglected, as it is assumed that the transit time of stress waves to travel through the powder preforms during sinter-forging operations considered under present analyses are considerably long.

3.1 SINTER-FORGING OF TRUNCATED CONICAL POWDER PREFORM

The analysis of open-die sinter forging of truncated conical preform considers one additional assumption apart from the common assumptions. It states that bulging of truncated conical preform is concentrated at smaller radius and theoretically approaches to zero, when larger radius becomes infinitively long *[Gokler et al., 1999]*.

3.1.1 Velocity Field & Strain Rates

Consider open-die sinter-forging of a truncated conical preform at cold conditions between two perfectly flat, parallel and rigid die platens with lower die platen moving upwards with velocity *'U'* and upper die platen stationary as shown in figure 3.1. The compatibility equation [Refer Equation A.9 in Appendix] and boundary conditions are given as:

$$\dot{\varepsilon}_{rr} + \dot{\varepsilon}_{\theta\theta} + \left(\frac{1-2\eta}{1+\eta}\right)\dot{\varepsilon}_{zz} = 0 \qquad \text{(A.9)}$$

$U_z = U \quad \text{at} \quad z = 0$ (3.1)

$U_z = 0 \quad \text{at} \quad z = H_0$ (3.2)

The velocity field and corresponding strain rates satisfying equations (4.13), (3.1) and (3.2) are given as [Refer Appendix B]:

$$U_r = \left[\frac{(1-2\eta)\beta e^{-\beta z/H_0} Ur}{2(1+\eta)\left(1-e^{-\beta}\right)H_0}\right] \qquad (3.3)$$

$$U_z = -\left[\frac{\left(e^{-\beta} - e^{-\beta z/H_0}\right)U}{1-e^{-\beta}}\right] \qquad (3.4)$$

$$U_\theta = 0 \qquad (3.5)$$

$$\dot{\varepsilon}_{rr} = \left[\frac{(1-2\eta)\beta e^{-\beta z/H_0} U}{2(1+\eta)\left(1-e^{-\beta}\right)H_0}\right] \qquad (3.6)$$

$$\dot{\varepsilon}_{zz} = -\left[\frac{\beta e^{-\beta z/H_0} U}{H_0\left(1-e^{-\beta}\right)}\right] \tag{3.7}$$

$$\dot{\varepsilon}_{\theta\theta} = \left[\frac{(1-2\eta)\beta e^{-\beta z/H_0} U}{2(1+\eta)\left(1-e^{-\beta}\right)H_0}\right] \tag{3.8}$$

$$\dot{\varepsilon}_{rz} = \frac{1}{2}\left(\frac{\partial U_r}{\partial z}+\frac{\partial U_z}{\partial r}\right) = -\left[\frac{(1-2\eta)\beta^2 e^{-\beta z/H_0} U r}{4(1+\eta)\left(1-e^{-\beta}\right)H_0^2}\right] \tag{3.9}$$

$$\dot{\varepsilon}_{r\theta} = \dot{\varepsilon}_{\theta z} = 0 \tag{3.10}$$

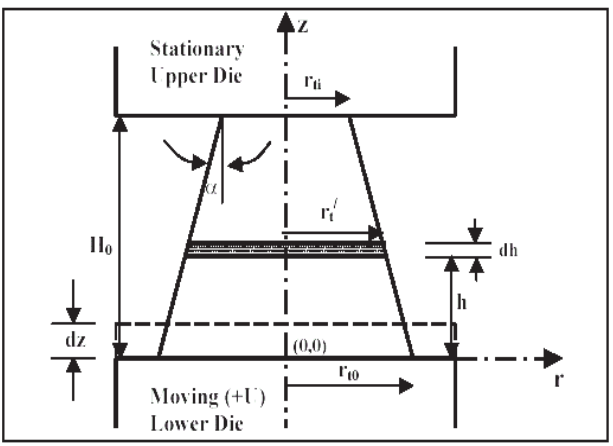

Figure 3.1: Schematic diagram of open-die sinter-forging of axi-symmetric truncated conical preform.

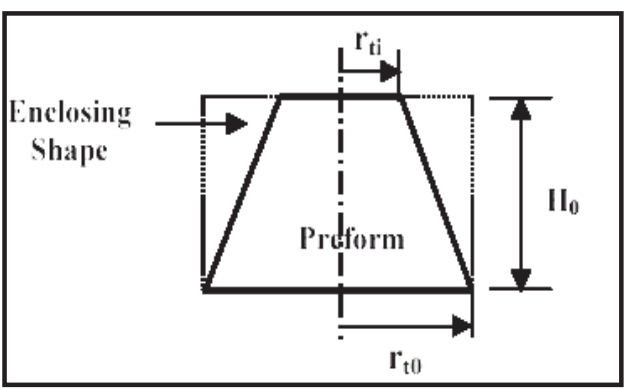

Figure 3.2: Shape-complexity factor for truncated conical preform.

3.1.2 Energy Dissipations & Average Die Load

The total external energy *'J'* supplied by the die platens during plastic deformation of sintered preforms based on *'Upper Bound'* approach is given as [*Singh S. et al., 2002*]:

$$J = \frac{2\sigma_o}{\sqrt{3}}\int_V \sqrt{\frac{1}{2}\dot{\varepsilon}_{ij}\dot{\varepsilon}_{ij}}\,dV + \int_S \tau\left|\Delta U\right| dS + \int_V \rho_p\left(a_i U_i\right) dV \qquad (3.11)$$

The first term on right side denotes internal energy dissipation *'W_i'*, the second term denotes frictional shear energy dissipation *'W_f'* and the last term denotes energy dissipation due to inertia forces *'W_a'*. The internal energy dissipation *'W_i'* during open-die sinter-forging of truncated conical preform is given as:

$$W_i = \left(\frac{2\sigma_0}{\sqrt{3}}\right)\int_V\left(\sqrt{\frac{1}{2}\dot{\varepsilon}_{ij}\dot{\varepsilon}_{ij}}\right)dV$$

$$= \left(\frac{2\sigma_o}{\sqrt{3}}\right)\int_{z=0}^{z=H_0}\int_{r=r_{ti}}^{r=\left(r_{ti}+H_0\tan\alpha'\right)}\left[\sqrt{\dot{\varepsilon}_{rr}^2+\left(\frac{\dot{\varepsilon}_{zz}^2+\dot{\varepsilon}_{rz}^2}{2}\right)}\right]\left(2\pi r dr dz\right) \qquad (3.12)$$

Substituting equations (3.6) to (3.10) above, solving and simplifying, the internal energy dissipation may be expressed as:

$$W_i = \left[\frac{8\pi\sigma_o U\left(\psi-2\right)^{1/2}H_0^2}{3\sqrt{3}\beta^2}\right]\left[\psi+\frac{\beta^2 r_{ti}^2\left(1-\tan^2\alpha'\right)}{4H_0^2}\right]^{3/2} \qquad (3.13)$$

where, $\psi = \left\{2+\left[\frac{2\left(1+\eta\right)}{1-2\eta}\right]^2\right\}$

The frictional shear energy dissipation at die-workpiece interface *'W_f'* during open-die sinter-forging of truncated conical preform is given as:

$$W_f = \int_S(\tau)\left|\Delta V\right| dS = \left\{\begin{array}{l}\int_{r=0}^{r=r_{t0}}\left[\left|\tau\right|_{z=H_0}\left|U_r\right|_{z=H_0}\left(2\pi r dr\right)\right]+ \\ \int_{r=0}^{r=r_{ti}}\left[\left|\tau\right|_{z=0}\left|U_r\right|_{z=0}\left(2\pi r dr\right)\right]\end{array}\right\} \qquad (3.14)$$

The frictional shear stress (assuming pressure term equal to average pressure) during sinter-forging of truncated conical preform at larger and smaller radii respectively is given as [Refer Equation 1.6]:

$$\left|\tau\right|_{z=H_0} = \mu\left\{P_{av}+\rho_0\varphi_0\left[1-\left(\frac{r_{tm}-r}{nr_{t0}}\right)\right]\right\} \qquad (3.15)$$

$$\left|\tau\right|_{z=0} = \mu\left\{P_{av} + \rho_0\varphi_0\left[1-\left(\frac{r_{tm}-r}{nr_{ti}}\right)\right]\right\} \tag{3.16}$$

From equation (3.3), the radial velocity at z = *'H_0'* and z = *'0'* respectively are given as:

$$\left|U_r\right|_{z=H_0} = \left[\frac{(1-2\eta)\beta e^{-\beta}Ur}{2(1+\eta)(1-e^{-\beta})H_0}\right] \tag{3.17}$$

$$\left|U_r\right|_{z=0} = \left[\frac{(1-2\eta)\beta Ur}{2(1+\eta)(1-e^{-\beta})}\right] \tag{3.18}$$

Substituting equations (3.15) to (3.18) into equation (3.14), solving and simplifying, the frictional shear energy dissipation may be expressed as:

$$W_f = \left[\frac{\pi\mu(1-2\eta)\beta U r_{ti}^2}{6(1+\eta)(1-e^{-\beta H_0})}\right]\left\{\begin{array}{l}\left[P_{av} + \rho_0\varphi_0\left(\frac{1}{r_{ti}^3}+\frac{3}{4nr_{ti}^3}\right)\right] \\ x\left(r_{t0}^3 e^{-\beta H_0} + r_{ti}^3\right) \\ -\left(\frac{r_{tm}}{nr_{ti}^3}\right)\left(r_{t0}^2 e^{-\beta H_0} + r_{ti}^2\right)\end{array}\right\} \tag{3.19}$$

The energy dissipation due to inertia forces *'W_a'* during open-die sinter-forging of truncated conical preform is given as:

$$W_a = \int_V\left[\rho_i\left(a_i U_i\right)\right]dV$$

$$= \int_{z=0}^{z=H_0}\int_{r=ti}^{r=\left(r_{ti}+H_0\tan\alpha'\right)}\left[\rho_i\left(a_r U_r + a_z U_z\right)\right](2\pi r dr dz) \tag{3.20}$$

where:

$$a_r = \left[U_r\frac{\partial U_r}{\partial r} + U_z\frac{\partial U_r}{\partial z} + \frac{\partial U_r}{\partial t}\right] \tag{3.21}$$

$$a_z = \left[U_z\frac{\partial U_z}{\partial z} + \frac{\partial U_z}{\partial t}\right] \tag{3.22}$$

Substituting equations (3.3) and (3.4) above and simplifying, one get:

$$\left(a_r U_r + a_z U_z\right) = \left\{ \begin{array}{l} \left\{ \left[\dfrac{(1-2\eta)^2 \beta^3 U^3 r^2 e^{-\beta z/H_0}}{4(1+\eta)^2 \left(1-e^{-\beta}\right)^3 H_0^3} \right] \right\} \\ \left\{ e^{-\beta} - \left[\dfrac{(1+4\eta) e^{-\beta z/H_0}}{2(1+\eta)} \right] \right\} \\ - \left[\dfrac{U^3 \beta e^{-\beta z/H_0} \left(e^{-\beta} - e^{-\beta z/H_0}\right)^2}{\left(1-e^{-\beta}\right)^3 H_0} \right] + U\dot{U} \end{array} \right\} \qquad (3.23)$$

Substituting equation (3.23) into equation (3.20), solving and simplifying, the energy dissipation due to inertia forces may be expressed as:

$$W_a = \left(\pi \rho_i r_{ti}^2\right) \left(\frac{r_{ti}}{H_0} + \tan\alpha' \right)^2 \\ x \left\{ \left\{ \left[\frac{(1-2\eta)^2 \left(r_{ti} / H_0 + \tan\alpha' \right)^2 U^3 \left(1+e^{-\beta H_0}\right)}{64(1+\eta)^2} \right] \right\} + \frac{U^3}{3} + U\dot{U}H_0 \right\} \qquad (3.24)$$

$$\left[1 - \frac{3(1-2\eta)\left(1+e^{-2\beta H_0}\right)}{8(1+\eta)} \right]$$

To study and investigate the effect of shape variation of truncated conical preform on various energy dissipations, die load and strain rates, a concept of shape-complexity factor has been introduced, which is basically a shape distribution function as shown in figure 3.2. It is represented by 'C_f' and defined mathematically as the ratio of larger to smaller radii of truncated conical preform. The value of factor is always greater than one and depends upon the magnitude of smaller and larger radius of truncated conical preform. The factor tends to reduce to unity, when the shape of truncated conical preform approaches to that of an enclosing cylinder, *i.e.* $r_{ti} \approx r_{t0}$. Mathematically, it is expressed as:

$$C_f = \left(\frac{r_{t0}}{r_{ti}} \right) = \left(\frac{r_{ti} + H_0 \tan\alpha'}{r_{ti}} \right) \\ = \left[1 + \left(\frac{H_0 \tan\alpha'}{r_{ti}} \right) \right] \qquad (3.25)$$

Thus, the total energy dissipation during sinter-forging processes is given as:

$$J = \left(W_i + W_f + W_a\right) \qquad (3.26)$$

The average forging load during open-die sinter-forging of truncated conical powder preform may be expressed as follows:

$$F_{av} = J(U)^{-1} A_{av} \tag{3.27}$$

To illustrate the dynamic effects, *i.e.* effect of die velocity on relative magnitudes of various energy dissipations and average die load involved during open-die sinter-forging of truncated conical preform, concepts of inertia factor *'ξ'* and load factor '*ζ*' has been introduced in the present analysis. The inertia factor has been defined as the ratio of inertia energy dissipation to total energy dissipated (in percent) for maximum allowable reduction of preform height and is mathematically expressed as:

$$\xi(\%) = \left(\frac{W_a}{J}\right)100 \tag{3.28}$$

The load factor has been defined as the ratio of difference in die load with and without dynamic effects to die load with dynamic effects (in percent) for maximum allowable reduction of preform height and is mathematically expressed as:

$$\zeta(\%) = \left|\frac{|F_{av}|_{withdynamiceffects} - |F_{av}|_{withoutdynamiceffects}}{|F_{av}|_{withdynamiceffects}}\right|100 \tag{3.29}$$

3.1.3 Average Bulged Profile *[Sahoo & Das, 2003]*

Consider an elemental strip of thickness *'dh'* and radius 'r_t' within the deforming truncated conical sintered preform at a distance *'h'* from lower die platen. Assuming that the lower die has moved through a distance *'dz'* and simultaneously the elemental strip has bulged radially by amount *'δr_t'* in the time interval *'dt'*. Thus, the small compression time interval may be expressed as:

$$dt = \left(\frac{dz}{U}\right) = \left(\frac{\delta r_t}{|U_r|_{z=h}}\right) \tag{3.30}$$

Substituting equation (3.13) and rearranging, the radial bulge may be given as:

$$\delta r_t = \left[\frac{(1-2\eta)\beta e^{-\beta h/H_0} r_t dz}{2(1+\eta)(1-e^{-\beta})H_0}\right] \tag{3.31}$$

Therefore, the final bulged radius of elemental strip within the deforming truncated conical preform is given as:

$$\left(r_t + \delta r_t\right) = r_t \left\{1 + \left[\frac{(1-2\eta)\beta e^{-\beta h/H_0} dz}{2(1+\eta)\left(1-e^{-\beta}\right)H_0}\right]\right\} \qquad (3.32)$$

3.1.4 Results & Parametric Discussion

To illustrate the dynamic effects on magnitude of various energy dissipations, die load and strains rates involved during open-die sinter-forging of truncated conical preform, a typical data of preform and other deformation characteristics has been considered:
H_0 = 17 mm; r_{t0} = 12 mm; β = 0.35; $\rho_0\phi_0 = 0.3P_{av}$; n = 2; ρ_i = 2 x 10^3 kg/m^3; σ_0 = 6.25 kg/mm^2; C_f = 1.6 ($\alpha^/ = 15^0$), 1.3 ($\alpha^/ = 10^0$) and 1.1 ($\alpha^/ = 5^0$); μ = 0.30 (high interfacial friction) and 0.01 (low interfacial friction); Acceleration = 0.1 m/s^2 and 1 m/s^2; U = 0.001 to 10 m/sec.

Figure 3.3 shows the variation of inertia energy dissipation with die velocity for different shape-complexity factor and acceleration under high interfacial friction condition during open-die sinter-forging of truncated conical preform. It is apparent from the figure that inertia energy dissipation increases exponentially with the increase in dynamic effects, *i.e.* die velocity and acceleration and becomes comparable with internal and frictional shear energy dissipations during sinter-forging operation, especially at higher die velocity. Thus, the magnitude of inertia energy dissipation is fairly appreciable during mechanical processing of sintered materials at high die speeds and must be considered during *'Upper Bound'* analysis for accurate measure of die loads. The inertia energy dissipation curves are also higher for low shape-complexity factors, which indicate that as the shape of the truncated conical preform approaches to that of an enclosing cylinder, energy dissipated in the form of inertia forces also increases. Hence, cylindrical preforms require more inertia energy for deformation, as compared to conical ones for the same amount of preform material.

Figure 3.4 shows the experimental and theoretical variation of die load with die velocity under high interfacial friction condition for different shape-complexity factor. It is evident from the figure that die load decreases rapidly with the increase in die velocity. This is due to short contact time under deformation during sinter-forging operation at higher die velocity. The requirement for load is higher for preform with low shape-complexity factor and high initial relative density. Thus, more densified unlubricated cylindrical preforms exhibit higher

resistance against deformation and requires higher die load for deformation, as compared to less densified truncated conical preforms.

The variation of inertia factor *'ξ'* with die velocity for different shape-complexity factors during open-die sinter-forging of truncated conical preform is shown in figure 3.5. The inertia factor gives measure of relative magnitude of energy dissipated to overcome inertia forces, as compared to the total external energy supplied by the press die platens. It is seen from the figure that inertia factor increases exponentially with the increase in die velocity indicating that energy dissipated in the form of inertia forces is fairly significant at higher die speed of deformation, *e.g.* contribution of inertia energy dissipated towards total energy supplied by press is about 30 percent at die speed of 10 m/s. It can also be observed that inertia factor is high for low shape-complexity factor, indicating that cylindrical preforms requires more inertia energy, as compared with conical preforms for same amount of deformation. Finally, it is confirmed that the magnitude of inertia energy dissipation is comparable to other energy dissipations during sinter-forging process, especially at higher die velocities and hence, dynamic effects must be considered during analysis of mechanical processing of sintered materials.

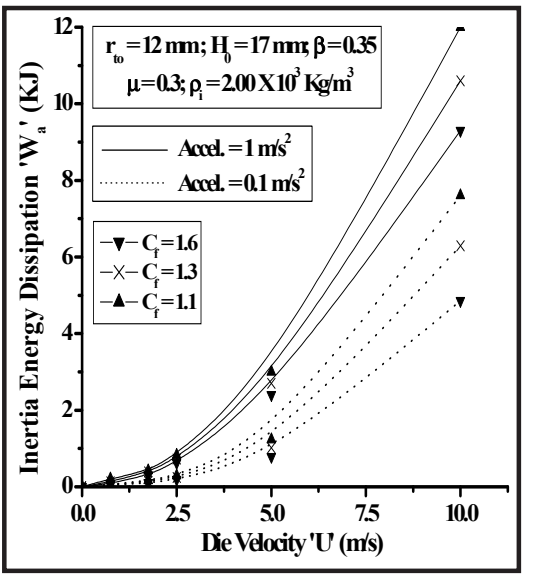

Figure 3.3: Variation of inertia energy dissipation with die velocity during open-die sinter-forging of truncated conical preform.

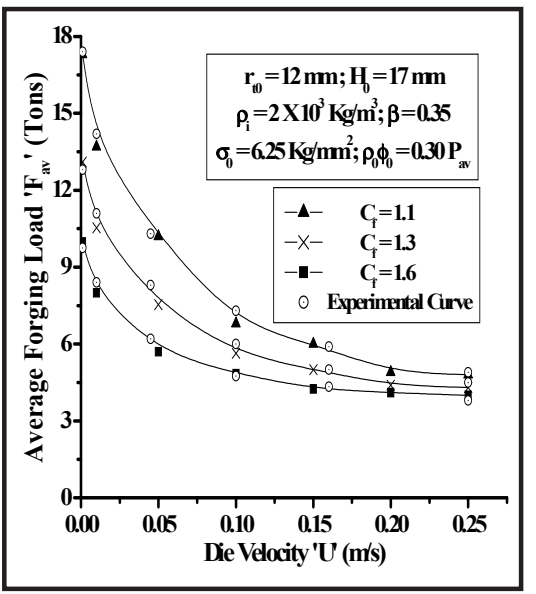

Figure 3.4: Variation of average die load with die velocity during open-die sinter-forging of truncated conical preform.

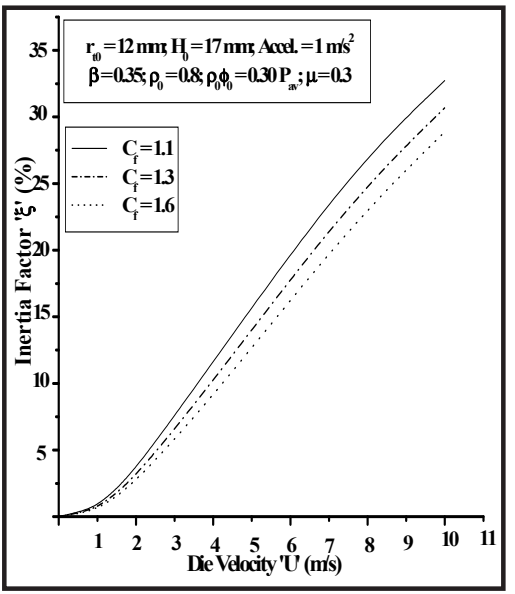

Figure 3.5: Variation of inertia factor with die velocity during open-die sinter-forging of truncated conical preform.

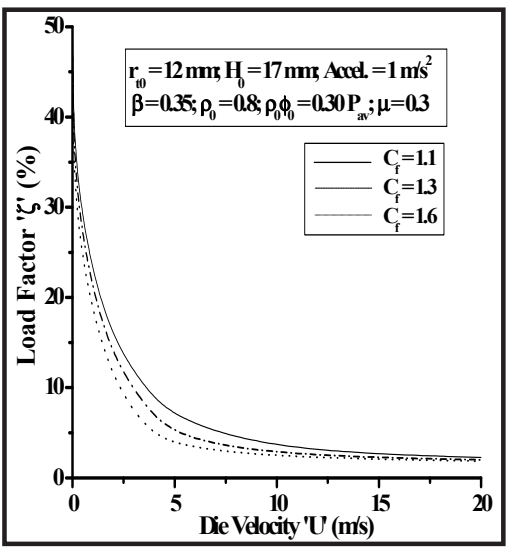

Figure 3.6: Variation of load factor with die velocity during open-die sinter-forging of truncated conical preform.

The investigation of dynamic effects on die load requirements for maximum allowable preform height reduction during open-die sinter-forging of truncated conical preform is shown in figure 3.6. The figure demonstrate variation of load factor 'ζ' with die velocity for different shape-complexity factors. It shows that load factor decreases with die velocity and becomes asymptote with x-axis, as deformation speed increases. This reveals that load required to deform the truncated conical preform at higher die velocities is considerably low as compared to deformation at slow-speeds. The amount of internal energy dissipated during mechanical processing of sintered materials at higher die velocities is entirely converted into heat and depends upon the amount and rate of plastic working, relative density and thermal properties of sintered materials. This heat generated, if not allowed to dissipate from preform-die contact surfaces immediately, will decrease the resistance of the sintered materials against deformation. This results into decrease in die-preform interfacial friction constraint appreciably, leading to lower die load requirements. The sinter-forging process, especially at high die velocities is characterized by very small deformation time, which is not sufficiently high for internal heat generated due to plastic working of sintered materials to dissipate quickly and thus, die load requirement decreases significantly.

Figures 3.7 (a) and (b) shows the variation of radial and axial strain rates with percent height reduction, shape-complexity factor, die velocity and acceleration during open-die sinter-forging of truncated conical preforms. It has been observed that the magnitude of strain rates during sinter-forging become considerably high with increase in die speed, *e.g.* axial strain rate in order of 1500 s^{-1} for 30 percent height reduction and die velocity of 3.5 m/s. It is apparent from the figures that both radial and axial strain rates increases exponentially with percent height reduction and are high for higher shape-complexity factors. Thus, truncated conical preforms will be subjected to higher strain rates, as compared to cylindrical preforms for the same die load and amount of material. The dynamic effects, *i.e.* effect of die velocity on strain rates can also be noted from the figures. It can be seen that increase in die velocity increases the axial strain rates; where as corresponding radial or lateral strain rates decreases. This is due to the densification of sintered materials during mechanical processing. The increase in relative density of the preform compensates the increase in lateral strain rates with increase in the die velocity. Finally, it is concluded that strain rate effects are dominant during mechanical processing of sintered materials, especially at high die velocities and must be taken care of during experimentation and theoretical analysis.

Figure 3.8 shows the contour graph of axial and radial strain rates with die velocity during open-die sinter-forging of truncated conical preforms. It can be easily observed that axial strain rates are higher than corresponding radial strain rates for same die velocity and other sinter-forging conditions. The contours in the graph gives the measure of axial and radial strain rates for a particular value of die velocity and depicts their interrelationship, *i.e.* measure of poison's ratio of porous material. It can be observed that poison's ratio of sintered aluminium powder preform is not constant and varies with the die velocity. Also, its value is lower than that of wrought materials, as deformation of sintered materials is accompanied with the compaction of powder particles.

The bulging of half-section (symmetry about vertical axis) of truncated conical preform during open-die sinter-forging is shown in figure 3.9. It is evident that as die travel increases, preform barrels and bulge increases. This is because the interfacial friction at die-workpiece interface retards the plastic flow of metal at preform surface and in its vicinity. The bulging or barreling phenomenon may be explained by the formation of a conical wedge of a relatively undeformed metal immediately near the preform top surface, while the rest of preform surface experiences high strains. However, ideal lubrication condition (use of lubricants) may reduce the degree of bulging to even zero level. It is also observed that bulging of truncated conical preform is concentrated at lower radius and is infinitesimally small or negligible at larger radius and for all practical purposes can be ignored. It is because; the frictional shear stress is low at smaller end of truncated conical preform due to small cross-sectional area leading to high radial flow. Thus, the bulge pattern in truncated conical preform is un-symmetrical about horizontal axis and is entirely different with comparison to cylindrical preform, where the bulge pattern is completely symmetrical.

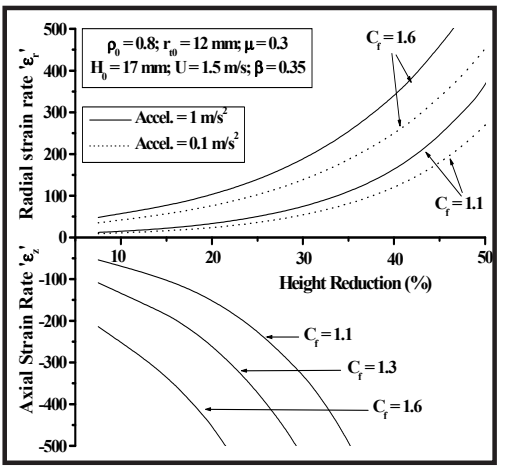

Figure 3.7 (a): Variation of radial and axial strain rates with height reduction for different shape-complexity factors during open-die sinter-forging of truncated conical preform.

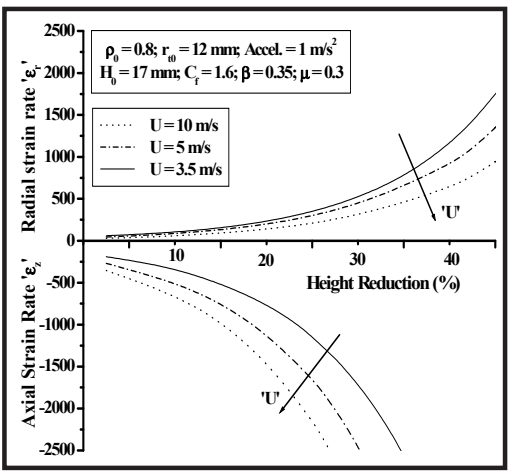

Figure 3.7 (b): Variation of radial and axial strain rate with height reduction for different die velocities during open-die sinter-forging of truncated conical preform.

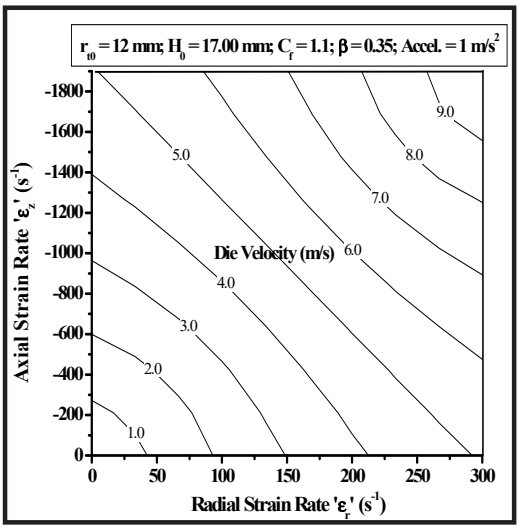

Figure 3.8: Contour plot of radial and axial strain rates for different die velocity during open-die sinter-forging of truncated conical preform.

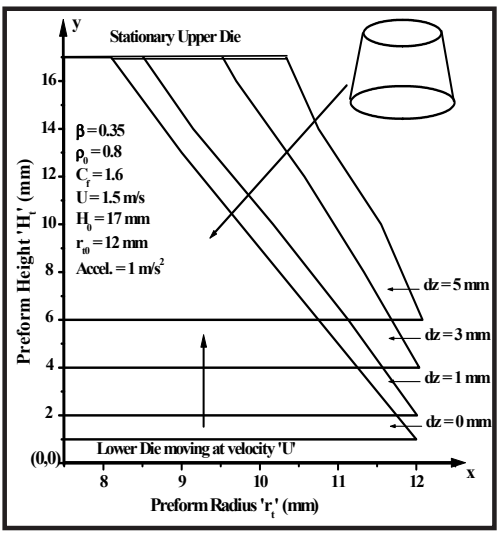

Figure 3.9: Bulged profile of truncated conical preform after open-die sinter-forging operation for different die travels.

3.2 SINTER-FORGING OF IRREGULAR POLYGONAL POWDER PREFORM

The theoretical analysis of open-die sinter-forging of irregular polygonal preform has been done with the *'Upper Bound'* approach, which is based on postulating a kinematically admissible velocity field for the entire deforming preform. However in many of the forging problems, the preform geometry precludes the formulation of a single mathematical expression for the velocity field and one such example is irregular polygonal preform. The irregular shape of polygonal preform rules out the formulation of a single velocity field throughout its body. A familiar way of dealing with such problems is the division of preform into smaller regions separated by common boundaries, so that the deformation behavior can be analyzed easily, according to the rules of *'Upper Bound'* theorem [*Sutradhar et al.,1995*].

In the present analysis also, the irregular polygonal preform has been divided into number of small regions and the velocity field for each of those regions have been formulated separately, either under axi-symmetric or plane strain conditions of deformation. The procedure of dividing the preform into smaller regions introduces the surfaces of velocity discontinuities or velocity jumps, along the boundaries. However in the present analysis, these velocity jumps along the discontinuity surfaces are avoided by suitably dividing the preform into smaller regions based on the symmetry in shape geometry and metal flow during deformation. Thus, analysis of open-die sinter-forging of irregular polygonal preform considers one additional assumption apart from the common assumptions. It states that velocity discontinuities or velocity jumps along the common boundaries of various regions assumed within the deforming irregular polygonal preform are zero.

3.2.1 Velocity Field & Strain Rates

An irregular four-sided polygonal preform *'ABCD'* has been considered for analysis as shown in figure 3.10. To simplify the *'Upper Bound'* analysis, the complete preform body has been divided into three zones, namely I, II and III, which are represented as *'$ABGO_1E$'*, *'EO_1GHO_2J'* and *'JO_2HCD'* respectively. These zones have been obtained by drawing angle bisectors from various internal corner angles of irregular polygonal preform. Then, from the intersection points of these angle bisectors, perpendiculars have been drawn to all the four sides of irregular polygon preform. Thus, both the zones I and III resulted into two pairs of symmetrical triangles, whereas zone II

resulted into a pair of symmetrical regions, which have been numbered for simplicity and given as follows:
Zone I: ΔAO_1E (1) $\cong \Delta AO_1F$ (2) and ΔBO_1F (3) $\cong \Delta BO_1G$ (4)
Zone III: ΔCO_2H (6) $\cong \Delta CO_2I$ (7) and ΔDO_2I (8) $\cong \Delta DO_2J$ (9)
Zone II: region O_1GHO_2 (5) $\cong$ region O_1EJO_2 (10)

Experimental investigations (Refer Chapter 5) and geometrical symmetry indicates that there is some kind of symmetry in material flow about the proposed perpendicular planes passing through the angle bisectors and perpendiculars drawn from the intersection of angle bisectors to the sides of irregular polygon preform. It has been found that these planes remain straight throughout the deformation process, which confirmed that there is no shear flow or velocity jumps along the boundaries of triangular regions under consideration as shown in figure 3.14. Also, the similarity in triangular regions of various zones considered under present study considerably reduces the mathematical formulations, since energy dissipations in overcoming internal strain, frictional shear resistance and inertia forces will be equal for similar triangles.

It is also seen from the figure that two circles with radius *'R_1'* and *'R_2'* with centers *'O_1'* and *'O_2'* respectively can be drawn inscribing the sides of irregular polygonal preform. Thus, deformation behavior of zones I and III can be suitable analyzed under axi-symmetry conditions and that of zone II under plane strain conditions for all practical conditions without introducing much complexity. The above method of analysis for four-sided irregular polygon can be extended to polygons with more than four sides, provided all the sides of polygons, except one are tangent to an imaginary circle [*Sagar & Juneja, 1991*].

Consider open-die sinter-forging of four-sided irregular polygonal preform at cold conditions between two perfectly flat, parallel and rigid die platens with the lower die platen moving upwards with velocity *'U'* and upper die platen being stationary as shown in figure 3.11.

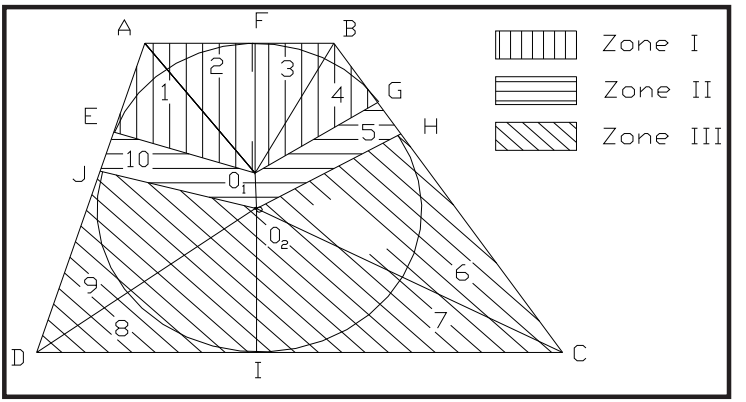

Figure 3.10: Schematic diagram of four-sided irregular polygonal preform.

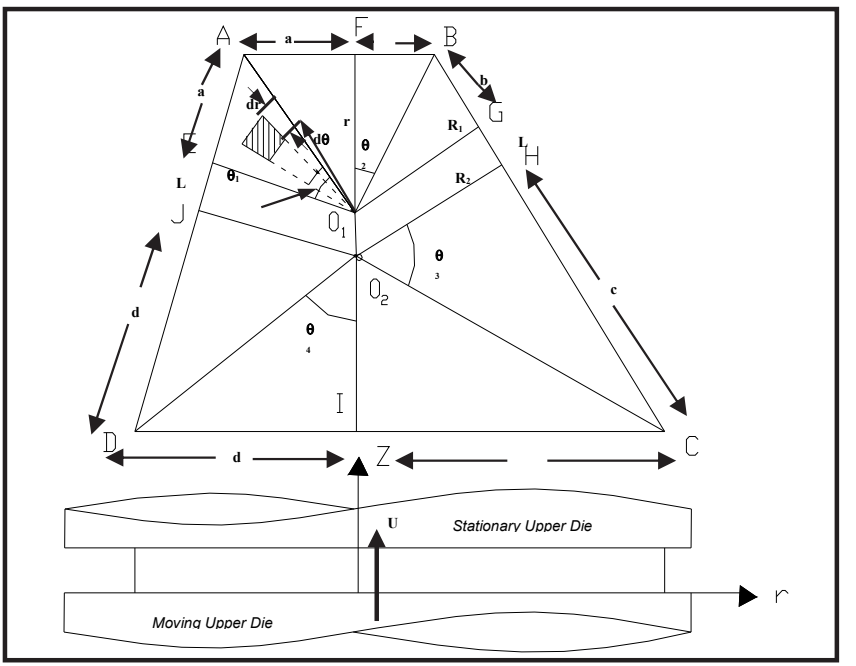

Figure 3.11: Schematic diagram of open-die sinter-forging of four-sided irregular polygonal preform.

ZONE – I & III

The deformation behavior of zones I and III can be suitable analyzed under axi-symmetry conditions as discussed earlier in the present section. The compatibility equation [Refer Equation A.9 in Appendix] and boundary conditions are given as:

$$\dot{\varepsilon}_{rr} + \dot{\varepsilon}_{\theta\theta} + \left(\frac{1-2\eta}{1+\eta}\right)\dot{\varepsilon}_{zz} = 0$$

$$U_z = U \quad \text{at} \quad z = 0 \tag{3.33}$$

$$U_z = 0 \quad \text{at} \quad z = H_0 \tag{3.34}$$

The velocity field and strain rates satisfying equations (4.23), (3.33) and (3.34) are given as [refer appendix B]:

$$U_r = \left[\frac{(1-2\eta)\beta e^{-\beta z/H_0} Ur}{2(1+\eta)\left(1-e^{-\beta}\right)H_0}\right] \tag{3.35}$$

$$U_z = -\left[\frac{\left(e^{-\beta} - e^{-\beta z/H_0}\right)U}{1-e^{-\beta}}\right] \tag{3.36}$$

$$U_\theta = 0 \tag{3.37}$$

$$\dot{\varepsilon}_{rr} = \left[\frac{(1-2\eta)\beta e^{-\beta z/H_0} U}{2(1+\eta)\left(1-e^{-\beta}\right)H_0}\right] \tag{3.38}$$

$$\dot{\varepsilon}_{zz} = -\left[\frac{\beta e^{-\beta z/H_0} U}{\left(1-e^{-\beta}\right)H_0}\right] \tag{3.39}$$

$$\dot{\varepsilon}_{\theta\theta} = \left[\frac{(1-2\eta)\beta e^{-\beta z/H_0} U}{2(1+\eta)\left(1-e^{-\beta}\right)H_0}\right] \tag{3.40}$$

$$\dot{\varepsilon}_{rz} = \frac{1}{2}\left(\frac{\partial U_r}{\partial z} + \frac{\partial U_z}{\partial r}\right)$$

$$= -\left[\frac{(1-2\eta)\beta^2 e^{-\beta z/H_0} Ur}{4(1+\eta)\left(1-e^{-\beta}\right)H_0^2}\right] \tag{3.41}$$

$$\dot{\varepsilon}_{r\theta} = \dot{\varepsilon}_{\theta z} = 0 \tag{3.42}$$

ZONE – II

The deformation behavior of zones II can be suitable analyzed under plane strain conditions as discussed earlier without introducing much complexity for all practical conditions [150]. The boundary conditions are given as equations 3.33 and 3.34 and compatibility equation [Refer Equation A.12 in Appendix] is given as:

$$\dot{\varepsilon}_{xx} + \left[\frac{(1+2\eta^2) - 2\eta\sqrt{3(1-\eta^2)}}{(1-4\eta^2)} \right] \dot{\varepsilon}_{zz} = 0 \qquad \text{(A.12)}$$

The velocity field and strain rates satisfying equations (4.24), (3.33) and (3.34) are given as [Refer Appendix C]:

$$U_x = \left[\frac{\chi\beta e^{-\beta z/H_0} Ux}{(1-e^{-\beta})H_0} \right] \qquad (3.43)$$

$$U_z = -\left[\frac{\left(e^{-\beta} - e^{-\beta z/H_0}\right) U}{\left(1-e^{-\beta}\right)} \right] \qquad (3.44)$$

$$U_y = 0 \qquad (3.45)$$

$$\dot{\varepsilon}_{xx} = \left[\frac{\chi\beta e^{-\beta z/H_0} Ux}{\left(1-e^{-\beta}\right)H_0} \right] \qquad (3.46)$$

$$\dot{\varepsilon}_{zz} = -\left[\frac{\beta e^{-\beta z/H_0} U}{\left(1-e^{-\beta}\right)H_0} \right] \qquad (3.47)$$

$$\dot{\varepsilon}_{yy} = 0 \qquad (3.48)$$

$$\dot{\varepsilon}_{xz} = \frac{1}{2}\left(\frac{\partial U_x}{\partial z} + \frac{\partial U_z}{\partial x} \right) = -\left[\frac{\chi\beta^2 e^{-\beta z/H_0} Ux}{2\left(1-e^{-\beta}\right)H_0^2} \right] \qquad (3.49)$$

$$\dot{\varepsilon}_{xy} = \dot{\varepsilon}_{yz} = 0 \qquad (3.50)$$

where, $\chi = \left[\frac{1+2\eta^2 - 2\eta\sqrt{3\left(1-\eta^2\right)}}{\left(1-4\eta^2\right)} \right]$

3.2.2 Energy Dissipations & Average Die Load

The total external energy *'J'* supplied by the die platens during plastic deformation using *'Upper Bound'* approach is given as in equation (3.11).

ZONE – I & III

The internal energy dissipation *'W_i'* for deformation of triangular region ΔAO_1E (1) is given as:

$$W_{i_1} = \left(\frac{2\sigma_o}{\sqrt{3}}\right)\int_V \left\{\sqrt{\left(\frac{1}{2}\dot{\varepsilon}_{ij}\dot{\varepsilon}_{ij}\right)}\right\} dV$$

$$= \left(\frac{2\sigma_o}{\sqrt{3}}\right)\int_{z=0}^{z=H_0}\int_{\theta=0}^{\theta=\theta_1}\int_{r=0}^{r=(R_1 \sec\theta)}\left[\sqrt{\dot{\varepsilon}_{rr}^2 + \frac{1}{2}\left(\dot{\varepsilon}_{zz}^2 + \dot{\varepsilon}_{rz}^2\right)}\right](r\,dr\,d\theta\,dz) \quad (3.51)$$

Substituting equations. (5.38) to (5.42) above, solving and simplifying, the internal energy dissipation for triangular region ΔAO_1E (1) may be expressed as:

$$W_{i_1} = \left\{\left[\frac{8\sigma_o U H_0^2 \psi^{3/2}}{3\sqrt{6}\beta^2(\psi-2)^{1/2}}\right]\left\{\left[1+\left(\frac{\beta^2 a^2 \sec^2\theta_1}{4\psi H_0^2 \tan^2\theta_1}\right)\right]^{3/2} - \tan^3\theta_1\right\}\right\} \quad (3.52)$$

The internal energy dissipation for triangular regions ΔBO_1F (3), ΔCO_2H (6) and ΔDO_2I (8) are formulated similarly and may be expressed as follows respectively:

$$W_{i_3} = \left\{\left[\frac{8\sigma_o U H_0^2 \psi^{3/2}}{3\sqrt{6}\beta^2(\psi-2)^{1/2}}\right]\left\{\left[1+\left(\frac{\beta^2 b^2 \sec^2\theta_2}{4\psi H_0^2 \tan^2\theta_2}\right)\right]^{3/2} - \tan^3\theta_2\right\}\right\} \quad (3.53)$$

$$W_{i_6} = \left\{ \left[\frac{8\sigma_o U H_0^2 \psi^{3/2}}{3\sqrt{6}\beta^2 (\psi-2)^{1/2}} \right] \left\{ \left[1 + \left(\frac{\beta^2 c^2 \sec^2\theta_3}{4\psi H_0^2 \tan^2\theta_3} \right) \right]^{3/2} - \tan^3\theta_3 \right\} \right\} \quad (3.54)$$

$$W_{i_8} = \left\{ \left[\frac{8\sigma_o U H_0^2 \psi^{3/2}}{3\sqrt{6}\beta^2 (\psi-2)^{1/2}} \right] \left\{ \left[1 + \left(\frac{\beta^2 d^2 \sec^2\theta_4}{4\psi H_0^2 \tan^2\theta_4} \right) \right]^{3/2} - \tan^3\theta_4 \right\} \right\} \quad (3.55)$$

where, $\psi = \left\{ 2 + \left[\frac{2(1+\eta)}{1-2\eta} \right]^2 \right\}$; $a = R_1 \tan\theta_1$; $b = R_1 \tan\theta_2$;

$c = R_2 \tan\theta_3$ and $d = R_2 \tan\theta_4$

The frictional shear energy dissipation *'W_f'* for triangular region ΔAO_1E (1) is given as:

$$W_{f_1} = \int_S \tau |\Delta U| dS$$

$$W_{f_1} = \int_{\theta=0}^{\theta=\theta_1} \int_{r=0}^{r=R_1\sec\theta} \left[|\tau|_{z=H_0} |U|_{z=H_0} + |\tau|_{z=0} |U|_{z=0} \right] (r dr d\theta) \quad (3.56)$$

The frictional shear stress (assuming pressure term equal to average pressure) during sinter-forging of irregular polygonal preform at z = *'0'* and *'H_0'* is given as [Refer Equation 1.7]:

$$|\tau|_{z=H_0} = \mu \left\{ P_{av} + \rho_0 \varphi_0 \left[1 - \left(\frac{r_{im} - r}{nR_1 \sec\theta} \right) \right] \right\} \quad (3.57)$$

From equation (3.35), the radial velocity at z = H_0 and z = 0 respectively are given as:

$$|U_r|_{z=H_0} = \left[\frac{(1-2\eta)\beta e^{-\beta} U r}{2(1+\eta)(1-e^{-\beta}) H_0} \right] \quad (3.58)$$

$$|U_r|_{z=0} = \left[\frac{(1-2\eta)\beta U r}{2(1+\eta)(1-e^{-\beta})} \right] \quad (3.59)$$

Substituting equations (3.57) to (3.59) into equation (3.56), solving and simplifying, frictional shear energy dissipation for triangular region ΔAO_1E (1) may be expressed as:

$$W_{f_1} = \left\{ \left[\frac{\mu(1-2\eta)\beta e^{-\beta} a^3 U}{6(1+\eta)(1-e^{-\beta})\tan^3\theta_1 H_0} \right] \left\{ \left\{ \left[P_{av} + \rho_0 \varphi_0 \left(1 + \frac{3}{4n} \right) \right] \left(\sec\theta_1 \tan\theta_1 + \ln\left| \sec\theta_1 + \tan\theta_1 \right| \right) \right\} - \left(\frac{2\rho_0 \varphi_0 r_{im} \tan^2\theta_1}{na} \right) \right\} \right\} \quad (3.60)$$

The frictional shear energy dissipation for triangular regions ΔBO_1F (3), ΔCO_2H (6) and ΔDO_2I (8) are formulated similarly and may be expressed as follows respectively:

$$W_{f_3} = \left\{ \left[\frac{\mu(1-2\eta)\beta e^{-\beta} b^3 U}{6(1+\eta)(1-e^{-\beta})\tan^3\theta_2 H_0} \right] \left\{ \left\{ \left[P_{av} + \rho_0 \varphi_0 \left(1 + \frac{3}{4n} \right) \right] \left(\sec\theta_2 \tan\theta_2 + \ln\left| \sec\theta_2 + \tan\theta_2 \right| \right) \right\} - \left(\frac{2\rho_0 \varphi_0 r_{im} \tan^2\theta_2}{nb} \right) \right\} \right\} \quad (3.61)$$

$$W_{f_6} = \left\{ \left[\frac{\mu(1-2\eta)\beta e^{-\beta} c^3 U}{6(1+\eta)(1-e^{-\beta})\tan^3\theta_3 H_0} \right] \left\{ \left\{ \left[P_{av} + \rho_0 \varphi_0 \left(1 + \frac{3}{4n} \right) \right] \left(\sec\theta_3 \tan\theta_3 + \ln\left| \sec\theta_3 + \tan\theta_3 \right| \right) \right\} - \left(\frac{2\rho_0 \varphi_0 r_{im} \tan^2\theta_3}{nc} \right) \right\} \right\} \quad (3.62)$$

$$W_{f_8} = \left\{ \left\{ \left[\frac{\mu(1-2\eta)\beta e^{-\beta} d^3 U}{6(1+\eta)(1-e^{-\beta})\tan^3\theta_4 H_0} \right] \right\} \left\{ \left\{ \left[P_{av} + \rho_0 \varphi_0 \left(1 + \frac{3}{4n}\right) \right] \right\} \left\{ \left(\sec\theta_4 \tan\theta_4 + \ln\left|\sec\theta_4 + \tan\theta_4\right| \right) \right\} \right\} \left\{ -\left(\frac{2\rho_0 \varphi_0 r_{im} \tan^2\theta_4}{nd} \right) \right\} \right\} \quad (3.63)$$

The inertia energy dissipation *'W_a'* for triangular region ΔAO_1E (1) is given as:

$$W_{a_1} = \int_V \rho_i \left(a_i U_i\right) dV = \rho_i \int_{z=0}^{z=H_0} \int_{\theta=0}^{\theta=\theta_1} \int_{r=0}^{r=(R_1 \operatorname{Sec}\theta)} \left(a_r U_r + a_z U_z\right)(r dr dz d\theta) \quad (3.64)$$

Substituting equations (3.35) and (3.36) into equations (3.21) and (3.22) and simplifying, one get:

$$\left(a_r U_r + a_z U_z\right) = \left\{ \left\{ \left[\frac{(1-2\eta)^2 \beta^3 U^3 r^2 e^{-2\beta z/H_0}}{4(1+\eta)^2 \left(1-e^{-\beta}\right)^3 H_0^3} \right] \right\} \left\{ \left[e^{-\beta} - \left[\frac{(1+4\eta) e^{-\beta z/H_0}}{2(1+\eta)} \right] \right] \right\} \left\{ -\left[\frac{U^3 \beta e^{-\beta z/H_0} \left(e^{-\beta} - e^{-\beta z/H_0}\right)^2}{\left(1-e^{-\beta}\right)^3 H_0} \right] + U\dot{U} \right\} \right\} \quad (3.65)$$

Substituting equation (3.65) into equation (3.64), solving and simplifying, the energy dissipation due to inertia forces for triangular region ΔAO_1E (1) may be expressed as:

$$W_{a_1} = \left[\frac{\rho_i H_0 a^2 U}{2\tan\theta_1} \right] \left\{ \left\{ \left[\frac{(1-2\eta)^2 \beta^2 a^2 U^2 \left(2 + \sec^2\theta_1\right)}{4(1+\eta)^3 (1+4\eta)\left(1-e^{-\beta}\right)^2 \tan^2\theta_1 H_0^3} \right] \right\} \left\{ \left[\frac{\left(e^{-\beta} + e^{-2\beta}\right)(2-\eta)}{(1+4\eta)} - 1 \right] \right\} - \frac{U^2\beta}{H_0} + \dot{U}U \right\} \quad (3.66)$$

The inertia energy dissipation for triangular regions ΔBO_1F (3), ΔCO_2H (6) and ΔDO_2I (8) are formulated similarly and may be expressed as follows respectively:

$$W_{a_3}=\left[\frac{\rho_i H_0 b^2 U}{2\tan\theta_2}\right]\left[\left\{\left[\frac{(1-2\eta)^2\beta^2 b^2 U^2\left(2+\sec^2\theta_2\right)}{4(1+\eta)^3(1+4\eta)\left(1-e^{-\beta}\right)^2\tan^2\theta_2 H_0^3}\right]\right\}\left[\frac{\left(e^{-\beta}+e^{-2\beta}\right)(2-\eta)}{(1+4\eta)}-1\right]-\frac{U^2\beta}{H_0}+\dot{U}U\right] \quad (3.67)$$

$$W_{a_6}=\left[\frac{\rho_i H_0 c^2 U}{2\tan\theta_3}\right]\left[\left\{\left[\frac{(1-2\eta)^2\beta^2 c^2 U^2\left(2+\sec^2\theta_3\right)}{4(1+\eta)^3(1+4\eta)\left(1-e^{-\beta}\right)^2\tan^2\theta_3 H_0^3}\right]\right\}\left[\frac{\left(e^{-\beta}+e^{-2\beta}\right)(2-\eta)}{(1+4\eta)}-1\right]-\frac{U^2\beta}{H_0}+\dot{U}U\right] \quad (3.68)$$

$$W_{a_8}=\left[\frac{\rho_i H_0 d^2 U}{2\tan\theta_4}\right]\left[\left\{\left[\frac{(1-2\eta)^2\beta^2 d^2 U^2\left(2+\sec^2\theta_4\right)}{4(1+\eta)^3(1+4\eta)\left(1-e^{-\beta}\right)^2\tan^2\theta_4 H_0^3}\right]\right\}\left[\frac{\left(e^{-\beta}+e^{-2\beta}\right)(2-\eta)}{(1+4\eta)}-1\right]-\frac{U^2\beta}{H_0}+\dot{U}U\right] \quad (3.69)$$

ZONE – II

The internal energy dissipation *'W_i'* for region O_1O_2HG (5) is given as:

$$W_{i_5}=\left(\frac{2\sigma_o}{\sqrt{3}}\right)\int_V\left[\sqrt{\left(\frac{1}{2}\dot{\varepsilon}_{ij}\dot{\varepsilon}_{ij}\right)}\right]dV$$

$$=\left(\frac{2\sigma_o}{\sqrt{3}}\right)\int_{x=0}^{x=R'_{i0}}\int_{y=0}^{y=L}\int_{z=0}^{z=H_0}\left(\dot{\varepsilon}_{xx}^2+\dot{\varepsilon}_{yy}^2+\dot{\varepsilon}_{zz}^2\right)^{1/2}(dxdydz) \quad (3.70)$$

Substituting equations (3.46) to (3.50) above, solving and simplifying, the internal energy dissipation for region O_1O_2HG (5) may be expressed as:

$$W_{i_5}=\left[\frac{2\sigma_o U(1+\chi^2)}{\sqrt{3}\chi\beta}\right]\left\{\begin{array}{l}\left(\frac{\chi\beta R'_{i0}}{2H_0\sqrt{1+\chi^2}}\right)+\sqrt{1+\left(\frac{\chi\beta R'_{i0}}{2H_0\sqrt{1+\chi^2}}\right)^2}\\ +\ln\left[\left(\frac{\chi\beta R'_{i0}}{2H_0\sqrt{1+\chi^2}}\right)+\sqrt{1+\left(\frac{\chi\beta R'_{i0}}{2H_0\sqrt{1+\chi^2}}\right)}\right]\end{array}\right\} \quad (3.71)$$

where,

$$R'_{i0}=\left(\frac{R_1+R_2}{2}\right)$$

The frictional shear energy dissipation *'W_f'* for region O_1O_2HG (5) is given as:

$$W_{f_5} = \int_S \tau |\Delta U| dS$$
$$= \int_{x=0}^{x=R_0} \int_{y=0}^{y=L} \left[|\tau|_{z=H_0} |U|_{z=H_0} + |\tau|_{z=0} |U|_{z=0} \right] (xdxdy) \quad (3.72)$$

The frictional shear stress for plane strain condition during sinter-forging of irregular polygonal preform (assuming pressure term equal to average pressure) at z = *'0'* and *'H_0'* is given as [Refer Equation 1.8]:

$$\tau = \mu \left\{ P_{av} + \rho_0 \varphi_0 \left[1 - \left(\frac{x_{im} - x}{nL} \right) \right] \right\} \quad (3.73)$$

From equation (5.43), the axial velocity at z = *'H_0'* and z = *'0'* respectively are given as

$$|U_x|_{z=H_0} = \left[\frac{\chi \beta e^{-\beta} Ux}{(1 - e^{-\beta}) H_0} \right] \quad (3.74)$$

$$|U_x|_{z=0} = \left[\frac{\chi \beta Ux}{(1 - e^{-\beta}) H_0} \right] \quad (3.75)$$

Substituting equations (3.73) to (3.75) into equation (3.72), solving and simplifying, the frictional shear energy dissipation for region O_1O_2HG (5) may be expressed as:

$$W_{f_5} = \left[\frac{\mu \chi \beta e^{-\beta} U R_0^2}{H_0 \left(1 - e^{-\beta}\right)} \right] \left\{ P_{av} + \rho_0 \varphi_0 \left[1 - \left(\frac{3x_{im} - 2R_0}{3nL} \right) \right] \right\} \quad (3.76)$$

The inertia energy dissipation *'W_a'* for region O_1O_2HG (5) may be given as:

$$W_{a_5} = \int_V \rho_i (a_i U_i) dV = \rho_i \int_{x=0}^{x=R_0} \int_{y=0}^{y=L} \int_{z=0}^{z=H_0} (a_x U_x + a_z U_z)(dxdydz) \quad (3.77)$$

where:

$$a_x = \left[U_x \frac{\partial U_x}{\partial x} + U_z \frac{\partial U_x}{\partial z} + \frac{\partial U_x}{\partial t} \right] \quad (3.78)$$

$$a_z = \left[U_z \frac{\partial U_z}{\partial z} + \frac{\partial U_z}{\partial t} \right] \quad (3.79)$$

Substituting equations (3.43) and (3.44) into equations (3.78) and (3.79) and simplifying, one get:

$$\left(a_x U_x + a_z U_z\right) = \left\{ \begin{array}{l} \left[\dfrac{\beta^3 U^3 x^2 \chi^2 e^{-2\beta z/H_0}}{\left(1-e^{-\beta}\right)^3 H_0^3} \right] \left[e^{-\beta} - (1+\chi) e^{-\beta z/H_0} \right] \\ - \left[\dfrac{\beta U^3 e^{-\beta z/H_0} \left(e^{-\beta} - e^{-\beta z/H_0} \right)}{\left(1-e^{-\beta}\right)^3 H_0} \right] + U\dot{U} \end{array} \right\} \qquad (3.80)$$

Substituting equation (3.80) into equation (3.77), solving and simplifying, the energy dissipation due to inertia forces for region O_1O_2HG (5) may be expressed as:

$$W_{a_5} = 2\rho_i L R_0 \left\{ \begin{array}{l} \left(\dfrac{U}{1-e^{-\beta}} \right)^3 \left\{ \begin{array}{l} \left[\dfrac{2\chi^2\beta^2 R_0^2 e^{-\beta}\left(1-e^{-\beta}\right)}{9H_0^2(5+2\chi)} \right] \left[\left(\dfrac{1+\chi}{5+2\chi} \right) + \left(\dfrac{1+e^{-\beta}}{2} \right) \right] \\ + \left(\dfrac{1-e^{-\beta}}{2} \right)^2 \end{array} \right\} \\ + U\dot{U} \end{array} \right\} \qquad (3.81)$$

The energy dissipations for similar regions resulted due to division of irregular preform are supposed to be same. These similar regions are: ΔAO_1E (1) $\cong$ ΔAO_1F (2); ΔBO_1F (3) $\cong$ ΔBO_1G (4); ΔCO_2H (6) $\cong$ ΔCO_2I (7), ΔDO_2I (8) $\cong$ ΔDO_2J (9) and region O_1O_2HG (5) $\cong$ region O_1O_2JE (10). Thus, energy dissipations for regions 2 (ΔAO_1F), 4 (ΔBO_1G), 7 (ΔCO_2I), 9 (ΔDO_2J) and 10 (region O_1O_2JE) may be estimated by equating to those of regions 1 (ΔAO_1E), 3 (ΔBO_1F), 6 (ΔCO_2H), 8 (DO_2I) and 5 (region O_1O_2HG) respectively, which has already been computed. Thus, total energy dissipation during open-die sinter-forging of irregular polygonal preform may be obtained by summing all the individual energy dissipations and may be expressed as:

$$J = 2 \sum_{q=1,3,6,8,5} \left(W_{i_q} + W_{f_q} + W_{a_q} \right) \qquad (3.82)$$

Thus, the average forging load may be estimated by substituting equation (3.82) into equation (3.27). The shape-complexity factor *'C_q'* has been introduced in the present research work to investigate the effect of shape variations of irregular polygonal preform on various characteristics of sinter-forging, which has been expressed as the ratio of radii of imaginary circles considered during division of irregular polygonal preform into various zones. The factor tends to unity, when $R_1 \cong R_2$ *i.e.* shape of irregular polygonal preform approaches to that of a square and tends to zero, when $R_1 \cong 0$ *i.e.* shape of irregular polygonal preform approaches to that of a triangle. Mathematically, it is expressed as:

$$C_q = \left(\frac{R_1}{R_2} \right) \qquad (3.83)$$

The dynamic or inertia effects, *i.e.* effect of die velocity on relative magnitudes of various energy dissipations and average die load involved during open-die sinter-forging of truncated conical preform has been illustrated using concepts of inertia factor *'ξ'* (Refer Equation 3.28) and load factor '*ζ*' (Refer Equation 3.29) as discussed in the previous section.

3.2.3 Results & Parametric Discussion

A typical data of preform and deformation characteristics compatible with corresponding experimental work has been considered to illustrate the dynamic effects on the magnitude of various energies, die load and strains rates involved during open-die sinter-forging of irregular polygonal preform and is given as follows:
H_0 = 10 mm; β = 0.30; $\rho_0\phi_0$ = 0.30 P_{av}; n = 3; ρ_i = 2 x 10^3 kg/m^3; σ_0 = 6.25 kg/mm^2; μ = 0.30 (high interfacial friction) and 0.01 (low interfacial friction); U = 0.001 to 10 m/sec.

The value of r_{im} and x_{im} used during calculation is varied according to interfacial lubrication conditions. The dimensions of preform for shape-complexity factors C_q = 0.85, 0.60 and 0.30 respectively are shown in table 3.3. Figure 3.12 shows variation of inertia energy dissipation with the die velocity for different shape-complexity factor at high interfacial friction condition during open-die sinter-forging of irregular polygonal preform. It is clearly evident from the figure that inertia energy dissipation increases exponentially with increase in the die velocity and becomes asymptote to y-axis at higher die velocities. This indicates that inertia energy dissipation is considerably high during deformation at higher die speeds and cannot be neglected during *'Upper Bound'* analysis. The higher curves for low shape-complexity factor indicates that as the shape of irregular polygonal preform approaches towards that of an enclosing square, corresponding inertia energy requirement also increases. The increase in shape-complexity factor means that the radii of imaginary circles on preform surface are numerically getting closer to each other and its shape is approaching towards that of an enclosing square (Refer Figure 3.10).

The experimental and theoretical variation of die loads with die velocity and shape-complexity factor for high interfacial friction conditions for maximum height reductions during sinter-forging of irregular polygonal preform is shown in figure 3.13. It is apparent that

die load decreases rapidly with increase in die velocity and becomes asymptote with x-axis at higher die speeds. The small contact time between die and preform at higher die velocities creates the conditions essential for load reduction. It can also be observed that densified square preform requires higher load to deform, as compared to irregular polygonal preform, which in turn will deform at higher load, as compared to triangular preform for the same amount of deformation.

The investigations into dynamic effects, *i.e.* die velocity on energy dissipation is shown in the form of variation of inertia factor *'ξ'* in figure 5.14. It is clearly evident that inertia factor increases exponentially with die velocity and at higher die velocity, the magnitude of inertia energy dissipation, as percent fraction of total external energy is substantially high, *e.g.* 10 percent at die velocity of 6 m/s.

Figure 3.15 demonstrate the variation of load factor 'ζ' for maximum allowable height reduction with die velocity during open-die sinter-forging of irregular polygonal preform. It is revealed from the figure that load factor decreases with die velocity and becomes asymptote with x-axis at higher die velocities. Thus, dynamic effects, *i.e.* die velocity leads to lower load requirements during sinter-forging operation, especially at higher die speeds, as compared to slow-speed deformation. The small deformation time during mechanical processing of sintered preforms at higher die velocities does not allow the heat generated during plastic working to dissipate quickly from preform-die interface, leading to low resistance of sintered materials against deformation and die-preform surface interfacial friction constraint.

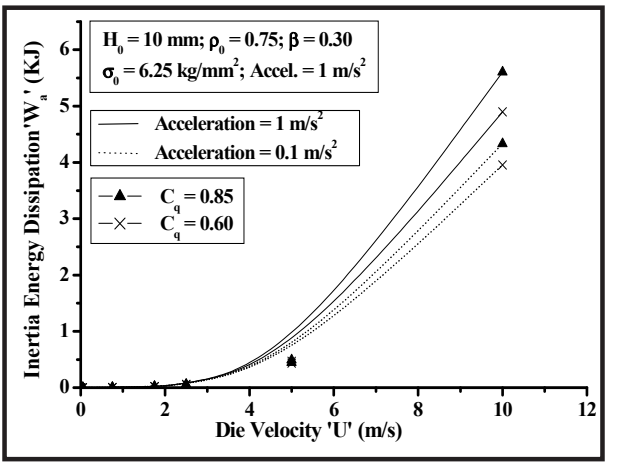

Figure 3.12: Variation of inertia energy dissipation with die velocity during open-die sinter-forging of irregular polygonal preform.

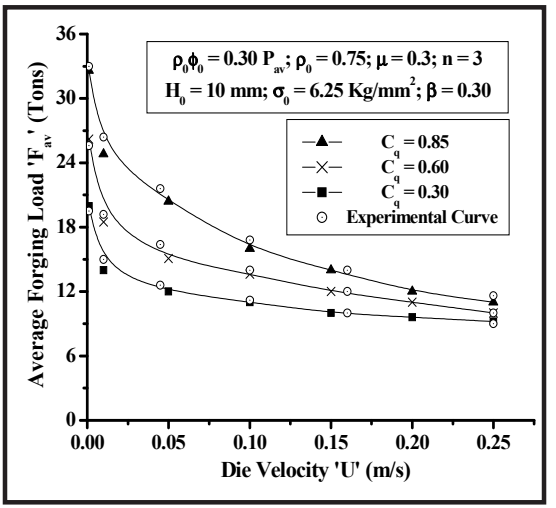

Figure 3.13: Variation of average die load with die velocity during open-die sinter-forging of irregular polygonal preform.

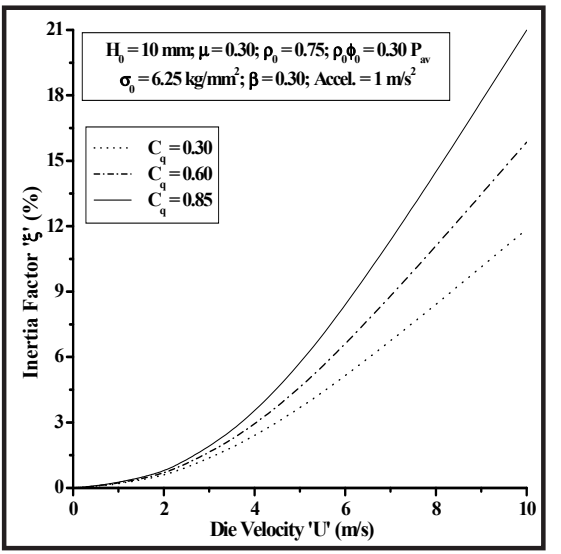

Figure 3.14: Variation of inertia factor with die velocity during open-die sinter-forging of irregular polygonal preform.

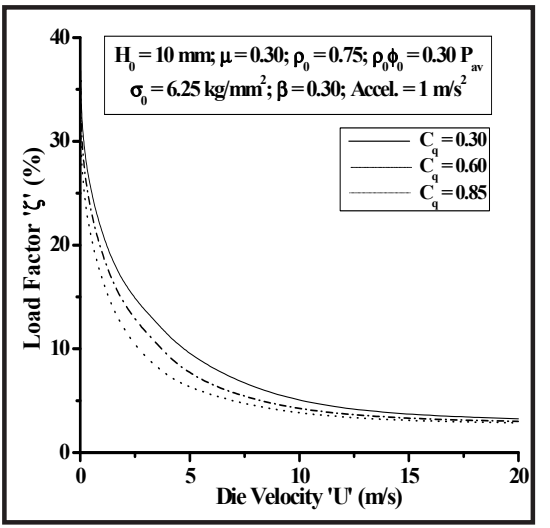

Figure 3.15: Variation of load factor with die velocity during open-die sinter-forging of irregular polygonal preform.

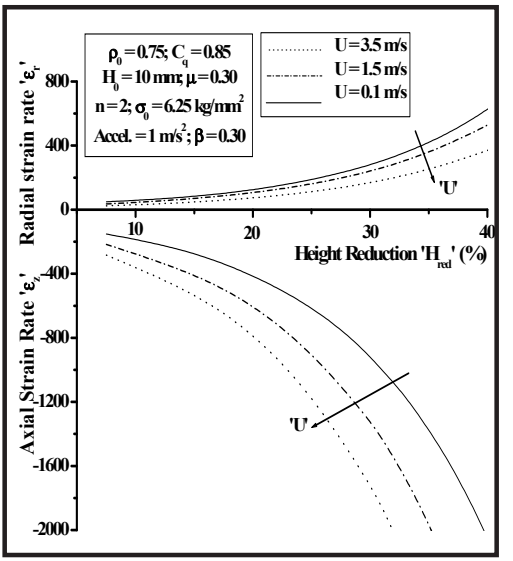

Figure 3.16: Variation of radial and axial strain rates with die velocity during open-die sinter-forging of irregular polygonal preform.

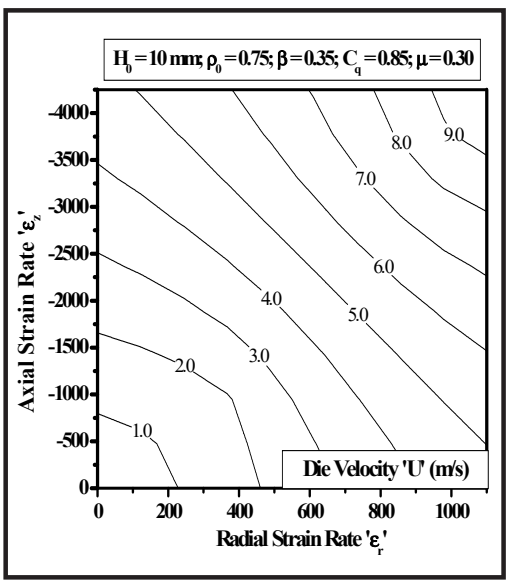

Figure 3.17: Contour plot of radial and axial strain rates for different die velocity during open-die sinter-forging of irregular polygonal preform.

Figure 3.16 shows the variation of radial and axial strain rates with percent height reduction, shape-complexity factor and die velocity during open-die sinter-forging of irregular polygonal preforms. It can be seen that both radial and axial strain rates increases exponentially with percent height reduction of preform. It is also evident that increase in the die velocity increases the axial strain rates but decreases the corresponding radial or lateral strain rates. This may be explained from the compatibility viewpoint. It has already been established in the present research work that volume changes are observed during sinter-forging operations due to densification of preforms. Thus, decrease in lateral strain rate is due to simultaneous increase in relative density and axial strain rate of preforms. The contour graph for axial and radial strain rates has also been plotted as shown in figure 5.17, which gives the measures of poison's ratio of sintered porous materials. It can be easily seen that poison's ratio of sintered materials varies with die velocity and other sinter-forging characteristics and its magnitude is less than that of wrought materials.

Figure 3.18 shows the average die pressure distribution over the surface of irregular polygonal preform during open-die sinter-forging. It is apparent from the figure that average die pressure increases exponentially from the periphery to the center of preform surface and is highest at the central axis. At the periphery of preform, average die pressure is equal to atmospheric pressure and at the center; it is asymptote to vertical axis. The high interfacial pressure at the center of irregular polygonal preform is due to high interfacial sticking friction phenomenon. The pressure distributions are also high for high shape-complexity factor indicating that square preforms will be subjected to higher die loads, as compared to the triangular or irregular polygonal preforms for the same amount of material.

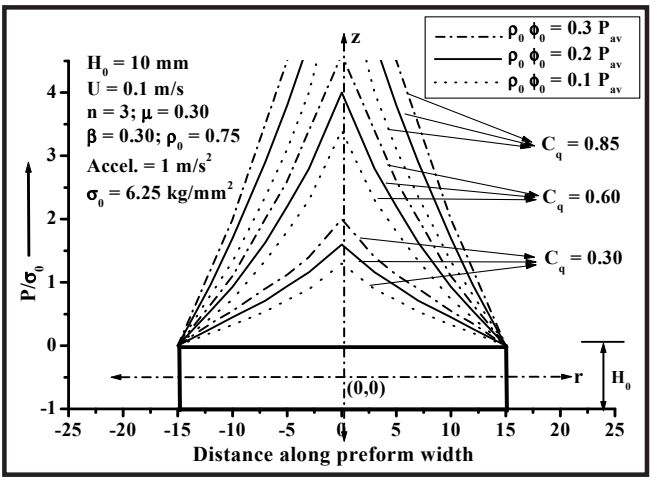

Figure 3.18: Pressure distribution over irregular polygonal preform surface during open-die sinter-forging.

CHAPTER - 4
CLOSE DIE FORGING OF SINTERED PREFORMS

Outline of the Chapter: *4.1 Flashless Closed-Die Sinter-Forging: Deformation Mode-I; 4.1.1 Velocity Field & Strain Rates; 4.1.2 Energy Dissipations & Average Die Load; 4.2 Flashless Closed-Die Sinter-Forging: Deformation Mode –II; 4.2.1 Velocity Field & Strain Rates; 4.2.2 Energy Dissipations & Average Die Load; 4.3 Results & Parametric Discussion*

The present chapter considers closed-die sinter-forging of a cylindrical preform to a double-hub-flange component at cold conditions. Figure 4.1 shows the schematic diagram of flashless closed-die sinter-forging of a double-hub flange component, where a cylindrical preform is initially placed in between two rigid die-halves of closed-die set comprising of upper punch, counter lower punch and container. Deformation takes place, as the upper punch moves downwards within the cylindrical cavity with velocity *'U'*, whereas the lower counter punch is static. The dies have cylindrical recess-cavities with depth equal to length of hubs required on both sides of the component and diameter equal to the diameter of hubs. These cavities also minimize the difficulty and variability during billet location within the closed-dies [*Ibhadode & Dean, 1988*].

The complete deformation process has been considered in two subsequent stages as shown in figure 4.2. The first stage consists of barreling of free vertical surface of cylindrical preform, as in case of conventional open-die sinter-forging, till it reaches and touches the middle of container sidewalls. This should happen without the occurrence of fracture on the preform bulged surface for defect-free sinter-forged products, which may be achieved by proper selection of preform aspect ratio, *e.g.* aspect ratio of 0.35-0.55 is recommended during closed-die sinter-forging of aluminum metal powder cylindrical preform without the occurrence of cracks.

During this stage of deformation, contact with container wall is around the mid height of workpiece and corner regions of die cavity remains unfilled. The subsequent second stage consists of constrained deformation of bulged preform, where corners are formed and filled. In

this stage, the bulged profile of preform is approximated with straight lines as shown with the dotted lines in the figure [*Manisekar & Narayanasamy, 2003; Ibhadode & Dean, 1987*].

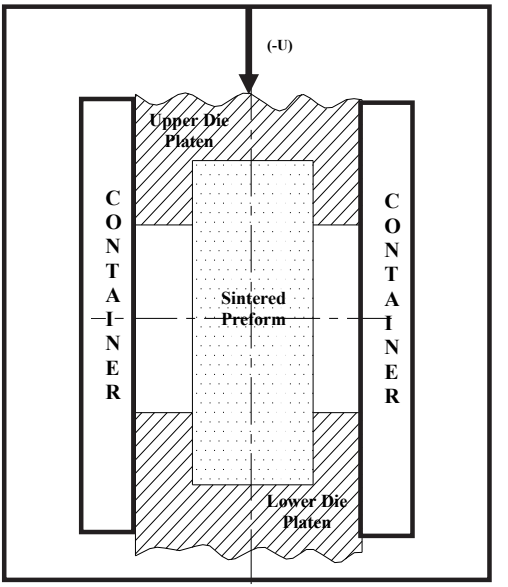

Figure 4.1: Schematic diagram of flashless closed-die sinter-forging of cylindrical preform.

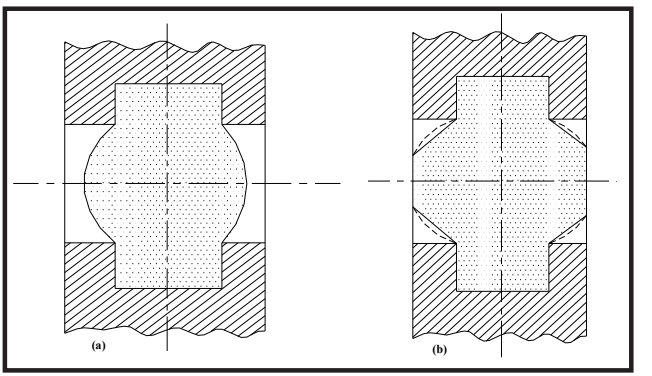

Figure 4.2: Deformation stages during flashless closed-die sinter-forging of cylindrical preform into double-hub flange component.

During *'Upper Bound'* analysis, the centers of co-ordinate axes are chosen at the center of preform and deformation of only quarter portion of preform has been considered due to symmetry about horizontal and vertical axes. The die load is computed at the end of closed-die sinter-forging operation, *i.e.* when the die cavity is just about to be filled completely and a small corner filling is still left. Also, two separate cases of deformation modes have been considered based on the different division of preform into dead and deforming zones.

The present research work considers some additional assumptions, which are as follows [*Ibhadode & Dean, 1988*]:

a. A very small corner of die cavity remains unfilled at the end of operation and the height of strip corresponding to this unfilled region is *'h'*. The estimation of various energies and die load is made at the end of operation, *i.e.* when the die is about to be filled completely and load is maximum.

b. Barreling of preform during second phase of deformation is neglected and it is assumed that inclined surface of deforming preform remains inclined during die cavity corner filling.

c. The circumferential flow of preform *i.e.* rotation of specimen has been neglected.

d. The deformation of cylindrical preform into of double hub-flange component is considered under axi-symmetric condition and corresponding compatibility condition is expressed as follows (Refer Equation A.9):

$$\dot{\varepsilon}_{rr} + \dot{\varepsilon}_{\theta\theta} + \left(\frac{1-2\eta}{1+\eta}\right)\dot{\varepsilon}_{zz} = 0 \qquad (4.1)$$

4.1 FLASHLESS CLOSED-DIE SINTER-FORGING: DEFORMATION MODE-I

In case of deformation mode-I, the quarter portion of deforming preform has been divided into three zones, namely zones 1, 2 and 3 respectively as shown in figure 4.3. It is assumed that there is no metal flow in zones 1 and 3 and hence, these zones are assumed to be dead. Thus, there is metal flow in zone 2 only and material corresponding to this zone is under the state of deformation. The boundary conditions for zone 2 are given as:

$U_z = 0$ at $z = 0$ (4.2)

$U_z = -U$ at $z = H'_0$ (4.3)

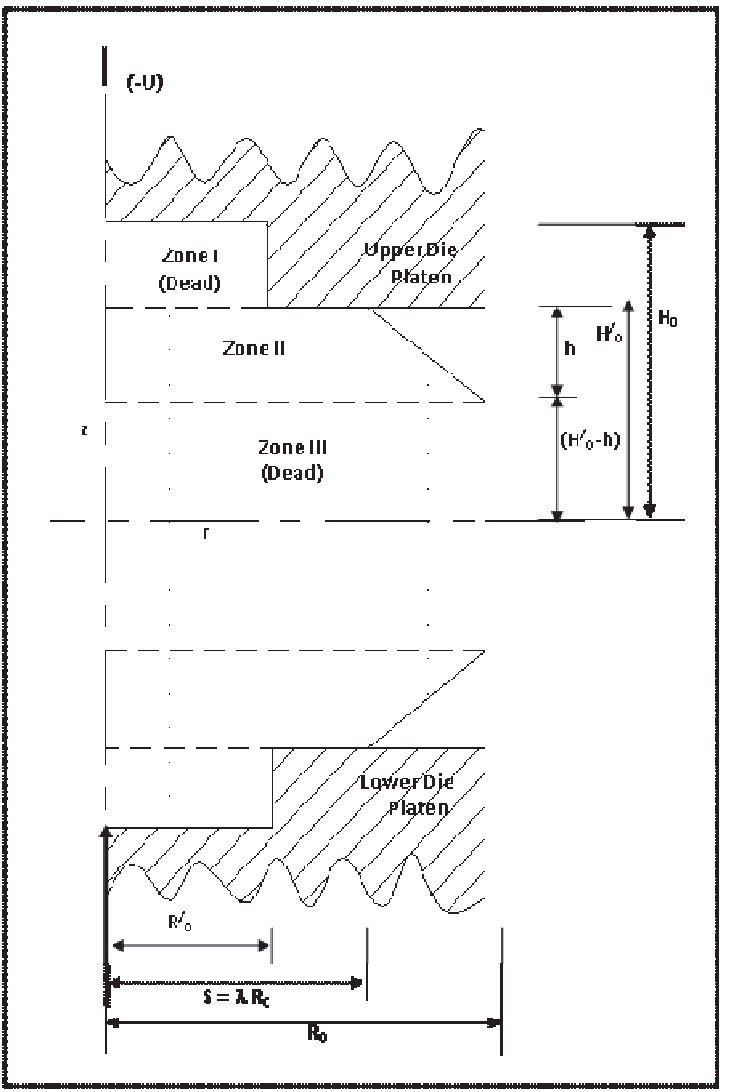

Figure 4.3: Schematic diagram of flashless closed-die sinter-forging of double-hub flange component during deformation mode-I.

4.1.1 Velocity Field & Strain Rates

The velocity field and strain rates satisfying equations (A.9), (4.2) and (4.3) are given as (Refer Appendix D):

$$U_r = \left[\frac{(1-2\eta)\,Ur}{2(1+\eta)\,h} \right] \qquad (4.4)$$

$$U_z = -\left(\frac{Uz}{h}\right) \tag{4.5}$$

$$U_\theta = 0 \tag{4.6}$$

$$\dot{\varepsilon}_{rr} = \left[\frac{(1-2\eta)U}{2(1+\eta)h}\right] \tag{4.7}$$

$$\dot{\varepsilon}_{zz} = -\left(\frac{U}{h}\right) \tag{4.8}$$

$$\dot{\varepsilon}_{\theta\theta} = \left[\frac{(1-2\eta)U}{2(1+\eta)h}\right] \tag{4.9}$$

$$\dot{\varepsilon}_{r\theta} = \dot{\varepsilon}_{\theta z} = \dot{\varepsilon}_{rz} = 0 \tag{4.10}$$

4.1.2 Energy Dissipations & Average Die Load

The total external energy *'J'* supplied by the die platens during plastic deformation using *'Upper Bound'* approach is given as in equation (3.11). The internal energy dissipation *'W_i'* is given as:

$$W_i = \left(\frac{2\sigma_0}{\sqrt{3}}\right)\int_V \sqrt{\frac{\varepsilon_{ij}\varepsilon_{ij}}{2}}\,dV$$

$$= \left(\frac{2\sigma_0}{\sqrt{3}}\right)\int_{r=S}^{R_0}\int_{z=0}^{z=z_0}\left(\dot{\varepsilon}_{rr}^2 + \frac{\dot{\varepsilon}_{zz}^2}{2}\right)^{\frac{1}{2}}(2\pi r.drdz) \tag{4.11}$$

where:

$$z_0 = h\left[1-\left(\frac{r-S}{R_0-S}\right)\right]$$

Substituting equations (4.4) to (4.10) above, solving and simplifying, the internal energy dissipation may be expressed as:

$$W_i = \left[\frac{\sqrt{2}\pi\sigma_0 U R_0^2 (2\lambda+1)\psi^{1/2}}{3\sqrt{3}(\psi-2)^{1/2}}\right] \tag{4.12}$$

where:

$$\lambda = \left(\frac{S}{R_0}\right) \text{ and } \psi = \left\{2+\left[\frac{2(1+\eta)}{1-2\eta}\right]^2\right\}$$

The energy will be dissipated to overcome interfacial friction at die-workpiece and container-workpiece interfaces as preform surface is in contact with upper die punch as well as with die container. The

frictional shear energy dissipation at die-workpiece interface 'W_{f_1}' is given as:

$$W_{f_1} = \int_S \tau |\Delta U| dS = \mu \int_{r=R_0'}^{r=R_0} \tau_1 |U_r|_{z=H_0'} (2\pi r dr) \tag{4.13}$$

The frictional shear stress (assuming pressure equal to average pressure) at die-preform interface during closed-die sinter-forging is given as [Refer Equation 1.9]:

$$\tau_1 = \mu \left\{ P_{av} + \rho_0 \varphi_0 \left[1 - \left(\frac{r_{cm} - r}{nS} \right) \right] \right\} \tag{4.14}$$

From equation (3.7), the radial velocity at z = *'H_0'* is given as:

$$|U_r|_{z=H_0'} = \left[\frac{(1-2\eta) U r}{2(1+\eta) h} \right] \tag{4.15}$$

Substituting equations (3.14) and (3.15) into equation (3.13), solving and simplifying, the frictional shear energy dissipation at die-workpiece interface may be expressed as:

$$W_{f_1} = \left\{ \begin{array}{l} \left[\dfrac{\pi\mu(1-2\eta) U \left(\lambda^3 R_0^{\ 3} - R_0'^3 \right)}{3(1+\eta) h} \right] \\ x \left[P_{av} + \rho_0 \varphi_0 \left(1 - \dfrac{r_{cm}}{nR_0\lambda} \right) + \left(\dfrac{3\rho_0\varphi_0}{4\lambda n R_0} \right) \left(\dfrac{\lambda^4 R_0^{\ 4} - R_0'^4}{\lambda^3 R_0^{\ 3} - R_0'^3} \right) \right] \end{array} \right\} \tag{4.16}$$

The frictional shear energy dissipation at container-workpiece interface 'W_{f_2}' is given as:

$$W_{f_2} = \int_S \tau |\Delta U| dS = \mu \int_{z=0}^{H_0' - h} \tau_2 |U_z|_{r=R_0} (2\pi R_0 dz) \tag{4.17}$$

The present analysis considers equalization of average pressure during constraint deformation of axi-symmetric cylindrical preform keeping the container reaction pressure distribution reasonably accurate. Therefore, the average pressure at die-preform interface is considered to be same as that of container-preform interface. Thus, the frictional shear stress (assuming pressure term equal to average pressure) at container-preform interface during closed-die sinter-forging is given as [Refer Equation 1.10]:

$$\tau_2 = \mu \left\{ P_{av} + \rho_0 \varphi_0 \left[1 - \left(\frac{z_{cm} - z}{nH_0'} \right) \right] \right\} \tag{4.18}$$

From equation (4.5), the axial velocity at r = *'R_0'* is given as:

$$U_z = -\left(\frac{Uz}{h}\right) \tag{4.19}$$

Substituting equations (4.18) and (4.19) into equation (4.17), solving and simplifying, the frictional shear energy dissipation at container-workpiece interface may be expressed as:

$$W_{f_2} = \left\{\begin{array}{l}\left(\dfrac{\pi\mu R_0 (H_0' - h)^2 U}{h}\right) \\ \left\{P_{av} + \rho_0\varphi_0\left(1 - \dfrac{z_{cm}}{nH_0'}\right) + \left[\dfrac{2\rho_0\varphi_0(H_0' - h)^3}{3nH_0'(H_0' - h)^2}\right]\right\}\end{array}\right\} \tag{4.20}$$

The energy dissipation due to inertia forces 'W_a' *is given as:*

$$W_a = \int_V \rho_i \left(a_r U_r + a_z U_z\right) dV$$

$$= \rho_i \int_{r=s}^{r=R_0} \int_{z=0}^{z=z_0} \left(a_r U_r + a_z U_z\right)\left(2\pi r.drdz\right) \tag{4.21}$$

Substituting equations (4.4) and (4.5) into equations (3.21) and (3.22) and simplifying, one get:

$$\left(a_r U_r + a_z U_z\right) = \left\{\left[\frac{1-2\eta}{2(1+\eta)}\right]^3 r^2 - z^2\right\}\left(\frac{U}{h}\right)^3 + \dot{U} \tag{4.22}$$

Substituting equation (4.22) into equation (4.21), solving and simplifying, the energy dissipation due to inertia forces may be expressed as:

$$W_a = \left(\frac{\pi\rho_i (1-\lambda) R_0^2 U}{10}\right)\left\{\begin{array}{l}\left[\dfrac{R_0^2\left(4\lambda^3 + 3\lambda^2 + 2\lambda + 1\right)U^2}{(\psi - 2)^{3/2} h^2}\right] \\ + \left[\dfrac{(1+4\lambda)U^2}{3}\right] + \left[\dfrac{20h(2\lambda+1)\dot{U}}{1-\lambda}\right]\end{array}\right\} \tag{4.23}$$

Thus, the total energy dissipations is given as:

$$J = 4\sum_j \left(W_i + W_{f_1} + W_{f_2} + W_a\right)_j \quad \textit{(j = No. of zones)} \tag{4.24}$$

Thus, average forging load may be computed by substituting equations (4.24) into equation (3.27).

4.2 FLASHLESS CLOSED-DIE SINTER-FORGING: DEFORMATION MODE -II

In case of deformation mode-I, the quarter portion of deforming preform has been divided into four zones, namely zones 1, 2, 3 and 4 respectively as shown in figure 4.4. It is assumed that there is no metal flow in zone 1 and hence, the zone is assumed to be dead. Thus, there is metal flow in zone 2, 3 and 4 and materials corresponding to these zones are under the state of deformation. The *'Upper Bound'* analyses for these zones are dealt separately and finally all the energy dissipations are summed at the end to compute average die load.

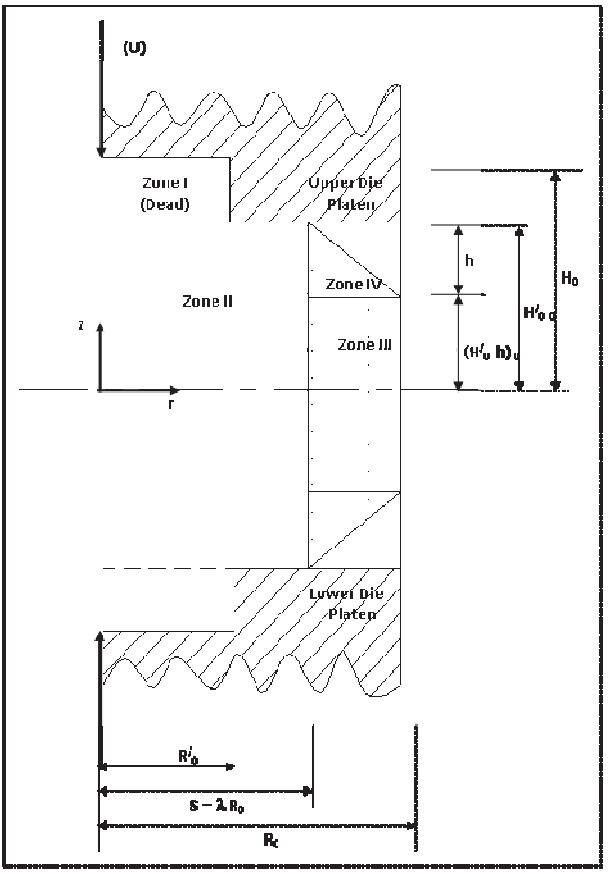

Figure 4.4: Schematic diagram of flashless closed-die sinter-forging of double-hub flange component during deformation mode-II.

The boundary conditions for zones 2, 3 and 4 during closed-die sinter-forging of double hub-flange component are given as:

$U_z = -U$	at	$z = H'_0$	(zone 2)	(4.25)
$U_z = 0$	at	$z = 0$	(zone 2 and 3)	(4.26)
$U_z = -U\,[(H'_0 - h) / H'_0]$	at	$z = (H'_0 - h)$	(zone 3 and 4)	(4.27)
$U_z = -U$	at	$z = H'_0$	(zone 4)	(4.28)

4.2.1 Velocity Field & Strain Rates

Zone-2

The velocity field and strain rates satisfying equations (A.9), (4.25) and (4.26) are formulated similarly as in case of deformation mode-I and is given as:

$$U_r = \left[\frac{(1-2\eta)\,Ur}{2(1+\eta)H'_0}\right] \qquad (4.29)$$

$$U_z = -\frac{Uz}{H'_0} \qquad (4.30)$$

$$U_\theta = 0 \qquad (4.31)$$

$$\dot{\varepsilon}_{rr} = \left[\frac{(1-2\eta)\,U}{2(1+\eta)H'_0}\right] \qquad (4.32)$$

$$\dot{\varepsilon}_{\theta\theta} = \left[\frac{(1-2\eta)\,U}{2(1+\eta)H'_0}\right] \qquad (4.33)$$

$$\dot{\varepsilon}_{zz} = -\left(\frac{U}{H'_0}\right) \qquad (4.34)$$

$$\dot{\varepsilon}_{r\theta} = \dot{\varepsilon}_{\theta z} = \dot{\varepsilon}_{zr} = 0 \qquad (4.35)$$

Zone-3

The velocity field and strain rates satisfying equations (A.9), (4.26) and (4.27) are formulated similarly and given as:

$$U_r = \left[\frac{(1-2\eta)(H'_0 - h)\,Ur}{2(1+\eta)H'^2_0}\right] \qquad (4.36)$$

$$U_z = -\left[\frac{(H'_0 - h)\,Uz}{H'^2_0}\right] \qquad (4.37)$$

$$U_\theta = 0 \qquad (4.38)$$

$$\dot{\varepsilon}_{rr} = \left[\frac{(1-2\eta)(H_0' - h)U}{2(1+\eta)H_0'^2}\right] \tag{4.39}$$

$$\dot{\varepsilon}_{zz} = -\left[\frac{(H_0' - h)U}{H_0'^2}\right] \tag{4.40}$$

$$\dot{\varepsilon}_{\theta\theta} = \left[\frac{(1-2\eta)(H_0' - h)U}{2(1+\eta)H_0'^2}\right] \tag{4.41}$$

$$\dot{\varepsilon}_{r\theta} = \dot{\varepsilon}_{\theta z} = \dot{\varepsilon}_{zr} = 0 \tag{4.42}$$

Zone-4

The velocity field and strain rates satisfying equations (A.9), (4.27) and (4.28) are similarly formulated and given as:

$$U_r = \left[\frac{(1-2\eta)(2H_0' - h)Ur}{2(1+\eta)hH_0'}\right] \tag{4.43}$$

$$U_z = -\left[\frac{(2H_0' - h)z}{(H_0' - h)h} - 1\right]\left[\frac{(H_0' - h)U}{H_0'}\right] \tag{4.44}$$

$$U_\theta = 0 \tag{4.45}$$

$$\dot{\varepsilon}_{rr} = \left[\frac{(1-2\eta)(2H_0' - h)U}{2(1+\eta)hH_0'}\right] \tag{4.46}$$

$$\dot{\varepsilon}_{zz} = -\left[\frac{(2H_0' - h)U}{hH_0'}\right] \tag{4.47}$$

$$\dot{\varepsilon}_{\theta\theta} = \left[\frac{(1-2\eta)(2H_0' - h)U}{2(1+\eta)hH_0'}\right] \tag{4.48}$$

$$\dot{\varepsilon}_{r\theta} = \dot{\varepsilon}_{\theta z} = \dot{\varepsilon}_{zr} = 0 \tag{4.49}$$

4.2.2 Energy Dissipations & Average Die Load

The total external energy *'J'* supplied by the die platens during plastic deformation using *'Upper Bound'* approach is given as in equation (3.11).

Zone-2

The internal energy dissipation *'W_i'* is given as:

$$W_i = \left(\frac{2\sigma_0}{\sqrt{3}}\right)\int_V \sqrt{\frac{\varepsilon_{ij}\varepsilon_{ij}}{2}}\,dV$$

$$= \left(\frac{2\sigma_0}{\sqrt{3}}\right) \int_{r=0}^{S} \int_{z=0}^{z=H_0'} \left(\dot{\varepsilon}_{rr}^2 + \frac{\dot{\varepsilon}_{zz}^2}{2}\right)^{\frac{1}{2}} (2\pi r.drdz) \tag{4.50}$$

Substituting equations (4.32) to (4.35) above, solving and simplifying, the internal energy dissipation may be expressed as:

$$W_i = \left[\frac{\sqrt{2}\pi\sigma_0 R_0^2 \alpha^2 U \psi^{1/2}}{\sqrt{3}(\psi - 2)^{1/2}}\right] \tag{4.51}$$

The frictional shear energy dissipation at die-workpiece interface 'W_{f_1}' is given as:

$$W_{f_1} = \int_S \tau |\Delta U| dS = \mu \int_{r=R_0'}^{S} \tau_1 |U_r|_{z=H_0'} (2\pi r dr) \tag{4.52}$$

The frictional shear stress (assuming pressure equal to average pressure) at die-preform interface during closed-die sinter-forging is given as [Refer Equation 1.9]:

$$\tau_1 = \mu \left\{ P_{av} + \rho_0 \varphi_0 \left[1 - \left(\frac{r_{cm} - r}{nS} \right) \right] \right\} \tag{4.53}$$

From equation (4.29), the radial velocity at z = *'H_0'* is given as:

$$|U_r|_{z=H_0'} = \left[\frac{(1-2\eta) Ur}{2(1+\eta) H_0'}\right] \tag{4.54}$$

Substituting equations (4.53) and (4.54) into equation (4.52), solving and simplifying, the frictional shear energy dissipation at die-workpiece interface may be expressed as:

$$W_{f_1} = \left\{ \left[\frac{\pi\mu(1-2\eta) U \left(\alpha^3 R_0^3 - R_0'^3\right)}{3(1+\eta) H_0'} \right] \left\{ P_{av} + \rho_0 \varphi_0 \left(1 - \frac{r_{cm}}{n\alpha R_0} \right) + \left(\frac{3\rho_0 \varphi_0}{4n\alpha R_0} \right) \left[\frac{\alpha^4 R_0^4 - R_0'^4}{\alpha^3 R_0^3 - R_0'^3} \right] \right\} \right\} \tag{4.55}$$

The frictional shear energy dissipation at container-workpiece interface 'W_{f_2}' is zero, *i.e.* $W_{f_2} = 0$, as there is no contact between container and workpiece.

The energy dissipation due to inertia forces 'W_a' *is given as:*

$$W_a = \int_V \rho_i \left(a_r U_r + a_z U_z\right) dV$$

$$= \rho_i \int_{r=0}^{S} \int_{z=0}^{z=H_0'} \left(a_r U_r + a_z U_z\right)\left(2\pi r.drdz\right) \qquad (4.56)$$

Substituting equations (4.29) and (4.30) into equations (3.21) and (3.22) and simplifying, one get:

$$\left(a_r U_r + a_z U_z\right) = \left\{\left[\frac{1-2\eta}{2(1+\eta)}\right]^3 r^2 - z^2\right\}\left(\frac{U}{H_0'}\right)^3 + \dot{U} \qquad (4.57)$$

Substituting equation (4.57) into equation (4.56), solving and simplifying, the energy dissipation due to inertia forces may be expressed as:

$$W_a = \left(\frac{\pi\rho_i \alpha^2 R_0^2 U}{3}\right)\left\{\begin{array}{l}\left[\dfrac{3(1-2\eta)^3 \alpha^2 R_0^2}{16(1+\eta)^3 H_0'^2} - 1\right] U^2 \\ +3\dot{U}H_0'\end{array}\right\} \qquad (4.58)$$

<u>Zone-3</u>

The internal energy dissipation *'W_i'* is given as:

$$W_i = \left(\frac{2\sigma_0}{\sqrt{3}}\right)\int_V \sqrt{\frac{\varepsilon_{ij}\varepsilon_{ij}}{2}} dV$$

$$= \left(\frac{2\sigma_0}{\sqrt{3}}\right)\int_{r=S}^{R_0} \int_{z=0}^{z=(H_0'-h)} \left(\dot{\varepsilon}_{rr}^2 + \frac{\dot{\varepsilon}_{zz}^2}{2}\right)^{\frac{1}{2}} \left(2\pi r.drdz\right) \qquad (4.59)$$

Substituting equations (4.39) to (4.42) above, solving and simplifying, the internal energy dissipation may be expressed as:

$$W_i = \left[\frac{\sqrt{2}\pi\sigma_0 \left(H_0' - h\right)^2 R_0^2 \left(1-\alpha\right)^2 U \psi^{1/2}}{\sqrt{3} H_0'^2 \left(\psi - 2\right)^{1/2}}\right] \qquad (4.60)$$

The frictional shear energy dissipation at die-workpiece interface 'W_{f_1}' is zero, *i.e.* $W_{f_1} = 0$, as there is no contact between die and workpiece. As discussed earlier, the present analysis considers equalization of average pressure during constraint deformation of axi-symmetric cylindrical preform keeping the container reaction pressure distribution reasonably accurate. Therefore, the average pressure at die-preform interface is considered to be same as that of container-preform

interface. Thus, the frictional shear energy dissipation at container-workpiece interface 'W_{f_2}' is given as:

$$W_{f_2} = \int_S \tau |\Delta U| dS = \mu \int_{z=0}^{H_0' - h} \tau_2 \left| U_z \right|_{r=R_0} \left(2\pi R_0 dz \right) \tag{4.61}$$

The frictional shear stress (assuming pressure term equal to average pressure) at container-preform interface during closed-die sinter-forging is given as [Refer Equation 1.10]:

$$\tau_2 = \mu \left\{ P_{av} + \rho_0 \varphi_0 \left[1 - \left(\frac{z_{cm} - z}{n H_0'} \right) \right] \right\} \tag{4.62}$$

From equation (3.37), the axial velocity at r = *'R_0'* is given as:

$$U_z = -\left[\frac{(H_0' - h) U z}{H_0'^2} \right] \tag{4.63}$$

Substituting equations (4.62) and (4.63) into equation (4.61), solving and simplifying, the frictional shear energy dissipation at container-workpiece interface may be expressed as:

$$W_{f_2} = \left\{ \left(\frac{\pi \mu R_0 (H_0' - h)^3 U}{H_0'^2} \right) x \left\{ p_{av} + \rho_0 \varphi_0 \left(1 - \frac{z_{cm}}{n H_0'} \right) + \left[\frac{2 \rho_0 \varphi_0 (H_0' - h)}{3 n H_0'} \right] \right\} \right\} \tag{4.64}$$

The energy dissipation due to inertia forces 'W_a' *is given as:*

$$W_a = \int_V \rho_i \left(a_r U_r + a_z U_z \right) dV$$

$$= \rho_i \int_{r=S}^{R_0} \int_{z=0}^{z=(H_0' - h)} \left(a_r U_r + a_z U_z \right) (2\pi r . dr dz) \tag{4.65}$$

Substituting equations (4.36) and (4.37) into equations (3.21) and (3.22) and simplifying, one get:

$$\left(a_r U_r + a_z U_z \right) = \left\{ \left[\frac{1 - 2\eta}{2(1 + \eta)} \right]^3 r^2 - z^2 \right\} \left[\frac{(H_0' - h) U}{H_0'^2} \right]^3 + \dot{U} \tag{4.66}$$

Substituting equation (4.66) into equation (4.65), solving and simplifying, the energy dissipation due to inertia forces may be expressed as:

$$W_a = \left[\frac{\pi\rho_i R_0^2\left(1-\alpha^2\right)U}{3}\right]\left\{\begin{array}{l}\left[\dfrac{3(1-2\eta)^3 R_0^2\left(1+\alpha^2\right)}{16(1+\eta)^3\left(H_0'-h\right)^2}-1\right] \\ x\left[\left(\dfrac{H_0'-h}{H_0'}\right)^6 U^2\right]+3\dot{U}\left(H_0'-h\right)\end{array}\right\} \quad (4.67)$$

Zone-4

The internal energy dissipation *'W_i'* is given as:

$$W_i = \left(\frac{2\sigma_0}{\sqrt{3}}\right)\int_V \sqrt{\frac{\varepsilon_{ij}\varepsilon_{ij}}{2}}dV$$

$$= \left(\frac{2\sigma_0}{\sqrt{3}}\right)\int_{r=S}^{R_0}\int_{z=0}^{z=z_0}\left(\dot{\varepsilon}_{rr}^2+\frac{\dot{\varepsilon}_{zz}^2}{2}\right)^{\frac{1}{2}}\left(2\pi r.drdz\right) \quad (4.68)$$

Substituting equations (4.46) to (4.49) above, solving and simplifying, the internal energy dissipation may be expressed as:

$$W_i = \left[\frac{\sqrt{2}\pi\sigma_0\left(H_0'-h\right)^2 R_0^2\left(1-\alpha\right)^2 U\psi^{1/2}}{\sqrt{3}H_0'^2\left(\psi-2\right)^{1/2}}\right] \quad (4.69)$$

The frictional shear energy dissipation at die-workpiece 'W_{f_1}' and container-workpiece interfaces are zero 'W_{f_2}', *i.e.* $W_{f_1} = W_{f_2} = 0$, as there is no contact between die and container with workpiece.

The energy dissipation due to inertia forces 'W_a' *is given as:*

$$W_a = \int_V \rho_i\left(a_r U_r + a_z U_z\right)dV$$

$$= \rho_i\int_{r=S}^{R_0}\int_{z=0}^{z=z_0}\left(a_r U_r + a_z U_z\right)\left(2\pi r.drdz\right) \quad (4.70)$$

Substituting equations (4.43) and (4.44) into equations (3.21) and (3.22) and simplifying, one get:

$$\left(a_r U_r + a_z U_z\right) = \left\{ \begin{array}{l} \left[\dfrac{(1-2\eta)(2H_0' - h)U}{2(1+\eta)hH_0'}\right]^3 r^2 \\ -\left\{ \begin{array}{l} \left[\dfrac{(2H_0' - h)z}{(H_0' - h)h} - 1\right]^2 \\ \left[\dfrac{(2H_0' - h)(H_0' - h)^2 U^3}{hH_0'^3}\right] \end{array} \right\} + U\dot{U} \end{array} \right\} \qquad (4.71)$$

Substituting equation (4.71) into equation (4.70), solving and simplifying, the energy dissipation due to inertia forces may be expressed as:

$$W_a = \left[\frac{\pi\rho_i R_0^2 (1-\alpha^2) U}{3}\right] \left\{ \begin{array}{l} \left[\dfrac{3(1-2\eta)^3 R_0^2 (1+\alpha^2)}{16(1+\eta)^3 (H_0' - h)^2} - 1\right] \\ \left[\left(\dfrac{H_0' - h}{H_0'}\right)^6 U^2\right] + 3\dot{U}(H_0' - h) \end{array} \right\} \qquad (4.72)$$

The average forging load may be computed similarly as in deformation mode-I. The dynamic or inertia effects *i.e.* effect of die velocity on relative magnitudes of various energy dissipations and average die load involved during closed-die sinter-forging of cylindrical preform to double-hub-flange component is illustrated using concepts of inertia factor 'ξ' (Refer Equation 3.28) and load factor 'ζ' (Refer Equation 3.29) as discussed in the previous sections.

4.3 RESULTS & PARAMETRIC DISCUSSION

To illustrate the dynamic effects during closed-die sinter-forging of cylindrical preforms, a typical data of preform and various deformation characteristics compatible with corresponding experimental work has been considered as follows:
$R_0 = 15$ mm; $R'_0 = 10$ mm; $H_0 = 20$ mm; $\psi = 0.80$; $\rho_0\phi_0 = 0.30$ P_{av}; $\sigma_0 = 6.25$ kg/mm^2; $\rho_i = 2 \times 10^3$ kg/m^3; $n = 2$; $\rho_0 = 0.75$; $(H'_0 / R_0) = 0.25$ to 1.0; $\mu = 0.20$ (high interfacial friction) and 0.05 (low interfacial friction); Acceleration = 0.1 and 1.0 m/s^2 and U = 0.001 to 10 m/sec.

Figure 4.5 shows theoretical variation of inertia energy with die velocity and acceleration for different deformation modes during flashless closed-die sinter-forging of cylindrical preform to double-hub-

flange component for complete die cavity fill. It is clearly noticeable from the figure that inertia energy dissipation is high for deformation mode I. This may be due the fact that deformation mode I considers a large sized dead zone, as compared to the deformation mode II and hence, absorbs large amount of external energy supplied by die platens to impart the required inertia. Figure 4.6 shows variation of inertia factor *'ξ'* with die velocity and it can be clearly observed that inertia factor increases exponentially with die velocity and preform aspect ratio. Also, it is higher for deformation mode I. Thus, for sinter-forging operations at higher die velocities, the magnitude of inertia energy dissipation becomes comparable to that of internal and frictional shear energy dissipations and must be taken care during analysis.

Figure 4.7 shows the comparison of average die load for deformation modes I and II with ratio of unfilled volume of die to component's actual volume for low and high preform aspect ratios during flashless closed-die sinter-forging of cylindrical preform to double-hub-flange component. The figure clearly shows that die load requirements are very high for complete filling of die cavity. This is obvious because higher die loads are required to force sintered preform materials into the cavities of impression during final stages of sinter-forging operation. The die load requirements are also high for higher preform aspect ratio. This is due the fact that slender preform makes contact with container walls comparatively earlier than shorter preforms and hence, exhibit higher interfacial frictional shear resistance. It can also be observed that load data are closer to each other for same preform aspect ratio irrespective of deformation modes during initial stage of closed-die sinter-forging operation, but at the end of operation during complete die fill, the effect of deformation modes dominates over the effect of preform aspect ratio.

The load factor 'ζ' decreases rapidly with the die velocity and become asymptote with x-axis at higher die speeds as shown in figure 4.8. The die loads are considered at the maximum reduction of preforms, *i.e.* during complete die filling stage. The decrease in die load with die velocity is attributed due to the shorter contact time of preform under deformation. Also, the load requirement under deformation mode I is higher than mode II. Thus, deformation mode I is more effective for predicting the closed-die forging load for complete die fills during flashless closed-die sinter-forging of axi-symmetric cylindrical preform as it gives higher estimate of theoretical load and hence, will always be preferred during equipment and tool design process.

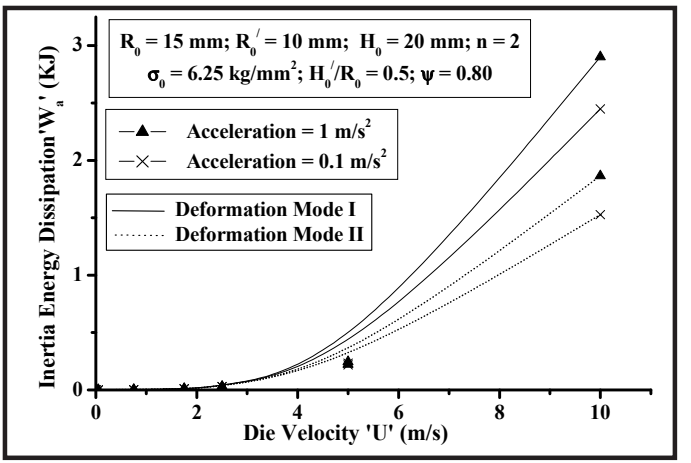

Figure 4.5: Variation of inertia energy with die velocity for different deformation modes during flashless closed-die sinter-forging.

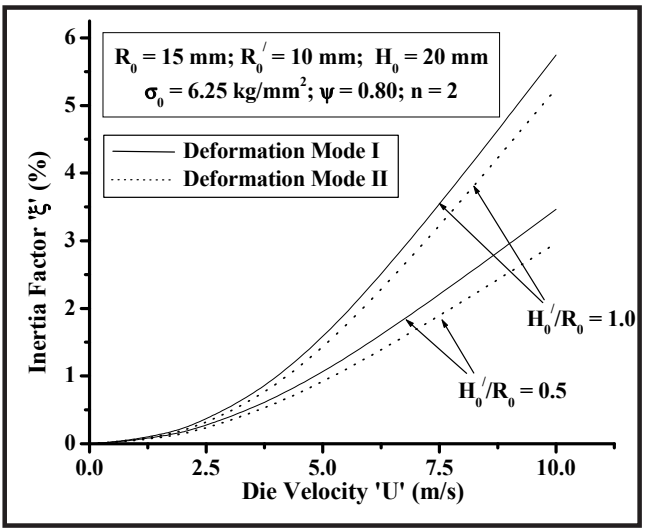

Figure 4.6: Variation of inertia factor with die velocity for different deformation modes during flashless closed-die sinter-forging.

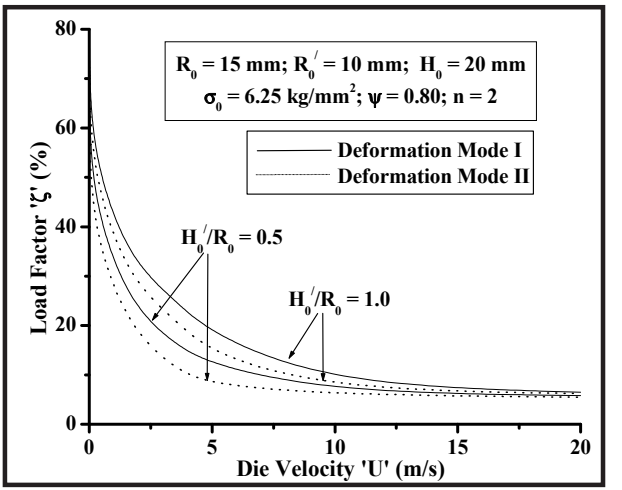

Figure 4.7: Variation of average forging load with ratio of unfilled volume of die to component's actual volume and aspect ratio for different deformation modes during flashless closed-die sinter-forging.

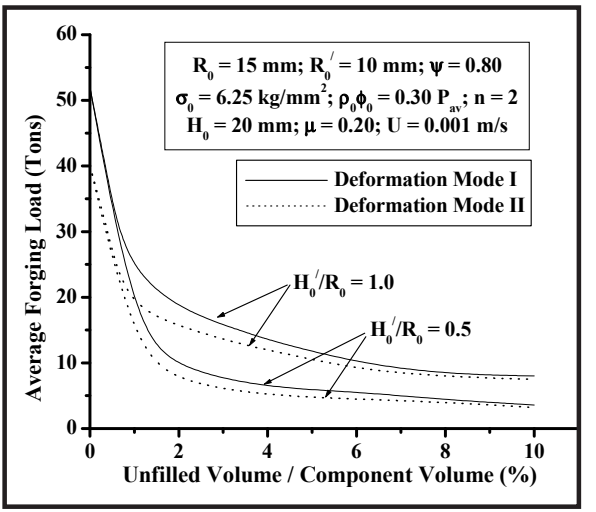

Figure 4.8: Variation of load factor with die velocity for different deformation modes during flashless closed-die sinter-forging.

Figure 4.9 shows experimental and theoretical variation of average die load with the ratio of unfilled volume of die to component's actual

volume for different preform aspect ratio and die velocity during flashless closed-die sinter-forging. It is undoubtedly apparent that average forging load increases exponentially at the end of sinter-forging operation because of high constraint deformation and resistance against metal flow during final stages of the die filling. The load curves are also high for higher preform aspect ratio, though the contact between preform and container walls will be made at lower loads as compared with the shorter preforms. This appears to be mainly of two prominent consequences. First, the geometry of corners differs with preform aspect ratio, due to difference in barrelling during free upsetting stage of deformation. Second, the preform with lower aspect ratio will have lower contact areas with container walls, resulting into low friction shear energy dissipations.

The experimental and theoretical variation of average forging load for complete die filling with preform aspect ratio for different die velocity and interfacial friction condition during flashless closed-die sinter-forging is shown in figure 4.10. The figure suggests that average forging load increases with preform aspect ratio and is higher for low die velocity. The reduction in die load with die velocity is attributed due to the enhanced dynamic effects during mechanical processing of sintered materials, especially at higher die velocities. Also, the low interfacial friction (vaseline) condition resulted into corresponding lower die load requirements, as compared with high (dry) interfacial friction condition due to better metal flow conditions. The experimental data of average forging load for aspect ratios 1.0 and 0.5 have also been shown in the figure, which have been found in close agreement to the corresponding theoretical data.

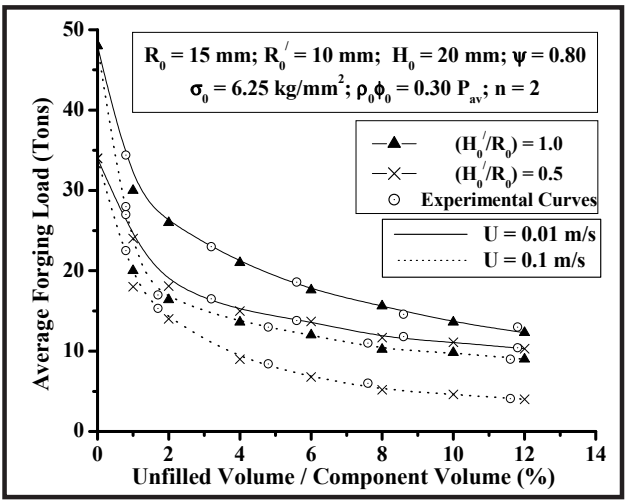

Figure 4.9: Variation of average forging load with ratio of unfilled volume of die to component's actual volume during flashless closed-die sinter-forging.

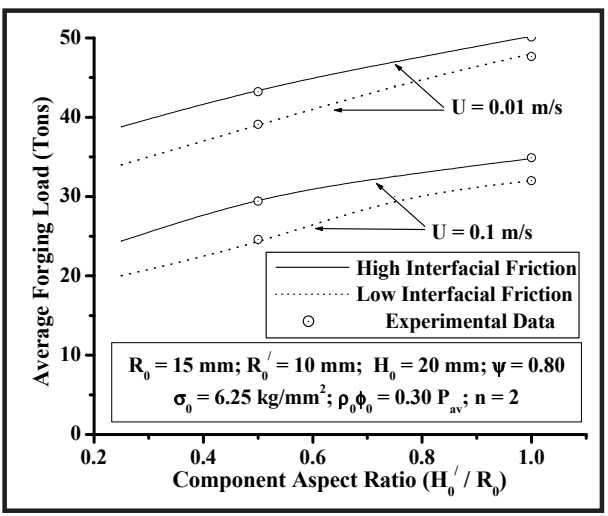

Figure 4.10: Variation of average forging load with component's aspect ratio during flashless closed-die sinter-forging for complete die fill.

CHAPTER - 5
ROTARY FORGING OF AXI-SYMMETRIC SINTERED POWDER PREFORM

Outline of the Chapter: *5.1 Indented Contact Area; 5.2 Indentation Phase; 5.2.1 Velocity Field & Strain Rates; 5.2.2 Power Dissipations & Average Indentation Load; 5.3 Rotary Phase; 5.3.1 Velocity Field & Strain Rates; 5.3.2 Power Dissipations & Average Rotary Load; 5.4 Parametric Results & Discussion*

The present problem considers rotary sinter-forging of axi-symmetric preform at cold conditions between a fixed flat bottom die and a rotating conical upper die with inclined cone axis, so that the indented area is parallel to the horizontal plane. The complete deformation problem is segmented into two parts namely, indentation and rotary phases. The present research work considers some assumptions in addition to common assumptions of sinter-forging, which are as follows [*Kubo & Hirai, 1977; Stranding & Appleton, 1979*]:

a. The mushrooming of final sintered component during rotary sinter-forging has been neglected.

b. The deformation during rotary sinter-forging is accompanied by circumferential flow of sintered material, *i.e.* $U_\theta \neq 0$.

c. The radial flow is not uniform throughout the circumference of indented area. It is maximum at center of horizontal symmetry axis and gradually decreases towards the ends and become zero.

5.1 INDENTED CONTACT AREA

Figure 5.1 shows the schematic representation of rotary sinter-forging process using upper conical and flat lower dies along with the coordinate axes chosen during analysis. The cone axis of upper conical die is swelled by an angle *'α'* with respect to vertical axis, which is also its skew contact angle. This makes its nearest generator to the preform top surface horizontal. It is assumed that during indentation phase, the upper conical die is fed axially to an indentation depth *'h_i'* into the preform top surface having initial height and radius as *'H_0'* and *'R_0'* respectively. This conical indented contact area is projected on the *'XOY'* plane and only half of the area has been considered for the

analysis due to its symmetry about x-axis a shown in figure 5.2. A typical illustration of conical indented contact area generated on preform top surface, which is parallel to horizontal plane is shown in figure 5.3.

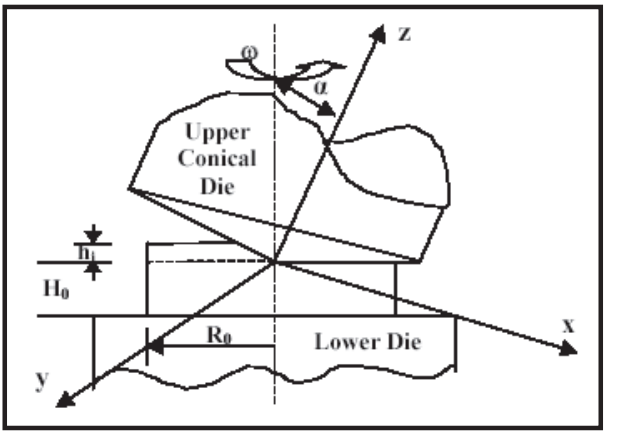

Figure 5.1: Schematic diagram of rotary sinter-forging.

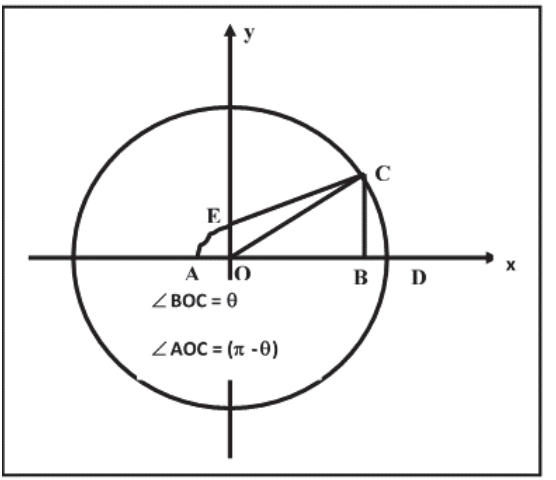

Figure 5.2: Indented contact area on preform top surface projected on XOY plane.

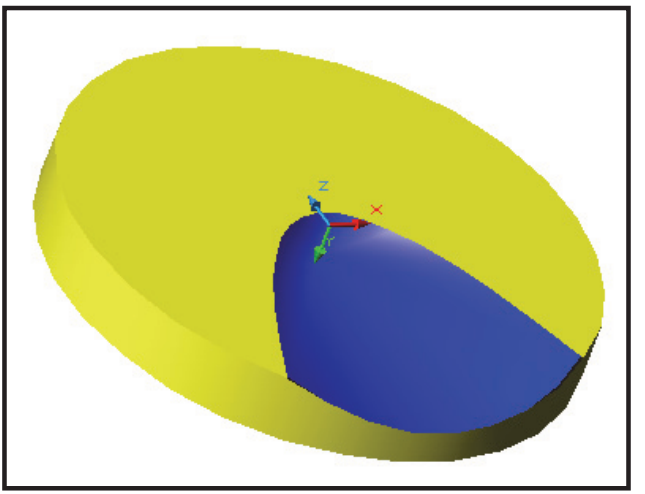

Figure 5.3: Schematic representation of conical indented contact area on preform top surface.

The equations for conical surface of upper conical die and flat top surface of axi-symmetric preform are given as [*Zhang, 1984*]:

$$x^2 + y^2 - \left(\frac{z^2}{\tan^2 \alpha}\right) = 0 \tag{5.1}$$

$$\left(\frac{z \cos \alpha}{h_i}\right) - \left(\frac{x \tan \alpha}{h_i \cos \alpha}\right) = 1 \tag{5.2}$$

Equations (5.1) and (5.2) are solved simultaneously and hence, equation for conical indented surface created on top surface of axi-symmetric preform is given as:

$$y^2 = \left(\frac{h_i^2}{\tan \alpha \cos^2 \alpha}\right) + \left(\frac{2h_i}{\tan \alpha \cos^3 \alpha}\right) x - \left(\frac{1}{\cos^4 \alpha} - 1\right) x^2 \tag{5.3}$$

Neglecting higher order terms of equation (5.3) for simplicity during further analysis, the equation for curve *'AEC'* in *'XOY'* plane may be given as:

$$y = \left(\frac{h_i}{\tan \alpha}\right) \left[\left(\frac{2x \tan \alpha}{h_i}\right) + 1\right]^{1/2} \tag{5.4}$$

The equation of preform top surface in *'XOY'* plane is a circle and may be expressed as:

$$x^2 + y^2 = R_0^2 \tag{5.5}$$

The coordinates of points *'A'* and *'C'* can be obtained by simultaneously solving equations (5.4) and (5.5) and are given as:

$$\left(x_A, y_A\right) \equiv \left(-\frac{h_i}{2\tan\alpha}, 0\right) \tag{5.6 a}$$

$$\left(x_C, y_C\right) \equiv \left\{\left[R_0 - \frac{h_i}{\tan\alpha}\right], \left[\left(\frac{h_i}{\tan\alpha}\right)\left(\frac{2R_0\tan\alpha}{h_i} - 1\right)^{1/2}\right]\right\} \tag{5.6 b}$$

The equation for curve *'AEC'* may also be expressed in polar coordinates as [*Choi], 1997]*:

$$r = \left[\frac{h_i}{\tan\alpha\left(1+\cos P\theta\right)}\right] = \left[\frac{2R_0 Q}{\left(1+\cos P\theta\right)}\right] \tag{5.7}$$

where,

$$Q = \left(\frac{h_i}{2R_0\tan\alpha}\right) \text{ and } P = \left(\frac{\pi}{2\alpha}\right)$$

Thus, the indented contact area on top surface of axi-symmetric preform may be computed in two parts as follows:

$$A_{av} = 2\left[\int_{\theta=0}^{\alpha}\int_{r=0}^{R_0}\left(r.dr.d\theta\right) + \int_{\theta=\alpha}^{\pi}\int_{r=0}^{r=\left(2R_0Q/1+\cos P\theta\right)}\left(r.dr.d\theta\right)\right] \tag{5.8}$$

Integrating above equation and simplifying, the indented contact area may be given as:

$$A_{av} = \left[R_0^2\alpha + \left(\frac{2R_0^2Q^2}{P}\right)\left(\tan\frac{P\pi}{2} + \tan^3\frac{P\pi}{2} + \frac{4}{3}\right)\right] \tag{5.9}$$

Hence, indented contact area rate may be expressed as:

$$ICR = \left(\frac{A_{av}}{\pi R_0^2}\right) \tag{5.10}$$

5.2 INDENTATION PHASE

The compatibility equation [Refer Equation A.9] and boundary conditions during indentation phase of rotary sinter-forging are given as:

$$\dot{\varepsilon}_{rr} + \dot{\varepsilon}_{\theta\theta} + \left(\frac{1-2\eta}{1+\eta}\right)\dot{\varepsilon}_{zz} = 0 \tag{5.11}$$

$U_z = 0$ at $z = 0$ (5.12)

$U_z = -U$ at $z = h_i$ (5.13)

$U_\theta = 0$ at $r = 0$ and $\theta = \alpha$ (5.14)

5.2.1 Velocity Field & Strain Rates

The velocity field and strain rates satisfying equations (A.9), (5.12) to (5.14) are given as [Refer Appendix E]:

$$U_r = \left[\frac{(1-2\eta)\beta e^{-\beta z/h_i} Ur(1+\cos P\theta)}{2(1+\eta)(1-e^{-\beta})h_i}\right] \tag{5.15}$$

$$U_\theta = -\left[\frac{(1-2\eta)\beta e^{-\beta z/h_i} Ur\sin P\theta}{(1+\eta)P(1-e^{-\beta})h_i}\right] \tag{5.16}$$

$$U_z = -\left(\frac{1-e^{-\beta z/h_i}}{1-e^{-\beta}}\right)U \tag{5.17}$$

$$\dot{\varepsilon}_{rr} = \frac{\partial U_r}{\partial r} = \left[\frac{(1-2\eta)\beta e^{-\beta z/h_i} U(1+\cos P\theta)}{2(1+\eta)(1-e^{-\beta})h_i}\right] \tag{5.18}$$

$$\dot{\varepsilon}_{\theta\theta} = \left[\frac{U_r}{r} + \frac{1}{r}\frac{\partial U_\theta}{\partial \theta}\right] = \left[\frac{(1-2\eta)\beta e^{-\beta z/h_i} U(1-\cos P\theta)}{2(1+\eta)(1-e^{-\beta})h_i}\right] \tag{5.19}$$

$$\dot{\varepsilon}_{zz} = \frac{\partial U_z}{\partial z} = -\left[\frac{\beta e^{-\beta z/h_i} U}{(1-e^{-\beta})h_i}\right] \tag{5.20}$$

$$\dot{\varepsilon}_{r\theta} = \frac{1}{2}\left[\frac{1}{r}\frac{\partial U_r}{\partial \theta} + \frac{\partial U_\theta}{\partial r} - \frac{U_\theta}{r}\right] = -\left[\frac{(1-2\eta)\beta e^{-\beta z/h_i} UP\sin P\theta}{4(1+\eta)(1-e^{-\beta})h_i}\right] \tag{5.21}$$

$$\dot{\varepsilon}_{\theta z} = \frac{1}{2}\left[\frac{\partial U_\theta}{\partial z} + \frac{1}{r}\frac{\partial U_z}{\partial r}\right] = \left[\frac{(1-2\eta)\beta^2 e^{-\beta z/h_i} Ur\sin P\theta}{(1+\eta)P(1-e^{-\beta})h_i^{\,2}}\right] \tag{5.22}$$

$$\dot{\varepsilon}_{zr} = \frac{1}{2}\left[\frac{\partial U_r}{\partial z} + \frac{\partial U_z}{\partial r}\right] = -\left[\frac{(1-2\eta)\beta^2 e^{-\beta z/h_i} Ur(1+\cos P\theta)}{4(1+\eta)(1-e^{-\beta})h_i^{\,2}}\right] \tag{5.23}$$

5.2.2 Power Dissipations & Average Indentation Load

The total external power *'J'* supplied by the die platens during rotary sinter-forging using *'Upper Bound'* approach is given as:

$$J = \frac{2\sigma_o}{\sqrt{3}} \int_V \sqrt{\frac{1}{2}\dot{\varepsilon}_{ij}\dot{\varepsilon}_{ij}}\, dV + \int_S \tau \left|\Delta U\right| dS \qquad (5.24)$$

The first term on the right side denotes internal energy dissipation *'W_i'* and the second term denotes frictional shear energy dissipation *'W_f'*. The energy dissipation have been computed by integrating the respective expressions into two parts, namely, from θ = *'0'* to *'α'* and θ = *'α'* to *'π'*. The corresponding expressions for radial distance are r = *'R_0'* and r = *{[h_i /[tanα (1+cosPθ)]}'* respectively [*Zhang, 1984*].

The internal energy dissipation *'W_i'* during indentation phase of rotary sinter-forging is given as:

$$W_i = \frac{\sigma_o}{\sqrt{3}} \int_V \left(\frac{\dot{\varepsilon}_{ij}\dot{\varepsilon}_{ij}}{2} \right)^{1/2} dV \qquad (5.25)$$

The above expression may also be expressed as:

$$W_i = \left(\frac{\sigma_o}{\sqrt{3}} \right) \left\{ \int_{z=0}^{h_i} \int_{\theta=0}^{\alpha} \int_{r=0}^{R_o} \left(\frac{\dot{\varepsilon}_{ij}\dot{\varepsilon}_{ij}}{2} \right)^{1/2} (r dr d\theta dz) + \int_{z=0}^{h_i} \int_{\theta=\alpha}^{\pi} \int_{r=0}^{r=\left[\frac{h_i}{\tan\alpha(1+\cos P\theta)}\right]} \left(\frac{\dot{\varepsilon}_{ij}\dot{\varepsilon}_{ij}}{2} \right)^{1/2} (r dr d\theta dz) \right\} \qquad (5.26)$$

Substituting equations (5.18) to (5.23) above, solving and simplifying, the internal energy dissipation may be expressed as:

$$W_i = \left[\frac{(1-2\eta)\sigma_0 \sqrt{\upsilon} U h_i^{\,2}}{96\sqrt{3}(1+\eta) P \tan^2\alpha} \right] \left\{ \left\{ \left(\frac{3PR_0^2 \upsilon \tan^2\alpha}{2h_i^{\,2}} \right) \left[16\upsilon + P^2 + \frac{\beta^2 R_0^2 (3\pi+8)}{4\pi h_i^{\,2}} \right] \right\} + \left\{ \left(4\upsilon + \frac{\beta^2}{8\tan^2\alpha} \right) \left(\tan^3 \frac{\pi P}{2} + 3\tan\frac{\pi P}{2} + 4 \right) \right\} + \left\{ \left(\frac{3P^2}{2} \right) \left[\frac{2}{P} \left(\tan\frac{\pi P}{2} - 1 \right) + (\pi - \alpha) \right] \right\} \right\} \qquad (5.27)$$

where,

$$\upsilon = \left[\frac{(1-2\eta)^2}{2(1+\eta)^2+(1-2\eta)^2}\right]$$

The frictional shear energy dissipation at die-workpiece interface *'W_f'* during indentation phase of rotary sinter-forging is given as:

$$W_f = \int_S \tau.|\Delta U|.dS$$

$$W_f = \int_{\theta=0}^{\theta=\alpha}\int_{r=0}^{r=R_0} |\tau|_{z=h_i}|\Delta U|_{z=h_i}(rdrd\theta) + \int_{\theta=\alpha}^{\theta=\pi}\int_{r=0}^{r=\left[\frac{h_i}{\tan\alpha(1+\cos P\theta)}\right]} |\tau|_{z=h_i}|\Delta U|_{z=h_i}(rdrd\theta) \quad (5.28)$$

The frictional shear stress (assuming pressure term equal to average pressure) during rotary sinter-forging at z = *'h_i'* is given as [Refer Equation 1.11]:

$$\tau = \mu\left\{P_{av} + \rho_0\varphi_0\left[1-\left(\frac{r_{rm}-r}{nR_0}\right)\right]\right\} \quad (5.29)$$

The deformation during rotary sinter-forging consists both of radial and circumferential flow of preform material, thus, resultant magnitude of velocity along the direction of frictional shear stress is given as:

$$|\Delta U| = \left|\left(U_r^2+U_\theta^2\right)^{1/2}\right|_{Z=h_i} \quad (5.30)$$

Substituting equations (5.15) and (5.16) above, one get:

$$\left|\left(U_r^2+U_\theta^2\right)^{1/2}\right|_{z=h_i} = \left\{\begin{array}{l}\left[\dfrac{(1-2\eta)\beta e^{-\beta}Ur}{(1+\eta)\left(1-e^{-\beta}\right)h_i}\right] \\ \left[\left(\dfrac{1+\cos P\theta}{2}\right)^2+\left(\dfrac{\sin P\theta}{P}\right)\right]^{1/2}\end{array}\right\} \quad (5.31)$$

Substituting equations (5.29) and (5.31) into equation (5.28), solving and simplifying, the frictional shear energy dissipation may be expressed as:

$$W_f = \left\{ \begin{array}{l} \left[\dfrac{(1-2\eta)\mu\beta e^{-\beta z/h_i} U h_i^{\,2}}{36(1+\eta)\left(1-e^{-\beta}\right) P \tan^3\alpha} \right] \\ \left\{ \left(\dfrac{6PR_0^3 \tan^3\alpha}{h_i^{\,3}} \right) \left[P_{av} + \rho_0 \varphi_0 \left(1 - \dfrac{r_{rm}}{nR_0} + \dfrac{3}{4n} \right) \right] \right\} \\ \left\{ \left[\left(\tan\alpha + \dfrac{1}{P} \right) \left(1 + \dfrac{2}{P^2} \right) + \left(\dfrac{4}{P^3} \right) \right] \right. \\ + \left\{ \left[P_{av} + \rho_0 \varphi_0 \left(1 - \dfrac{r_{rm}}{nR_0} \right) \right] \left(\tan^3 \dfrac{\pi P}{2} + 3\tan\dfrac{\pi P}{2} + 4 \right) \right\} \\ + \left\{ \left(\dfrac{3\rho_0 \varphi_0 h_i}{10nP^2 R_0 \tan\alpha} \right) \left(3\tan^5 \dfrac{\pi P}{2} + 5\tan^3 \dfrac{\pi P}{2} + 3 \right) \right\} \end{array} \right. \quad (5.32)$$

The total power dissipations may be computed by substituting equations (5.27) and (5.32) into equation (5.24) and average forging load during indentation phase of rotary sinter-forging may be computed by below equation:

$$F_i = J(U)^{-1} A_{av} \quad (5.33)$$

5.3 ROTARY PHASE

The compatibility equation [Refer Equation A.9] and boundary conditions during rotary phase of rotary sinter-forging are given as:

$$\dot{\varepsilon}_{rr} + \dot{\varepsilon}_{\theta\theta} + \left(\frac{1-2\eta}{1+\eta} \right) \dot{\varepsilon}_{zz} = 0 \quad (5.34)$$

$U_z = 0$ at $z = 0$ (5.35)

$U_z = -\omega \sin\alpha$ at $z = h_i$ (5.36)

$U_\theta = 0$ at $r = 0$ & $\theta = \alpha$ (5.37)

5.3.1 Velocity Field & Strain Rates

The velocity field and strain rates satisfying equations (A.9), (5.35) to (5.37) for rotary phase is derived similarly as during indentation phase and given as:

$$U_r = \left[\frac{(1-2\eta)\beta e^{-\beta Z/h_i} r^2 \omega \sin\alpha (1+\cos P\theta)}{2(1+\eta)(1-e^{-\beta})h_i} \right] \tag{5.38}$$

$$U_\theta = -\left[\frac{(1-2\eta)\beta e^{-\beta Z/h_i} r^2 \omega \sin\alpha \sin P\theta}{(1+\eta)P(1-e^{-\beta})h_i} \right] \tag{5.39}$$

$$U_z = -\left[\frac{(1-e^{-\beta Z/h_i}) r\omega \sin\alpha}{1-e^{-\beta}} \right] \tag{5.40}$$

$$\dot{\varepsilon}_{rr} = \frac{\partial U_r}{\partial r} = \left[\frac{(1-2\eta)\beta e^{-\beta Z/h_i} r\omega \sin\alpha (1+\cos P\theta)}{(1+\eta)(1-e^{-\beta})h_i} \right] \tag{5.41}$$

$$\dot{\varepsilon}_\theta = \left[\frac{U_r}{r} + \frac{1}{r}\frac{\partial U_\theta}{\partial \theta} \right] = \left[\frac{(1-2\eta)\beta e^{-\beta Z/h_i} r\omega \sin\alpha (1-\cos P\theta)}{2(1+\eta)(1-e^{-\beta})h_i} \right] \tag{5.42}$$

$$\dot{\varepsilon}_z = \frac{\partial U_Z}{\partial Z} = -\left[\frac{\beta e^{-\beta Z/h_i} r\omega \sin\alpha}{(1-e^{-\beta})h_i} \right] \tag{5.43}$$

$$\begin{aligned} \dot{\varepsilon}_{r\theta} &= \frac{1}{2}\left[\frac{1}{r}\frac{\partial U_r}{\partial \theta} + \frac{\partial U_\theta}{\partial r} - \frac{U_\theta}{r} \right] \\ &= -\left[\frac{(1-2\eta)\beta e^{-\beta Z/h_i} r\omega \sin\alpha \sin P\theta (P^2-2)}{4(1+\eta)(1-e^{-\beta})h_i P} \right] \end{aligned} \tag{5.44}$$

$$\dot{\varepsilon}_{\theta z} = \frac{1}{2}\left[\frac{\partial U_\theta}{\partial Z} + \frac{1}{r}\frac{\partial U_Z}{\partial \theta} \right] = \left[\frac{(1-2\eta)\beta^2 e^{-\beta Z/h_i} r^2 \omega \sin\alpha \sin P\theta}{(1+\eta)P(1-e^{-\beta})h_i^{\,2}} \right] \tag{5.45}$$

$$\begin{aligned} \dot{\varepsilon}_{zr} &= \frac{1}{2}\left[\frac{\partial U_r}{\partial z} + \frac{\partial U_Z}{\partial r} \right] \\ &= -\left[\frac{(1-2\eta)\beta^2 e^{-\beta Z/h_i} r^2 \omega \sin\alpha (1+\cos P\theta)}{2(1+\eta)(1-e^{-\beta})h_i^{\,2}} \right] \end{aligned} \tag{5.46}$$

5.3.2 Power Dissipations & Average Rotary Load

The internal energy dissipation *'W_i'* during rotary phase of rotary sinter-forging is given as:

$$W_i = \left(\frac{\sigma_o}{\sqrt{3}}\right)\int_v \left(\frac{\dot{\varepsilon}_{ij}\dot{\varepsilon}_{ij}}{2}\right)^{1/2} dv$$

$$= \left(\frac{\sigma_o}{\sqrt{3}}\right)\int_{z=0}^{h_i}\int_{\theta=\alpha}^{\pi}\int_{r=0}^{r=\left[\frac{h_i}{\tan\alpha(1+\cos P\theta)}\right]} \left(\frac{\dot{\varepsilon}_{ij}\dot{\varepsilon}_{ij}}{2}\right)^{1/2} (rdrd\theta dz) \qquad (5.47)$$

Substituting equations (5.41) to (5.46) above, solving and simplifying, the internal energy dissipation may be expressed as:

$$W_i = \left[\frac{2\sigma_0(1-2\eta)\omega\sin\alpha h_i^{\,3}}{15\sqrt{6}(1+\eta)\tan^3\alpha}\right]\left[\begin{Bmatrix}\left(1+\frac{3\beta^2}{40\tan\alpha}\right)\\ \left(\tan^5\frac{P\pi}{2}+\frac{5}{3}\tan^3\frac{P\pi}{2}+5\tan\frac{P\pi}{2}+\frac{43}{12}\right)\end{Bmatrix} + \frac{1}{16}\tan^5\frac{P\pi}{2}+\frac{5}{4}\tan\frac{P\pi}{2}+\frac{21}{16}\right] \qquad (5.48)$$

The frictional shear energy dissipation at die-workpiece interface *'W_f'* during rotary phase of rotary sinter-forging is given as:

$$W_f = \int_S \tau.|\Delta U|.dS = \int_{\theta=\alpha}^{\theta=\pi}\int_{r=0}^{r=\left[\frac{h_i}{\tan\alpha(1+\cos P\theta)}\right]} |\tau|_{z=h_i}|\Delta U|_{z=h_i}(rdrd\theta) \qquad (5.49)$$

The frictional shear stress (assuming pressure term equal to average pressure) during rotary sinter-forging at z = *'h_i'* is given as [Refer Equation 1.11]:

$$\tau = \mu\left\{P_{av} + \rho_0\varphi_0\left[1-\left(\frac{r_{rm}-r}{nR_0}\right)\right]\right\} \qquad (5.50)$$

The resultant magnitude of velocity along the direction of frictional shear stress during rotary sinter-forging is expressed in equation (5.30). Hence, substituting equations (5.38) and (5.39) into equation (5.30), one get:

$$\left|\left(U_r^2+U_\theta^2\right)^{1/2}\right|_{z=h_i} = \begin{Bmatrix}\left[\frac{(1-2\eta)\beta e^{-\beta}r^2\omega\sin\alpha}{(1+\eta)\left(1-e^{-\beta}\right)h_i}\right]\\ \left[\left(\frac{1+\cos P\theta}{2}\right)^2+\left(\frac{\sin P\theta}{P}\right)\right]^{1/2}\end{Bmatrix} \qquad (5.51)$$

Substituting equations (5.50) and (5.51) into equation (5.49), solving and simplifying, the frictional shear energy dissipation may be expressed as:

$$W_f = \left[\frac{(1-2\eta)\mu\beta e^{-\beta}\omega h_i^{\,3}\sin\alpha}{40(1+\eta)\left(1-e^{-\beta}\right)P^3\tan^4\alpha}\right]\left\{\begin{Bmatrix}\left[P_{av}+\rho_0\varphi_0\left(1-\frac{r_{cm}}{nR_0}\right)\right]\\ \left(\tan^5\frac{\pi P}{2}+\frac{5}{3}\tan^3\frac{\pi P}{2}+1\right)\end{Bmatrix}\right.$$
$$\left.+\left\{\begin{Bmatrix}\left(\frac{\rho_0\varphi_0 h_i}{80R_0\tan\alpha}\right)\\ \left[\tan^5\frac{\pi P}{2}+\frac{5\left(1+8P^2\right)}{3}\tan^3\frac{\pi P}{2}\right.\\ \left.+40P^2\tan\frac{P\pi}{2}+\frac{8}{3}\left(1+5P^2\right)\right]\end{Bmatrix}\right\}\right\} \qquad (5.52)$$

The total power dissipations may be computed by substituting equations (5.48) and (5.52) into equation (5.24) and average forging load during rotary phase of rotary sinter-forging may be computed by below equation:

$$F_r = J\left(R_0\omega\right)^{-1} A_{av} \qquad (5.53)$$

The dynamic effects, *i.e.* effect of die velocity on the relative magnitudes of various energy dissipations and average die load involved during rotary sinter-forging of axi-symmetrical preform has been illustrated using concepts of inertia factor 'ξ' (Refer Equation 3.28) and load factor 'ζ' (Refer Equation 3.29) as discussed in the previous sections.

5.4 PARAMETRIC RESULTS & DISCUSSION

To illustrate the dynamic effects during rotary sinter-forging of axi-symmetric preforms, a typical data of preform and various deformation characteristics compatible with corresponding experimental work has been considered as follows:
R_0 = 15 mm; H_0 = 10 mm; $\rho_0\phi_0$ = 0.30 P_{av}; σ_0 = 6.25 kg/mm^2; ρ_i = 2 × 10^3 kg/m^3; β = 0.35; n = 2; α = 5^0, 10^0, 15^0, 20^0, 25^0 and 30^0; μ = 0.30 (high interfacial friction) and 0.05 (low interfacial friction); U = 0.001 to 0.1 m/sec; ω = 1.0 to 60.0 rad/sec and h_i = 0.25 to 2.5 mm.

Figures 5.4 shows variation of indentation load with skew contact angle of upper conical die and indentation depth for different die velocity during rotary sinter-forging of axi-symmetric preforms. It is evident

that indentation loads are lower for higher skew contact angles and axial die velocity of upper conical die. The higher skew contact angle means lower apex angle of upper conical die and hence, lower contact area between die and preform surface. The smaller contact deforming surface area between die and workpiece during rotary sinter-forging results into lower indentation loads for the same die pressure. Thus, load requirements during rotary sinter-forging are considerably low, as compared to conventional flat die sinter-forging operations. Also, the indentation loads are lower for higher axial die velocity due to dynamic effects, *i.e.* shorter deformation contact times for rotary sinter-forging process, especially at higher die velocities.

It has been indicated in figure 2.16 of chapter 2 that indented contact area generated on preform top surface increases with increase in die load and this is also shown in figure 5.5. The figure shows the experimental and theoretical variations of average indentation load with indentation depth for different die velocity. It is clearly observed that indentation load increases with indentation depth, as higher loads are required to penetrate the preform top surface. Also, the indentation loads are lower for higher axial die velocity of upper conical die, whose justification has been discussed with the previous figure.

Figure 5.6 shows the variation of inertia factor *'ξ'* with angular die velocity of upper conical die for different skew contact angles and indentation depths during rotary sinter-forging of axi-symmetric preforms. It is evident from the figure that inertia factor increases exponentially with angular die velocity indicating that inertia energy dissipations is relatively high and comparable to internal and frictional shear energy dissipations during mechanical processing of sintered materials at higher die velocities. Also, the higher skew contact angle of upper conical die and lower indentation depth results into lower inertia energy dissipations due to smaller conical indented contact areas generated over preform top surfaces.

The variation of load factor *'ζ'* with angular die velocity of upper conical die during rotary sinter-forging of axi-symmetric preforms is shown in figure 5.7. It can be observed that die load decreases with increase in angular velocity of upper conical die *i.e.* dynamic effects are predominant at higher deformation speeds, as compared with that at rotary sinter-forging at slower speed due to smaller contact times under loads. The short forging times results into decrease in resistance of preform material against deformation and hence lower die loads.

Figures 5.8 shows the variation of height reduction with angular velocity of upper conical die for different average rotary load during rotary sinter-forging of axi-symmetric preforms. It can be seen that reduction in height increases rapidly with the angular die velocity and then remains fairly constant. Also, it is higher for higher rotary loads and initial indentation depths. Figure 5.9 shows the variation of average rotary load with skew contact angle of the upper conical die for different angular velocities during rotary sinter-forging of axi-symmetric preforms. It is evident from the figure that rotary loads are lower for higher skew contact angle and lower indentation depth indicating that load requirements with upper conical die having smaller cone angle is comparatively low as compared that with higher cone angle during rotary sinter-forging process.

The final rotary forging loads also decreases with increase in angular velocity of die. This appears to be mainly of two prominent consequences. First, rotary sinter-forging, especially at higher die velocity is characterized by very small deformation contact time resulting into restriction of heat dissipation at die-preform interface and thus, reduction in the resistance of preform material against deformation. Second, the rotary sinter-forging produces an additional horizontal component of circumferential stress due to rotation or dynamic effects of upper conical die, which not only creates conditions necessary for better metal flow, but also reduces the net resultant stress required for deformation of sintered material. This effect also increases with angular velocity of upper conical die. This confirms the advantage of high load reduction offered by the rotary sinter-forging with conical dies over that of conventional flat-die sinter-forging operations. Also, the experimental data are in close agreement with theoretical ones and thus, confirms the validity of the present theoretical *'Upper Bound'* analysis.

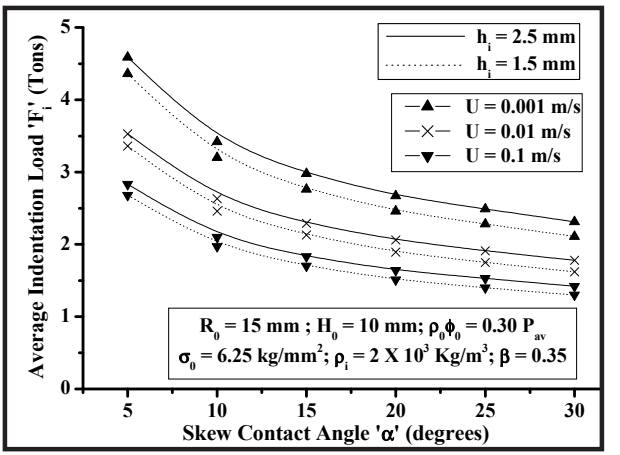

Figure 5.4: Variation of average indentation load with skew contact angle of upper conical die during rotary sinter-forging.

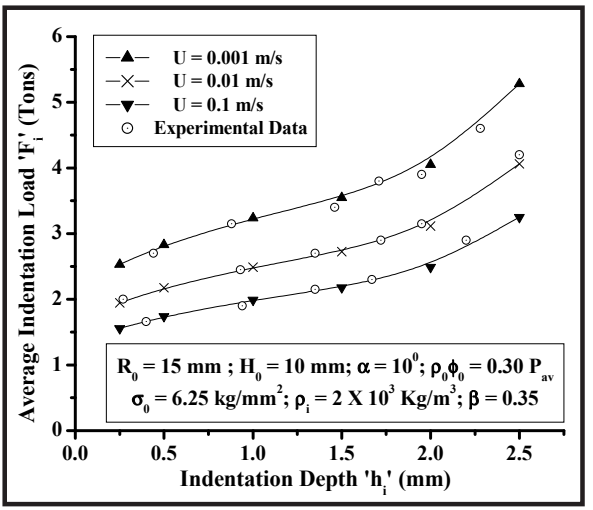

Figure 5.5: Variation of average indentation load with indentation depth during rotary sinter-forging.

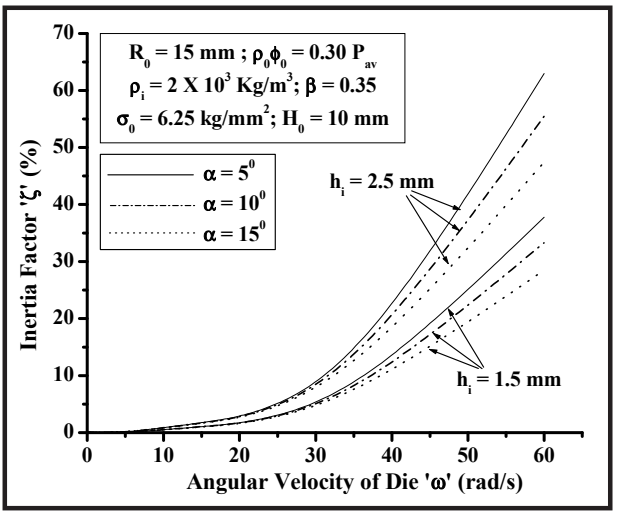

Figure 5.6: Variation of inertia factor with angular velocity of upper conical die during rotary sinter-forging.

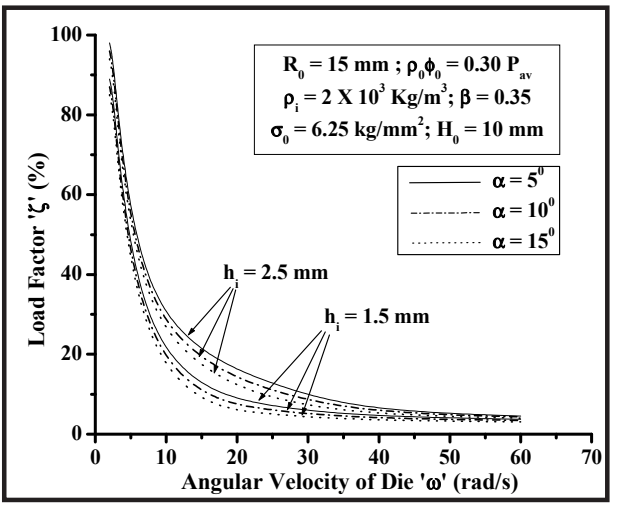

Figure 5.7: Variation of load factor with angular velocity of upper conical die during rotary sinter-forging.

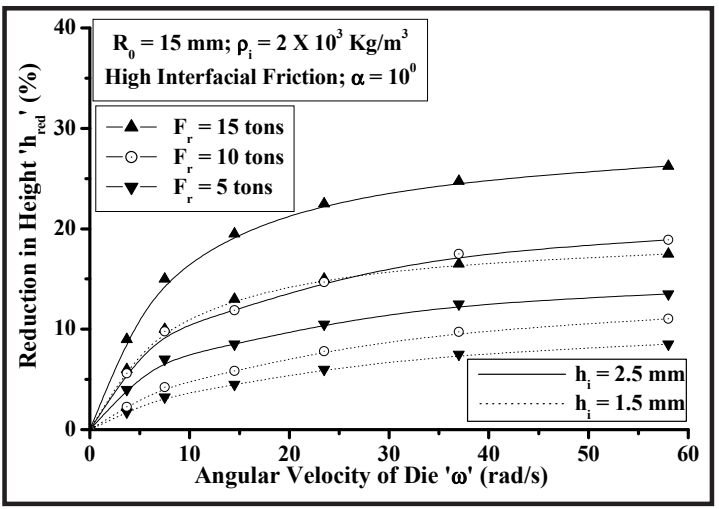

Figure 5.8: Variation of height reduction with angular velocity for different average rotary load during rotary sinter-forging.

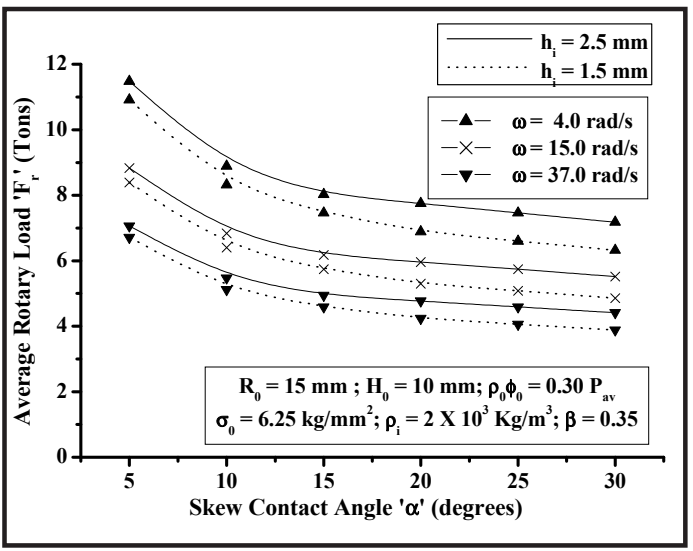

Figure 5.9: Variation of average rotary load with skew contact angle of upper conical die during rotary sinter-forging.

CHAPTER-6
DESIGN OF EXPERIMENT (DOE) APPLICATIONS IN SINTER FORGING

Outline of the Chapter: *6.1 Upper Bound Analysis of Hollow Preform; 6.1.1 Velocity Field & Strain Rates; 6.1.2 Energy Dissipations; 6.2 Design of Experiment (DOE) Analysis; 6.3 Results & Parametric Discussion*

Design of experiment and response surface methodology techniques are the two prominent quality engineering tools, which could be effectively used for analyzing, recognizing and setting of main controlling factors to particular levels, such that the load requirements during sinter-forging processes are minimized and process performance can be optimized. A very little work has been reported for application of these tools in material processing area. *Antony et al. [1997, 1998]* gave a review of statistical design of experiments techniques and reported its applications for improving the process quality using several case studies. *Derringer & Suich [1980] & Hambli [2002]* gave design of experiment-based analysis for simultaneous optimisation of several response variables during sheet metal blanking processes. *Hill et al. [1966]* gave a review of response surface methodology techniques and *Doloi et al. [2003]* successfully applied it for parametric analysis of electrochemical discharge machining process.

The present chapter demonstrates the application of DOE (Design of Experiment) and RSM (Response Surface Methodology) techniques for the analysis of dynamic effects during mechanical processing of sintered materials. To illustrate this, open-die sinter-forging of hollow metal powder preform has been considered assuming bulging of vertical sides of preform and no circumferential flow of sides. The expressions for internal, frictional and inertia energy dissipations have been established based on exponential velocity field and strain rates and a concept of inertia and load factors has been introduced for investigation of the associated dynamic effects during sinter-forging operation. Further, DOE and RSM analysis has been done for both the inertia and load factors respectively.

The analysis considered four *'Factors', i.e.* shape-complexity factor, barreling parameter, initial relative density of preform and die velocity and two *'Response Variables', i.e.* inertia factor and load factor. The DOE technique considered for present analysis is 2^n full-factorial randomized design, so that the complete effect of factors on the response variables could be studied. The *'Interaction Effects', i.e.* factor combinations, which highly influence the *'Response Variables'* has been identified and their values for optimal sinter-forging conditions has been found. During RSM analysis, the multiple linear regression equations of second order has been formulated based on various interaction effects. Finally, these *'Interaction Effects'* between various *'Factors'* has been plotted as three-dimensional graphs using MATLAB software.

6.1 UPPER BOUND ANALYSIS OF HOLLOW PREFORM

The analysis of open-die sinter-forging of hollow disc preform considers one additional assumption apart from the common assumptions. It states that at neutral radius or section, the radial velocity in the deforming hollow disc preform is zero. The direction of frictional shear stress during sinter-forging will necessarily depend upon the direction of material flow. The direction of material flow in solid preforms is radially outwards throughout, but in hollow disc preforms, the direction of material flow will not be always outwards everywhere. In fact, it will depend upon the interfacial friction conditions, which actually decides the position of neutral radius. Thus, two flow conditions arise due to the position of neutral radius during open-die sinter-forging of hollow disc preform. During first flow condition, the interfacial friction is high and neutral radius lies within the inner radius, *i.e.* $r_{hn} < r_{hi}$ and the flow of metal is outwards throughout the deforming hollow disc preform. During second flow condition, the interfacial condition is low and the neutral radius lies in-between the inner and outer radii *i.e.* $r_{hi} \leq r_{hn} \leq r_{h0}$. In this case, the metal will flow inwards for region $r_{hi} \leq r \leq r_{hn}$ and outwards for region $r_{hn} \leq r \leq r_{h0}$ *[Agrawal, 1999]*. The above two conditions are dealt separately in the present analysis, as energy dissipation due to frictional shear stress will be different in both the cases due to difference in the metal flow behavior [Refer Figures 6.1 (a) & (b)].

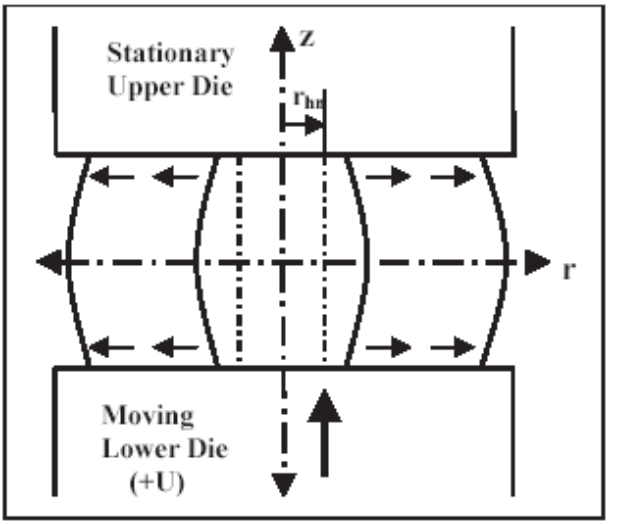

Figure 6.1 (a): Metal flow for case I ($r_{hi} \geq r_{hn}$), *i.e.* metal is flowing outwards everywhere.

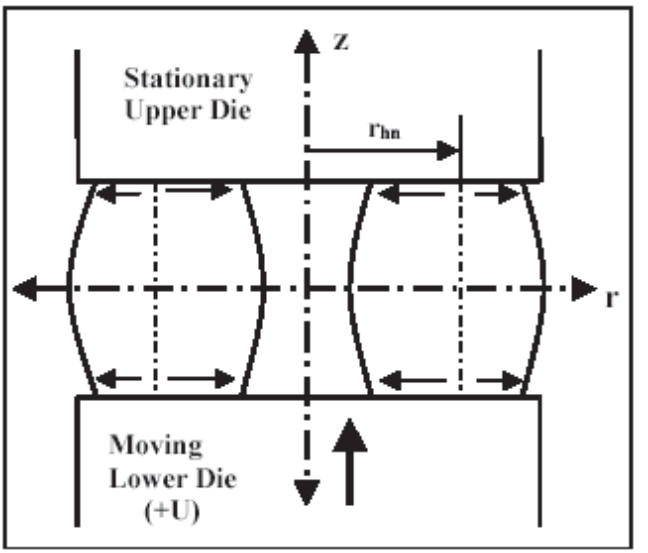

Figure 6.1 (b): Metal flow for case II ($r_{h0} \geq r_{hn} \geq r_{hi}$), *i.e.* metal is flowing inwards for $r_{hn} \geq r \geq r_{hi}$ and outwards for $r_{h0} \geq r \geq r_{hn}$.

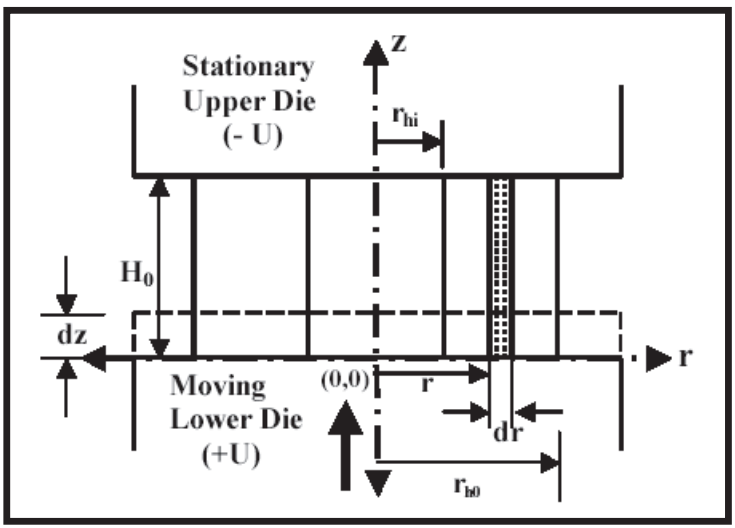

Figure 6.2: Schematic diagram of open-die sinter-forging of axi - symmetric hollow disc preform.

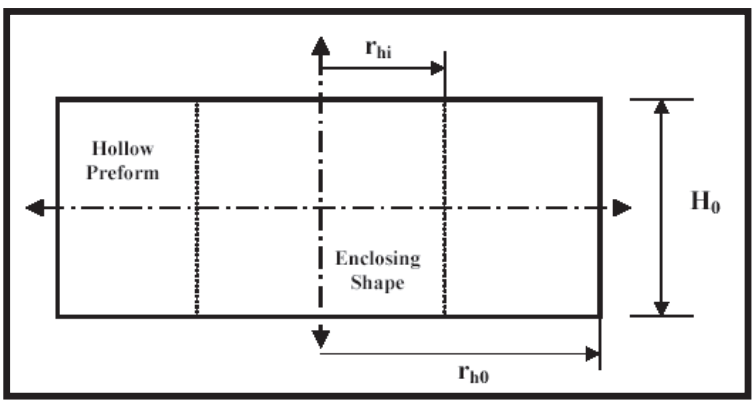

Figure 6.3: Shape-complexity factor for hollow disc preform.

6.1.1 Velocity Field & Strain Rates

Consider open-die sinter-forging of a hollow disc preform between two perfectly flat, parallel and rigid die platens with lower die platen moving upwards with velocity *'U'* and upper die platen being stationary as shown in figure 6.2. The compatibility equation [Refer Equation A.9] and boundary conditions are given as:

$$\dot{\varepsilon}_{rr} + \dot{\varepsilon}_{\theta\theta} + \left(\frac{1-2\eta}{1+\eta}\right)\dot{\varepsilon}_{zz} = 0$$

$$U_z = U \quad \text{at} \quad z = 0 \tag{6.1}$$
$$U_z = 0 \quad \text{at} \quad z = H_0 \tag{6.2}$$
$$U_r = 0 \quad \text{at} \quad r = r_n \tag{6.3}$$

The velocity field and strain rates satisfying equations (A.9), (6.1), (6.2) and (6.3) are given as [Refer Appendix F]:

$$U_r = \left[\frac{(1-2\eta)}{2(1+\eta)}\right]\left[\frac{\beta e^{-\beta z/H_0} Ur}{(1-e^{-\beta})H_0}\right]\left[1-\left(\frac{r_{hn}}{r}\right)^2\right] \tag{6.4}$$

$$U_z = -\left[\frac{e^{-\beta} - e^{-\beta z/H_0}}{1-e^{-\beta}}\right]U \tag{6.5}$$

$$U_\theta = 0 \tag{6.6}$$

$$\dot{\varepsilon}_{rr} = \left[\frac{(1-2\eta)}{2(1+\eta)}\right]\left[\frac{\beta e^{-\beta z/H_0} U}{(1-e^{-\beta})H_0}\right]\left[1+\left(\frac{r_{hn}}{r}\right)^2\right] \tag{6.7}$$

$$\dot{\varepsilon}_{zz} = -\left[\frac{\beta e^{-\beta z/H_0} U}{(1-e^{-\beta})H_0}\right] \tag{6.8}$$

$$\dot{\varepsilon}_{\theta\theta} = \left[\frac{(1-2\eta)}{2(1+\eta)}\right]\left[\frac{\beta e^{-\beta z/H_0} U}{(1-e^{-\beta})H_0}\right]\left[1-\left(\frac{r_{hn}}{r}\right)^2\right] \tag{6.9}$$

$$\dot{\varepsilon}_{rz} = -\left[\frac{(1-2\eta)\beta^2 e^{-\beta z/H_0} Ur}{4(1+\eta)(1-e^{-\beta})H_0^{\,2}}\right]\left[1-\left(\frac{r_{hn}}{r}\right)^2\right] \tag{6.10}$$

$$\dot{\varepsilon}_{r\theta} = \dot{\varepsilon}_{\theta z} = 0 \tag{6.11}$$

6.1.2 Energy Dissipations

The total external energy *'J'* supplied by the die platens during plastic deformation using *'Upper Bound'* approach is given as in equation (5.11). The internal energy dissipation *'W_i'* during open-die sinter-forging of hollow disc preform is given as:

$$W_i = \left(\frac{2\sigma_0}{\sqrt{3}}\right)\int_V \left(\sqrt{\frac{1}{2}\dot{\varepsilon}_{ij}\dot{\varepsilon}_{ij}}\right) dV$$

$$= \left(\frac{2\sigma_0}{\sqrt{3}}\right)\int_{z=0}^{z=H_0}\int_{r=r_{hi}}^{r=r_{ho}} \left[\frac{\dot{\varepsilon}_{rr}^2 + \dot{\varepsilon}_{zz}^2 + \dot{\varepsilon}_{\theta\theta}^2 + \dot{\varepsilon}_{rz}^2}{2}\right](2\pi r dr dz) \qquad (6.12)$$

Substituting equations (6.7) to (6.11) above, solving and simplifying, the internal energy dissipation may be expressed as:

$$W_i = \left[\frac{2\pi\sigma_0(1-2\eta)(r_{ho}-r_{hi})^2 U}{\sqrt{3}(1+\eta)}\right]\left[2 + \frac{4(1+\eta)^2}{(1-2\eta)^2} - \frac{\beta^2\left(r_{h0}^2 + r_{hi}^2 + r_{h0}r_{hi} - 12r_{hn}^2\right)}{24H_0^2} - \frac{\beta^2 r_{hn}^4}{8H_0^2(r_{h0}-r_{hi})^2} + \frac{r_{hn}^4}{3(r_{h0}-r_{hi})\left(r_{h0}^3 - r_{hi}^3\right)}\right] \qquad (6.13)$$

The frictional shear energy dissipation at die-workpiece interface *'W_f'* is given as:

$$W_f = \int_S (\tau_\pm)|\Delta U| dS \qquad (6.14)$$

The frictional shear stress (assuming pressure term equal to average pressure) during sinter-forging of hollow disc preform at z = *'0'* and *'H_0'* is given as [refer equation 4.5].

$$\tau_\pm = \mu\left[p_{av} + \rho_0\varphi_0\left\{1 - \frac{r_{hm} \pm (r_{hn} - r)}{n r_{h0}}\right\}\right] \qquad (6.15)$$

The positive and negative signs signify that metal is flowing outwards and inwards respectively. Thus, as discussed earlier in the present section, there will be two cases of metal flow according to the position of neutral radius due to two different interfacial friction conditions, which are discussed below separately.

<u>Case I: ($r_{hn} < r_{hi}$)</u>, *i.e.* when metal is flowing outwards throughout the preform.

The frictional shear energy dissipation during open-die sinter-forging of hollow disc preform for the present flow condition may be expressed as:

$$W_{f_I} = \int_{r=r_{hi}}^{r=r_{h0}} (\tau_+)|U_r|_{z=o}(2\pi r dr) + \int_{r=r_{hi}}^{r=r_{h0}} (\tau_+)|U_r|_{z=H_0}(2\pi r dr)$$

From equation (6.4), the radial velocity at z = 0 and z = H_0 respectively are given as:

$$\left|U_r\right|_{z=0} = \left[\frac{(1-2\eta)\beta U r}{2(1+\eta)\left(1-e^{-\beta}\right)H_0}\right]\left[1-\left(\frac{r_{hn}}{r}\right)^2\right] \tag{6.17}$$

$$\left|U_r\right|_{z=H_0} = \left[\frac{(1-2\eta)\beta e^{-\beta} U r}{2(1+\eta)\left(1-e^{-\beta}\right)H_0}\right]\left[1-\left(\frac{r_{hn}}{r}\right)^2\right] \tag{6.18}$$

Substituting equations (6.15), (6.17) and (6.18) into equation (6.16), solving and simplifying, the frictional shear energy dissipation may be expressed as:

$$W_{f_I} = \left[\frac{\pi\mu\beta(1-2\eta)\left(1+e^{-\beta}\right)\left(r_{h0}-r_{hi}\right)U}{3(1+\eta)\left(1-e^{-\beta}\right)H_0}\right]\left\{\begin{array}{l}\left\{\left[P_{av}+\rho_0\varphi_0\left(1-\frac{r_{hm}+r_{hn}}{nr_{h0}}\right)\right]\right\} \\ \left(r_{h0}^2+r_{hi}^2+r_{h0}r_{hi}-3r_{hn}^2\right)\end{array}\right\} + \left[\frac{3\rho_0\varphi_0\left(r_{h0}+r_{hi}\right)\left(r_{h0}^2+r_{hi}^2-2r_{hn}^2\right)}{4nr_{h0}}\right] \tag{6.19}$$

<u>Case II: ($r_{hi} \le r_{hn} \le r_{ho}$)</u>, i.e. when metal is flowing inwards in the region bounded by r_{hi} and r_{hn} and flowing outwards in the region bounded by r_{hn} and r_{h0} in preform.

The frictional shear energy dissipation during open-die sinter-forging of hollow disc preform for the present flow condition may be expressed as:

$$W_{f_{II}} = \left[\begin{array}{l}\int_{r=r_{hi}}^{r=r_{hn}}(\tau_-)\left|U_r\right|_{z=0}(2\pi r dr)+\int_{r=r_{hn}}^{r=r_{h0}}(\tau_+)\left|U_r\right|_{z=0}(2\pi r dr) \\ +\int_{r=r_{hi}}^{r=r_{hn}}(\tau_-)\left|U_r\right|_{z=H_0}(2\pi r dr)+\int_{r=r_{hn}}^{r=r_{h0}}(\tau_+)\left|U_r\right|_{z=H_0}(2\pi r dr)\end{array}\right] \tag{6.20}$$

Substituting equations (6.15), (6.17) and (6.18) into equation (6.19), solving and simplifying, the frictional shear energy dissipation may be expressed as:

$$W_{f_{II}}=\left[\frac{\pi\mu\beta(1-2\eta)\left(1+e^{-\beta}\right)U}{3(1+\eta)\left(1-e^{-\beta}\right)H_0}\right]\left\{\begin{array}{l}\left\{\left[P_{av}+\rho_0\varphi_0\left(1-\frac{r_{hm}}{nr_{h0}}\right)\right]\right.\\\left.\left[\left(r_{h0}-r_{hn}\right)^2\left(r_{h0}+2r_{hn}\right)+\left(r_{hn}-r_{hi}\right)^2\left(r_{hn}+2r_{hi}\right)\right]\right\}\\-\left(\frac{\rho_0\varphi_0 r_{hn}}{nr_{h0}}\right)\left[\begin{array}{l}\left(r_{h0}-r_{hn}\right)^2\left(r_{h0}+2r_{hn}\right)\\-\left(r_{hn}-r_{hi}\right)^2\left(r_{hn}+2r_{hi}\right)\end{array}\right]\\+\left(\frac{3\rho_0\varphi_0}{4nr_{h0}}\right)\left[\begin{array}{l}\left(r_{h0}-r_{hn}\right)^2\left(r_{h0}+r_{hn}\right)^2\\-\left(r_{hn}-r_{hi}\right)^2\left(r_{hn}+r_{hi}\right)^2\end{array}\right]\end{array}\right\}\quad(6.21)$$

The energy dissipation due to inertia forces 'W_a' is given as:

$$W_a=\int_V\rho_i a_i U_i dV=\int_{z=0}^{Z=H_0}\int_{r=r_{hi}}^{r=r_{h0}}\rho_i\left(a_r U_r+a_z U_z\right)\left(2\pi r dr dz\right)$$

Substituting equations (6.4) and (6.5) into equations (5.20) and (5.21) and simplifying one gets:

$$\left(a_r U_r+a_z U_z\right)=\left\{\begin{array}{l}\left[\frac{(1-2\eta)\beta e^{-\beta z/H_0}U}{2(1+\eta)\left(1-e^{-\beta}\right)H_0}\right]^3\left[r^2\left(1-\frac{r_{hn}^2}{r^2}\right)^2\left(1+\frac{r_{hn}^2}{r^2}\right)\right]\\+\left[\frac{(1-2\eta)\beta e^{-\beta z/H_0}Ur}{2(1+\eta)\left(1-e^{-\beta}\right)H_0}\right]^2\left[\frac{\beta\left(e^{-\beta}-e^{-\beta z/H_0}\right)U}{\left(1-e^{-\beta}\right)H_0}\right]\left[1-\frac{r_{hn}^2}{r^2}\right]^2\\-\left[\frac{\left(e^{-\beta}-e^{-\beta z/H_0}\right)^2\beta e^{-\beta z/H_0}U^3}{\left(1-e^{-\beta}\right)^3H_0}\right]+U\dot{U}\end{array}\right\}\quad(6.23)$$

Substituting equation (6.23) into equation (6.22), solving and simplifying, the energy dissipation due to inertia forces may be expressed as:

$$W_a=\left[\frac{\pi\rho_i\beta^2\left(r_{h0}^2-r_{hi}^2\right)U^3}{3H_0^2}\right]\left\{\begin{array}{l}\left\{\left[\frac{(1-2\eta)^3\left(1-e^{-3\beta}\right)}{8(1+\eta)^3\left(1-e^{-\beta}\right)^3}\right]\right.\\\left.\left[\left(\frac{r_{h0}^2+r_{hi}^2}{2}\right)+\left(\frac{2r_{hn}^4}{r_{h0}^2-r_{hi}^2}\right)\ln\left|\frac{r_{h0}}{r_{hi}}\right|+\left(\frac{r_{hn}^6}{r_{h0}^2r_{hi}^2}\right)-r_{hn}^2\right]\right\}\\-\left\{\left[\frac{(1-2\eta)^2\left(2+e^{-\beta}\right)H_0}{4(1+\eta)^2\left(1-e^{-\beta}\right)}\right]\right.\\\left.\left[\left(\frac{r_{h0}^3-r_{hi}^3}{r_{h0}^2-r_{hi}^2}\right)-\left(\frac{2r_{hn}^2}{r_{h0}+r_{hi}}\right)-\frac{r_{hn}^4}{r_{h0}r_{hi}\left(r_{h0}+r_{hi}\right)}\right]\right\}\\-\left\{\left(\frac{H_o^2}{\beta^2}\right)\left[1-e^{-\beta}-\frac{3\dot{U}H_0}{U^2}\right]\right\}\end{array}\right\}\quad(6.24)$$

To study the shape variation effects during sinter-forging of axi-symmetric hollow disc preform, a concept of shape-complexity factor is introduced, which is defined as the ratio of outer to inner radius of hollow disc preform [Refer Figure 6.3]. The value of the factor is always greater than one and tends to infinity, when shape of hollow disc preform approaches to that of an enclosing solid disc, *i.e.* $r_{hi} \approx 0$.

$$C_p = \left[\frac{r_{h0}}{r_{hi}} \right] \tag{6.25}$$

The dynamic or inertia effects, *i.e.* effect of die velocity on relative magnitudes of various energy dissipations and average die load involved during open-die sinter-forging of hollow disc preform is illustrated using concepts of inertia factor *'ξ'* (Refer Equation 3.28) and load factor 'ζ' (Refer Equation 3.29) as discussed in the previous chapter.

6.2 DESIGN OF EXPERIMENT (DOE) ANALAYSIS

In order to study and identify the interrelationships among important process variables and their effect on dynamic effects and other related deformation characteristics during mechanical processing of sintered materials, especially at higher die velocities, 2^n full-factorial DOE (Design of Experiment) and RSM (Response Surface Methodology) techniques has been employed in the present research work. The analysis considers four *'Factors'*, each at two levels *i.e.* low and high levels during open-die sinter-forging of hollow disc preform *e.g.* shape-complexity factor *'C_p'*, barreling parameter *'β'*, initial relative density *'ρ_0'* and die velocity *'U'*, which are represented as *'A'*, *'B'*, *'C'* and *'D'* respectively as shown in the table 6.1. The inertia factor *'ξ'* and load factor *'ζ'* has been considered as *'Response Variables'*.

Table 6.2 shows various combinations of factors known as *'Factor Treatments'* with the corresponding values of response variables *i.e.* inertia and load factors and *'Run Order'* considered during experimentation. The positive and negative signs of factor treatments indicate high and low levels of factors respectively. The *'Run Orders'* are codes in which the alphabets represent factors, which are at high level in a particular *'Factor Treatment'*. The values of response variables have been multiplied with the coefficients of standard *'Orthogonal Contrast Coefficient Table'* for 2^4 full-factorial experimental design (refer table G.1 in appendix G) and corresponding values of *'Average Coefficient of Factor Effect Estimate'*, *'Sum of Squares'* and *'Percent Contribution'* for each experiment run have been obtained using standard formulae *[Montgomery, 1976]*. Tables 6.3 (a)

and (b) shows the values of *'Average Coefficient of Factor Effect Estimate'*, *'Sum of Squares'* and *'Percent Contribution'* for inertia factor and load factor respectively.

Table 6.1: Factor levels for 2^4 full-factorial design during open-die sinter-forging of hollow disc preform.

Factors	Factor Description	Factor Levels	
		Low	High
A	Shape Complexity Factor (C_p)	1.2	2.0
B	Barreling parameter (β)	0.20	0.40
C	Initial relative density (ρ_0)	0.70	0.90
D	Die Velocity (U)	0.01 m/s	10 m/s

Table 6.2: Factor treatments, response variable values and run order for 2^4 full-factorial designs during open-die sinter-forging of hollow disc preform.

Sl. No.	Factor Treatments				Response Variables		Run Order
	A	B	C	D	ξ (%)	ζ (%)	
1	-	-	-	-	00.046	36.414	**1**
2	+	-	-	-	00.361	56.852	**a**
3	-	+	-	-	00.052	43.445	**b**
4	+	+	-	-	00.385	67.545	**ab**
5	-	-	+	-	00.090	50.444	**c**
6	+	-	+	-	00.547	78.766	**ac**
7	-	+	+	-	00.099	59.382	**bc**
8	+	+	+	-	00.590	82.784	**abc**
9	-	-	-	+	03.934	0.703	**d**
10	+	-	-	+	19.693	1.097	**ad**
11	-	+	-	+	04.166	1.009	**bd**
12	+	+	-	+	20.828	1.455	**abd**
13	-	-	+	+	05.708	0.979	**cd**
14	+	-	+	+	28.539	1.528	**acd**
15	-	+	+	+	06.130	1.140	**bcd**
16	+	+	+	+	30.652	1.623	**abcd**

Table 6.3 (a): Factor effect estimate of inertia factor for 2^4 full-factorial designs during open-die sinter-forging of hollow disc preform.

Factorial Effect	Average Factor-Effect Estimate Coefficient	Sum of Squares	Percent Contribution
A	1.02 E+01	4.14 E+02	2.36 E+01
B	4.98 E-01	9.92 E-01	5.66 E-02
AB	3.31 E-01	4.38 E-01	2.50 E-02
C	2.86 E+00	3.27 E+01	1.87 E+00
AC	1.90 E+00	1.45 E+01	8.28 E-01
BC	1.49 E-01	8.87 E-02	5.06 E-03
ABC	1.01 E-01	4.04 E-02	2.31 E-03
D	1.47 E+01	8.63 E+02	4.92 E+01
AD	**9.77 E+00**	**3.82 E+02**	**2.18 E+01**
BD	4.78 E-01	9.12 E-01	5.21 E-02
ABD	1.01 E-01	4.04 E-02	2.31 E-03
CD	**2.74 E+00**	**3.00 E+01**	**1.72 E+00**
ACD	1.83 E+00	1.34 E+01	7.64 E-01
BCD	1.43 E-01	8.19 E-02	4.68 E-03
ABCD	9.65 E-02	3.72 E-02	2.12 E-03

Table 6.3 (b): Factor effect estimate of load factor for 2^4 full-factorial designs during open-die sinter-forging of hollow disc preform.

Factorial Effect	Average Factor-Effect Estimate Coefficient	Sum of Squares	Percent Contribution
A	1.23E+01	6.02E+02	3.90E+00
B	3.95E+00	6.24E+01	4.04E-01
AB	-1.59E-01	1.01E-01	6.55E-04
C	8.52E+00	2.90E+02	1.88E+00
AC	9.22E-01	3.40E+00	2.20E-02
BC	-6.47E-01	1.67E+00	1.08E-02
ABC	1.09E+00	4.73E+00	3.06E-02
D	-5.83E+01	1.36E+04	8.79E+01
AD	**-1.18E+01**	**5.57E+02**	**3.61E+00**
BD	-3.72E+00	5.54E+01	3.58E-01
ABD	-1.09E+00	4.73E+00	3.06E-02

CD	-8.26E+00	2.73E+02	1.77E+00
ACD	-8.74E-01	3.06E+00	1.98E-02
BCD	5.45E-01	1.19E+00	7.69E-03
ABCD	1.06E+00	4.48E+00	2.90E-02

It is clear from the tables 6.3 (a) and (b) that interaction effects *'AD'* and *'CD'* are high for both inertia and load factors. This indicates that die velocity in combination with shape-complexity factor and initial relative density are of significant importance during open-die sinter-forging of hollow disc preforms, especially at higher deformation speeds. Further, these interactions have been investigated using *'Response Surface Methodology'* technique and multiple linear regression equations of second order depicting the interactions have been formulated mathematically [refer appendix G]. Subsequently, three-dimensional graphs have been generated for each regression equations using MATLAB software [161]. The regression equations for interactions *'AD'* and *'CD'* for inertia factor are given as:

$$\left|Y_{ad}\right|_{inertiafactor} = \begin{bmatrix} 6.273 - 90.156A - 2.012D - 90.682A^2 \\ +0.142D^2 + 26.6AD - 0.802A^2D^2 \end{bmatrix} \quad (6.26)$$

$$\left|Y_{cd}\right|_{inertiafactor} = \begin{bmatrix} 5.602 - 3.807C - 2.148D - 13.737C^2 \\ +0.565D^2 - 0.592CD - 0.06C^2D^2 \end{bmatrix} \quad (6.27)$$

The regression equations for interactions *'AD'* and *'CD'* for load factor are given as:

$$\left|Y_{ad}\right|_{loadfactor} = \begin{bmatrix} 73.217 + 15.409A - 1.001D + 0.665A^2 \\ -0.878D^2 + 3.088AD - 0.363A^2D^2 \end{bmatrix} \quad (6.28)$$

$$\left|Y_{cd}\right|_{loadfactor} = \begin{bmatrix} 78.251 - 51.59C - 2.273D + 74.907C^2 \\ +0.3741D^2 - 14.468CD - 0.285C^2D^2 \end{bmatrix} \quad (6.29)$$

6.3 RESULTS & PARAMETRIC DISCUSSION

To investigate the dynamic effects using DOE and RSM techniques during sinter-forging of axi-symmetric hollow disc preforms, a typical data of preform and deformation characteristics have been considered as follows:

r_{h0} = 12 mm; H_0 = 10 mm; r_{hm} = 7.0 mm; r_{hn} = 8.0 mm; $\rho_0\phi_0 = 0.30\ P_{av}$; σ_0 = 8.25 kg/mm^2; $\rho_i = 7 \times 10^3$ kg/m^3; n = 2; μ = 0.30 (high interfacial friction), β =0.20 to 0.40; C_p = 1.2 to 2.0 and U = 0.01 to 10 m/sec.

Figures 6.4 (a) and (b) shows interaction effects *'A-D'* and *'C-D'* respectively on inertia factor during open-die sinter-forging of hollow disc preform as three-dimensional response surfaces. It is evident from the figures that inertia factor increases with shape-complexity factor, relative density and die velocity. It indicates that as the die velocity, shape-complexity factor and relative density of preform increases, the inertia energy dissipation, as a fraction percent of total energy supplied by die platens also increases. Thus, at high-speed deformation, the energy dissipated in the form of inertia forces is almost comparable with those of internal and frictional shear energy dissipations and hence, must be considered during analysis for the accurate prediction of die loads. From figures, it is also evident that interaction effect *'A-D'* is almost linear, whereas interaction effect *'C-D'* is non-linear with respect to inertia factor.

The interaction effects *'A-D'* and *'C-D'* on load factor are shown in figures 6.5 (a) and (b) respectively. It is clearly apparent that load factor decreases with die velocity, whereas it increases with shape-complexity factor and preform relative density. The effect of interaction *'A-D'* on load factor is nonlinear, whereas effect of interaction *'C-D'* is linear. Hence, dynamic effects *i.e.* effect of die velocity in combination with preform relative density and shape-complexity factor produces nonlinear effects, in case of inertia and load factors respectively. Thus, it can be concluded that die velocity is the most critical deformation characteristics during mechanical processing of sintered materials, whose effect on inertia energy dissipation and average die load becomes pronounced at higher values. Finally, it is expected that the present techniques used for the analysis of dynamic effects during mechanical processing of sintered materials will be highly useful for the researchers to identify and optimize the deformation processes.

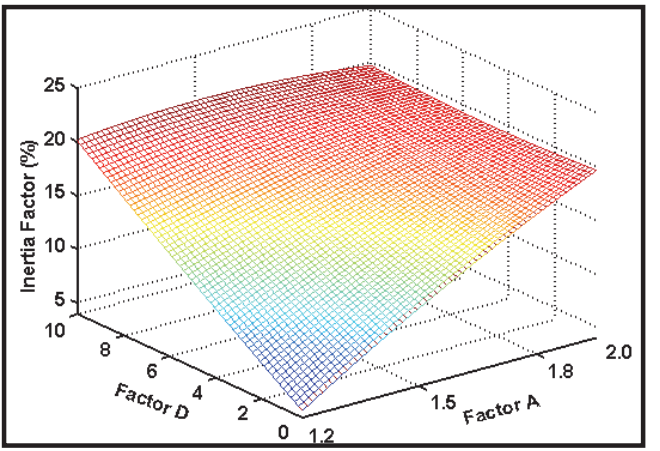

Figure 6.4 (a): Interaction effect of factors *'A'* and *'D'* on inertia factor during open-die sinter-forging of hollow disc preform.

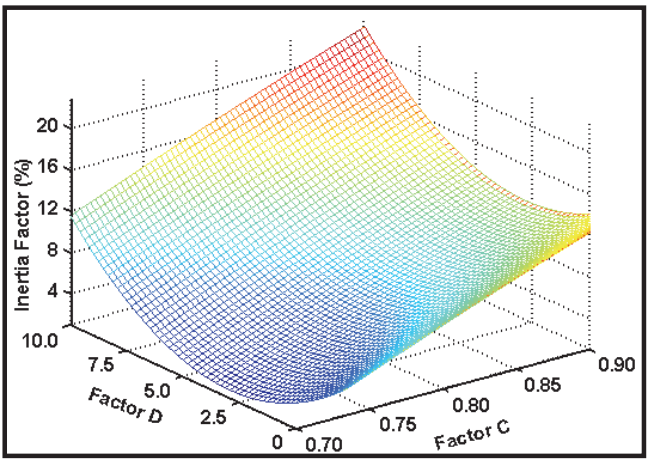

Figure 6.4 (b): Interaction effect of factors *'C'* and *'D'* on inertia factor during open-die sinter-forging of hollow disc preform.

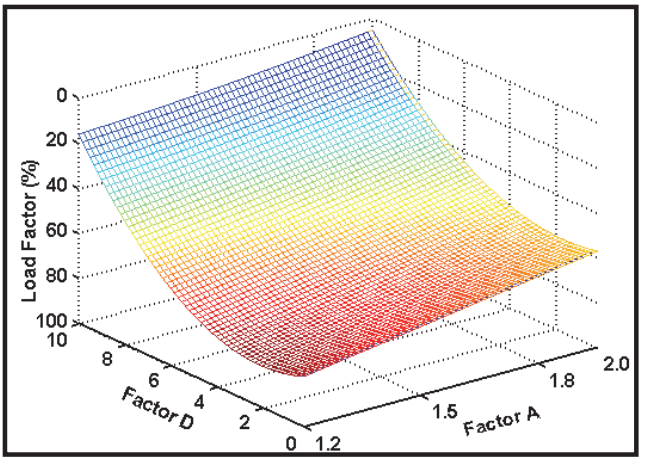

Figure 6.5 (a): Interaction effect of factors *'A'* and *'D'* on load factor during sinter-forging of hollow disc preform.

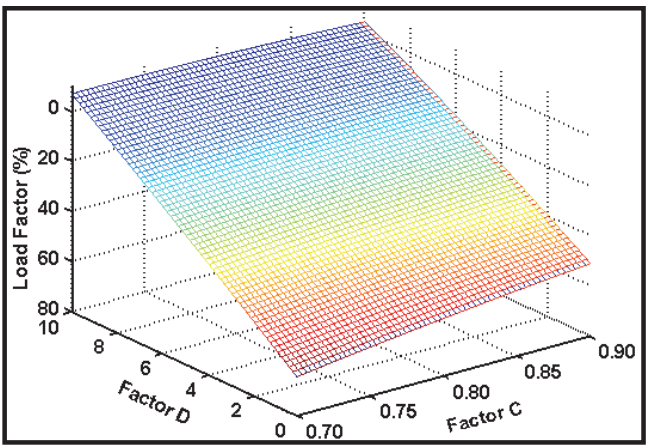

Figure 6.5 (b): Interaction effect of factors *'C'* and *'D'* on load factor during sinter-forging of hollow disc preform.

APPENDIX A

The principal strain increments during sinter-forging of metal powder preforms according to Tabata & Masaki (Refer Chapter-1) is given as:

$$d\varepsilon_{ii} = \left\{ d\lambda \left[\frac{3(\sigma_{ii} - \sigma_m)}{2\sqrt{3}J_2'} \pm \eta \right] \right\} (i = 1,2,3) \tag{1.20}$$

where:

$$d\lambda = \left\{ \frac{\sqrt{2}}{3} \left[(d\varepsilon_{11} - d\varepsilon_{22})^2 + (d\varepsilon_{22} - d\varepsilon_{33})^2 + (d\varepsilon_{33} - d\varepsilon_{11})^2 \right]^{1/2} \right\} \tag{A.1}$$

$$J_2' = \left[\frac{(\sigma_{11} - \sigma_{22})^2 + (\sigma_{22} - \sigma_{33})^2 + (\sigma_{33} - \sigma_{11})^2}{6} \right] \tag{A.2}$$

$$\sigma_m = \left(\frac{\sigma_{11} + \sigma_{22} + \sigma_{33}}{3} \right) \tag{A.3}$$

$$\eta = \left[0.54(1 - \rho_r)^{1.2} \right] \tag{A.4}$$

(for compressive hydrostatic stress component)

The volumetric strain increment is given as:

$$d\varepsilon_v = (d\varepsilon_{11} + d\varepsilon_{22} + d\varepsilon_{33}) \tag{A.5}$$

Substituting equations (A.1) to (A.4) and (4.20) into equation (A.5), one gets:

$$d\varepsilon_v = \begin{bmatrix} \mp(3\eta d\lambda) \\ = \mp \left\{ \sqrt{2}\eta \left[(d\varepsilon_{11} - d\varepsilon_{22})^2 + (d\varepsilon_{22} - d\varepsilon_{33})^2 + (d\varepsilon_{33} - d\varepsilon_{11})^2 \right]^{1/2} \right\} \end{bmatrix} \tag{A.6}$$

The state of strain during axi-symmetric sinter-forging of metal powder preforms is given as follows:

$$\varepsilon_{11} = \varepsilon_{33} = \varepsilon_{rr} = \varepsilon_{\theta\theta} \;\&\; \varepsilon_{22} = \varepsilon_{zz} \tag{A.7}$$

Hence, the strain increments during axi-symmetric sinter-forging of metal powder preforms from equations (A.6) & (A.7) are given as follows:

$$d\varepsilon_{rr} = \left(\tfrac{1}{2} - \eta \right) d\lambda \,,\; d\varepsilon_{\theta\theta} = \left(\tfrac{1}{2} - \eta \right) d\lambda$$

$$\&\; d\varepsilon_{zz} = -(1 + \eta) d\lambda \tag{A.8}$$

Substituting equations (A.8) into equation (A.6) and rearranging, the compatibility equation during axi-symmetric sinter-forging of metal powder preforms is given as:

$$\dot{\varepsilon}_{rr} + \dot{\varepsilon}_{\theta\theta} + \left(\frac{1-2\eta}{1+\eta}\right)\dot{\varepsilon}_{zz} = 0 \qquad \text{(A.9)}$$

Also, the state of strain during plane-strain sinter-forging of metal powder preforms is given as follows:

$$\varepsilon_{11} = \varepsilon_{xx}\,,\ \varepsilon_{22} = \varepsilon_{yy}\ \ \&\ \ \varepsilon_{33} = \varepsilon_{zz} = \left(\frac{\varepsilon_{xx} + \varepsilon_{yy}}{2}\right) \qquad \text{(A.10)}$$

Hence, the strain increments during plane-strain sinter-forging of metal powder preforms from equations (A.6) and (A.10) are given as follows:

$$d\varepsilon_{xx} = \left(\frac{3}{2} - \eta\right)d\lambda\ ;\ d\varepsilon_{yy} = -\left(\frac{3}{2} + \eta\right)d\lambda$$

$$\&\ \ d\varepsilon_{zz} = -\eta\, d\lambda \qquad \text{(A.11)}$$

Substituting equations (A.11) into equation (A.10) and rearranging, the compatibility equation during plane strain sinter-forging of metal powder preform is given as:

$$\dot{\varepsilon}_{xx} + \left[\frac{\left(1 + 2\eta^2 - 2\eta\sqrt{3\left(1-\eta^2\right)}\right)}{\left(1-4\eta^2\right)}\right]\dot{\varepsilon}_{yy} = 0 \qquad \text{(A.12)}$$

APPENDIX B

Assuming radial velocity *'U_r'* in a deforming axi-symmetric truncated conical preforms to vary with following parameters:

a) increases with increase in radial distance.
b) decreases exponentially with increase in vertical distance.
c) increases with increase in barreling parameter.
d) increases with increase in die velocity.

The velocity along *'θ'* direction, *i.e.* circumferential velocity is zero, as there is no rotation of preform during open-die sinter-forging operation. The axial velocity along vertical direction is assumed to be a function of radial distance *'r'* and vertical distance *'z'*.

Therefore, velocity field and strain rates for axi-symmetric truncated conical preforms may be expressed as:

$$U_r = \left(K_1 \beta e^{-\beta z/H_0} Ur\right) \quad \text{(B.1)}$$

$$U_\theta = 0 \quad \text{(B.2)}$$

$$U_z = f(r,z) \quad \text{(B.3)}$$

$$\dot{\varepsilon}_{rr} = \frac{\partial U_r}{\partial r} = \left(K_1 \beta e^{-\beta z/H_0} U\right) \quad \text{(B.4)}$$

$$\dot{\varepsilon}_{\theta\theta} = \frac{U_r}{r} = \left(K_1 \beta e^{-\beta z/H_0} U\right) \quad \text{(B.5)}$$

$$\dot{\varepsilon}_{zz} = \frac{\partial U_z}{\partial z} = \frac{\partial f(r,z)}{\partial z} \quad \text{(B.6)}$$

The compatibility equation during axi-symmetric sinter-forging of metal powder preform is given as [Refer Appendix A]:

$$\dot{\varepsilon}_{rr} + \dot{\varepsilon}_{\theta\theta} + \left(\frac{1-2\eta}{1+\eta}\right)\dot{\varepsilon}_{zz} = 0$$

Substituting equations (B.4) to (B.6) into above equation and solving, one get:

$$U_z = \left\{\left[\frac{2(1+\eta)}{1-2\eta}\right]\left(K_1 e^{-\beta z/H_0} UH_0\right) + K_2\right\} \quad \text{(B.7)}$$

where, K_1 and K_2 are constants of integration.

The boundary conditions are given as [Refer Equations 3.1 & 3.2]:

$U_z = U$ at $z = 0$

$U_z = 0 \quad \text{at} \quad z = H_0$

Substituting boundary conditions into equations (B.7), the constants of proportionality are given as:

$$K_1 = \left[\frac{1-2\eta}{2(1+\eta)\left(1-e^{-\beta}\right)H_0}\right] \;\&\; K_2 = -\left(\frac{e^{-\beta}U}{1-e^{-\beta}}\right) \tag{B.8}$$

Substituting equation (B.8) into equations (B.7), the axial vertical velocity is given as:

$$U_z = -\left[\frac{\left(e^{-\beta} - e^{-\beta z/H_0}\right)U}{1-e^{-\beta}}\right] \tag{B.9}$$

Substituting equation (B.9) into equations (B.1) to (B.6), the velocity field & strain rates during open-die sinter-forging of axi-symmetric truncated conical preform are given as:

$$U_r = \left[\frac{(1-2\eta)\beta e^{-\beta z/H_0}Ur}{2(1+\eta)\left(1-e^{-\beta}\right)H_0}\right] \tag{B.10}$$

$$U_z = -\left[\frac{\left(e^{-\beta} - e^{-\beta z/H_0}\right)U}{1-e^{-\beta}}\right] \tag{B.11}$$

$$U_\theta = 0 \tag{B.12}$$

$$\dot{\varepsilon}_{rr} = \frac{\partial U_r}{\partial r} = \left[\frac{(1-2\eta)\beta e^{-\beta z/H_0}U}{2(1+\eta)\left(1-e^{-\beta}\right)H_0}\right] \tag{B.13}$$

$$\dot{\varepsilon}_{zz} = \frac{\partial U_z}{\partial z} = -\left[\frac{\beta e^{-\beta z/H_0}U}{\left(1-e^{-\beta}\right)H_0}\right] \tag{B.14}$$

$$\dot{\varepsilon}_{\theta\theta} = \frac{U_r}{r} = \left[\frac{(1-2\eta)\beta e^{-\beta z/H_0}U}{2(1+\eta)\left(1-e^{-\beta}\right)H_0}\right] \tag{B.15}$$

$$\dot{\varepsilon}_{rz} = \frac{1}{2}\left(\frac{\partial U_r}{\partial z} + \frac{\partial U_z}{\partial r}\right) = -\left[\frac{(1-2\eta)\beta^2 e^{-\beta z/H_0}Ur}{4(1+\eta)\left(1-e^{-\beta}\right)H_0^2}\right] \tag{B.16}$$

$$\dot{\varepsilon}_{r\theta} = \dot{\varepsilon}_{\theta z} = 0 \tag{B.17}$$

APPENDIX C

Assuming that axial velocity *'U_x'* in a deforming preform under plane-strain condition varies with following parameters:

a) increases with increase in axial distance.
b) decreases exponentially with increase in vertical distance.
c) increases with increase in barreling parameter.
d) increases with increase in die velocity.

The lateral velocity along *'y'* direction is zero, as there is no rotation of preform during open-die sinter-forging operation. The velocity along vertical direction is assumed to be a function of axial distance *'x'* and vertical distance *'z'*. Therefore, velocity field for plane-strain preform may be expressed as:

$$U_x = K_1 \beta e^{-\beta z/H_0} Ux \qquad (C.1)$$

$$U_y = 0 \qquad (C.2)$$

$$U_z = f(x,z) \qquad (C.3)$$

The compatibility equation during plane-strain sinter-forging of metal powder preform is given as [Refer Appendix A]:

$$\dot{\varepsilon}_{xx} + \left[\frac{(1+2\eta^2) - 2\eta\sqrt{3(1-\eta^2)}}{(1-4\eta^2)} \right] \dot{\varepsilon}_{zz} = 0$$

Substituting equations (C.1) to (C.3) into above equation and integrating, one gets:

$$U_z = \left\{ \left[\frac{1-4\eta^2}{(1+2\eta^2) - 2\eta\sqrt{3(1-\eta^2)}} \right] K_1 H_0 e^{-\beta z/H_0} U + K_2 \right\} \qquad (C.4)$$

where, K_1 and K_2 are constants of integration.

Thus, strain rates during open-die sinter-forging of plane-strain preforms are given as:

$$\dot{\varepsilon}_{xx} = \frac{\partial U_x}{\partial x} = \left(K_1 \beta e^{-\beta z/H_0} U \right) \qquad (C.5)$$

$$\dot{\varepsilon}_{yy} = 0 \qquad (C.6)$$

$$\dot{\varepsilon}_{zz} = \frac{\partial U_z}{\partial z} = \frac{\partial f(x,z)}{\partial z} \qquad (C.7)$$

The boundary conditions are given as [Refer Equations 3.33 & 3.34]:

$U_z = U$ at $z = 0$

$U_z = 0$ at $z = H_0$

Substituting boundary conditions into equations (C.4), the constants of proportionality are given as:

$$K_1 = \left[\frac{(1+2\eta^2)-2\eta\sqrt{3(1-\eta^2)}}{\left(1-4\eta^2\right)\left(1-e^{-\beta}\right)H_0}\right] \;\&\; K_2 = -\left(\frac{e^{-\beta}U}{1-e^{-\beta}}\right) \tag{C.8}$$

Substituting equation (C.8) into equations (C.4), the axial vertical velocity is given as:

$$U_z = -\left[\frac{\left(e^{-\beta}-e^{-\beta z/H_0}\right)U}{1-e^{-\beta}}\right] \tag{C.9}$$

Differentiating the above equation, the axial vertical strain rate is given as:

$$\dot{\varepsilon}_{zz} = \frac{\partial U_z}{\partial z} = -\left[\frac{\beta e^{-\beta z/H_0}U}{\left(1-e^{-\beta}\right)H_0}\right] \tag{C.10}$$

Substituting equation (C.10) into compatibility equation, strain rate along x-axis is given as follows:

$$\dot{\varepsilon}_{xx} = \left\{\frac{\left[(1+2\eta^2)-2\eta\sqrt{3(1-\eta^2)}\right]\beta e^{-\beta z/H_0}U}{\left(1-4\eta^2\right)\left(1-e^{-\beta}\right)H_0}\right\} \tag{C.11}$$

Integrating above equation, the velocity along x-axis is given as:

$$U_x = \left\{\frac{\left[(1+2\eta^2)-2\eta\sqrt{3(1-\eta^2)}\right]\beta e^{-\beta z/H_0}Ux}{\left(1-4\eta^2\right)\left(1-e^{-\beta}\right)H_0}\right\}$$

Therefore, velocity field & strain rates during open-die sinter-forging of plane-strain preforms are given as:

$$U_x = \left[\frac{\chi\beta e^{-\beta z/H_0}Ux}{(1-e^{-\beta})H_0}\right] \tag{C.12}$$

$$U_z = -\left[\frac{\left(e^{-\beta}-e^{-\beta z/H_0}\right)U}{1-e^{-\beta}}\right] \tag{C.13}$$

$$U_y = 0 \tag{C.14}$$

$$\dot{\varepsilon}_{xx} = \frac{\partial U_x}{\partial x} = \left[\frac{\chi\beta e^{-\beta z/H_0}Ux}{\left(1-e^{-\beta}\right)H_0}\right] \tag{C.15}$$

$$\dot{\varepsilon}_{zz} = \frac{\partial U_z}{\partial z} = -\left[\frac{\beta e^{-\beta z/H_0} U}{\left(1-e^{-\beta}\right) H_0}\right] \tag{C.16}$$

$$\dot{\varepsilon}_{yy} = 0 \tag{C.17}$$

$$\dot{\varepsilon}_{xz} = \frac{1}{2}\left(\frac{\partial U_x}{\partial z} + \frac{\partial U_z}{\partial x}\right) = -\left[\frac{\chi \beta^2 e^{-\beta z/H_0} Ux}{2\left(1-e^{-\beta}\right) H_0^2}\right] \tag{C.18}$$

$$\dot{\varepsilon}_{xy} = \dot{\varepsilon}_{yz} = 0 \tag{C.19}$$

where, $\chi = \left[\frac{1+2\eta^2 - 2\eta\sqrt{3\left(1-\eta^2\right)}}{\left(1-4\eta^2\right)}\right]$

APPENDIX D

Assuming radial velocity *'U_r'* in a deforming axi-symmetric cylindrical preform within closed dies to vary with following parameters:

a) increases with increase in radial distance.
b) decreases with increase in vertical distance.
c) increases with increase in die velocity.

The circumferential velocity along *'θ'* direction is assumed to be zero and axial velocity along vertical direction is assumed to be a function of radial distance *'r'* and vertical distance *'z'*. Therefore, velocity field and strain rates during closed-die sinter-forging of axi-symmetric cylindrical preform may be expressed as:

$$U_r = \left(\frac{K_1 U r}{H_0}\right) \tag{D.1}$$

$$U_z = f(r,z) \tag{D.2}$$

$$U_\theta = 0 \tag{D.3}$$

$$\dot{\varepsilon}_{rr} = \frac{\partial U_r}{\partial r} = \left(\frac{K_1 U}{H_0^{'}}\right) \tag{D.4}$$

$$\dot{\varepsilon}_{zz} = \frac{\partial U_z}{\partial z} = \frac{\partial f(r,z)}{\partial z} \tag{D.5}$$

$$\dot{\varepsilon}_{\theta\theta} = \frac{U_r}{r} = \left(\frac{K_1 U}{H_0^{'}}\right) \tag{D.6}$$

The compatibility equation during axi-symmetric sinter-forging of metal powder preform is given as [refer appendix A]:

$$\dot{\varepsilon}_{rr} + \dot{\varepsilon}_{\theta\theta} + \left(\frac{1-2\eta}{1+\eta}\right)\dot{\varepsilon}_{zz} = 0$$

Substituting equations (D.4) to (D.6) into above equation and solving, one gets:

$$U_z = -\left(\frac{2K_1 U z}{H_0^{'}}\right) + K_2 \tag{D.7}$$

where, K_1 and K_2 are constants of integration.
The boundary conditions are given as [Refer Equations 4.2 and 4.3]:

$U_z = 0$ at $z = 0$
$U_z = -U$ at $z = H^{/}_0$

Substituting boundary conditions into equations (D.7), the constants of proportionality are given as:

$$K_1 = \frac{1}{2} \text{ and } K_2 = 0 \tag{D.8}$$

Substituting equation (D.8) into equations (D.7), the axial vertical velocity is given as:

$$U_z = -\left(\frac{Uz}{H_0'}\right) \tag{D.9}$$

Substituting equation (D.9) into equations (D.1) to (D.6), the velocity field & strain rates during open-die sinter-forging of axi-symmetric cylindrical preform are given as:

$$U_r = \left[\frac{(1-2\eta)Ur}{2(1+\eta)h}\right] \tag{D.10}$$

$$U_z = -\left(\frac{Uz}{h}\right) \tag{D.11}$$

$$U_\theta = 0 \tag{D.12}$$

$$\dot{\varepsilon}_{rr} = \left[\frac{(1-2\eta)U}{2(1+\eta)h}\right] \tag{D.13}$$

$$\dot{\varepsilon}_{zz} = -\left(\frac{U}{h}\right) \tag{D.14}$$

$$\dot{\varepsilon}_{\theta\theta} = \left[\frac{(1-2\eta)U}{2(1+\eta)h}\right] \tag{D.15}$$

$$\dot{\varepsilon}_{r\theta} = \dot{\varepsilon}_{\theta z} = \dot{\varepsilon}_{rz} = 0 \tag{D.16}$$

APPENDIX E

Assuming axial velocity *'U_x'* in the deforming axi-symmetric preform during indentation phase of sinter rotary-forging is assumed to vary with following parameters:

a) increases with increase in radial distance.
b) decreases exponentially with increase in vertical distance.
c) increases with increase in barreling parameter.
d) increases with increase in die velocity.

Therefore, axial velocity and strain rate are given as:

$$U_Z = \left[K_1 \beta e^{-\beta z / h_i} U + K_2 \right] \tag{E.1}$$

$$\dot{\varepsilon}_{zz} = -\left(\frac{K_1 \beta^2 e^{-\beta z / h_i} U}{h_i} \right) \tag{E.2}$$

The boundary conditions are given as [Refer Equations 5.12 & 5.13]:

$U_z = 0$ at $z = 0$

$U_z = -U$ at $z = h_i$

Substituting boundary conditions into equations (E.1), the constants of proportionality are given as:

$$K_1 = \left[\frac{1}{\beta(1 - e^{-\beta})} \right] \;\&\; K_2 = -\left(\frac{U}{1 - e^{-\beta}} \right) \tag{E.3}$$

Substituting equation (E.3) into equations (E.1) & (E.2), the axial vertical velocity and strain rate are given as:

$$U_z = -\left[\frac{1 - e^{-\beta z / h_i}}{1 - e^{-\beta}} \right] U \tag{E.4}$$

$$\dot{\varepsilon}_{zz} = \left[\frac{-\beta e^{-\beta z / h_i} U}{(1 - e^{-\beta}) h_i} \right] \tag{E.5}$$

The flow conditions during sinter rotary-forging suggest that circumferential flow of material takes place, *i.e.* $U_\theta \neq 0$ along with radial flow. Also, radial flow is not uniform throughout the circumference of indented area and is accompanied with vertical bulging of preform sides. It is maximum at the center of horizontal symmetry axis of indented area and gradually decreases towards its

ends and is zero at the ends. Therefore, radial velocity and strain rate are given as:

$$U_r = \left[K_3 U e^{-\beta z / h_i} (1 + \cos P\theta) r \right] \quad \text{(E.6)}$$

$$\dot{\varepsilon}_{rr} = \left[K_3 U e^{-\beta z / h_i} (1 + \cos P\theta) \right] \quad \text{(E.7)}$$

where, $P = \left(\frac{\pi}{2\alpha} \right)$

The compatibility equation during axi-symmetric sinter-forging of metal powder preform is given as [Refer Appendix A]:

$$\dot{\varepsilon}_{rr} + \dot{\varepsilon}_{\theta\theta} + \left(\frac{1-2\eta}{1+\eta} \right) \dot{\varepsilon}_{zz} = 0$$

Rearranging the above equation, one gets:

$$\frac{\partial U_r}{\partial r} + \frac{U_r}{r} + \frac{1}{r} \frac{\partial U_\theta}{\partial \theta} = \left(\frac{2\eta - 1}{1+\eta} \right) \dot{\varepsilon}_z \quad \text{(E.8)}$$

Substituting equations (E.4) & (E.6) into equation (E.8), rearranging and integrating, the circumferential velocity is given as:

$$U_\theta = \left\{ \left[\frac{(1-2\eta)\beta e^{-\beta z / h_i} U \theta r}{(1+\eta)(1-e^{-\beta}) h_i} \right] - \left(2K_3 U e^{-\beta z / h_i} r \right) \left(\theta + \frac{\sin P\theta}{P} \right) + K_4 \right\} \quad \text{(E.9)}$$

Neglecting the higher order terms, the above equation may be expressed as:

$$U_\theta = \left\{ \left[\frac{(1-2\eta)\beta e^{-\beta z / h_i} U \theta r}{(1+\eta)(1-e^{-\beta}) h_i} \right] - \left(2K_3 U e^{-\beta z / h_i} \theta r \right) + K_4 \right\} \quad \text{(E.10)}$$

The boundary condition for circumferential velocity during indentation phase of sinter rotary-forging [Refer Equations 5.37] is given as:
$U_\theta = 0$ at $r = 0$ & $\theta = \alpha$.

Substituting boundary condition into equation (E.10), the constants of proportionality are given as:

$$K_3 = \left[\frac{(1-2\eta)\beta}{2(1+\eta)\left(1-e^{-\beta}\right) h_i} \right] \text{ \& } K_4 = 0 \quad \text{(E.11)}$$

The radial and circumferential velocities may be formulated by substituting equation (E.11) into equations (E.7) & (E.9) respectively.

Therefore, the velocity field and strain rate during indentation phase of sinter rotary-forging are given as:

$$U_r = \left[\frac{(1-2\eta)\beta e^{-\beta z/h_i} Ur(1+\cos P\theta)}{2(1+\eta)(1-e^{-\beta})h_i}\right] \tag{E.12}$$

$$U_\theta = -\left[\frac{(1-2\eta)\beta e^{-\beta z/h_i} Ur\sin P\theta}{(1+\eta)P(1-e^{-\beta})h_i}\right] \tag{E.13}$$

$$U_z = -\left[\frac{1-e^{-\beta z/H_o}}{1-e^{-\beta}}\right]U \tag{E.14}$$

$$\dot{\varepsilon}_{rr} = \frac{\partial U_r}{\partial r} = \left[\frac{(1-2\eta)\beta e^{-\beta z/h_i} U(1+\cos P\theta)}{2(1+\eta)(1-e^{-\beta})h_i}\right] \tag{E.15}$$

$$\dot{\varepsilon}_{\theta\theta} = \left(\frac{U_r}{r} + \frac{1}{r}\frac{\partial U_\theta}{\partial \theta}\right) = \left[\frac{(1-2\eta)\beta e^{-\beta z/h_i} U(1-\cos P\theta)}{1-2\eta(1-e^{-\beta})h_i}\right] \tag{E.16}$$

$$\dot{\varepsilon}_{zz} = \frac{\partial U_z}{\partial z} = -\left[\frac{\beta e^{-\beta z/H_o} U}{(1-e^{-\beta})h_i}\right] \tag{E.17}$$

$$\dot{\varepsilon}_{r\theta} = \frac{1}{2}\left[\frac{1}{r}\frac{\partial U_r}{\partial \theta} + \frac{\partial U_\theta}{\partial r} - \frac{U_\theta}{r}\right] = -\left[\frac{(1-2\eta)\beta e^{-\beta z/h_i} UP\sin P\theta}{4(1+\eta)(1-e^{-\beta})h_i}\right] \tag{E.18}$$

$$\dot{\varepsilon}_{\theta z} = \frac{1}{2}\left[\frac{\partial U_\theta}{\partial z} + \frac{1}{r}\frac{\partial U_z}{\partial r}\right] = \left[\frac{(1-2\eta)\beta^2 e^{-\beta z/h_i} Ur\sin P\theta}{(1+\eta)P(1-e^{-\beta})h_i^{\,2}}\right] \tag{E.19}$$

$$\dot{\varepsilon}_{zr} = \frac{1}{2}\left[\frac{\partial U_r}{\partial z} + \frac{\partial U_z}{\partial r}\right] = -\left[\frac{(1-2\eta)\beta^2 e^{-\beta z/h_i} Ur(1+\cos P\theta)}{4(1+\eta)(1-e^{-\beta})h_i^{\,2}}\right] \tag{E.20}$$

APPENDIX F

Assuming axial velocity *'U_z'* in a deforming hollow axi-symmetric preform to vary with following parameters:

a) decreases exponentially with increase in axial vertical distance.
b) increases with increase in barreling parameter.
c) increases with increase in die velocity.

The velocity along *'θ'* direction *i.e.* circumferential velocity is zero, as there is no rotation of preform during open-die sinter-forging operation. The radial velocity is assumed to be a function of radial distance *'r'* and axial vertical distance *'z'*. Therefore, velocity field for hollow preform may be expressed as:

$$U_r = f(r,z) \tag{F.1}$$

$$U_\theta = 0 \tag{F.2}$$

$$\left(U_z = K_1 \beta e^{-\beta z/H_0} U + K_2\right) \tag{F.3}$$

where, K_1 and K_2 are a constant of proportionality.

The boundary conditions are given as [Refer Equations 6.1 to 6.3]:

$U_z = U \quad at \quad z = 0;$
$U_z = 0 \quad at \quad z = H_0$
$U_r = 0 \quad at \quad r = r_{hn}$

Substituting boundary conditions into equation (F.3), and solving, the constants of proportionality are given as:

$$K_1 = \left[\frac{1}{\beta\left(1-e^{-\beta}\right)}\right] \;\&\; K_2 = -\left(\frac{e^{-\beta}U}{1-e^{-\beta}}\right) \tag{F.4}$$

Substituting constants of proportionality into equation (F.3), the axial strain rate is given as:

$$U_z = -\left[\frac{\left(e^{-\beta} - e^{-\beta z/H_0}\right)U}{1-e^{-\beta}}\right] \tag{F.5}$$

Thus, strain rates during open-die sinter-forging of hollow preform are given as:

$$\dot{\varepsilon}_{rr} = \frac{\partial U_r}{\partial r} \tag{F.6}$$

$$\dot{\varepsilon}_{\theta\theta} = \frac{U_r}{r} \tag{F.7}$$

$$\dot{\varepsilon}_{zz} = \frac{\partial U_z}{\partial z} = -\left[\frac{\beta e^{-\beta z/H_0} U}{H_0\left(1-e^{-\beta}\right)}\right] \tag{F.8}$$

The compatibility equation during axi-symmetric sinter-forging of metal powder preform is given as [Refer Appendix A]:

$$\dot{\varepsilon}_{rr} + \dot{\varepsilon}_{\theta\theta} + \left(\frac{1-2\eta}{1+\eta}\right)\dot{\varepsilon}_{zz} = 0$$

Substituting equations (F.6) to (F.8) above and rearranging, one gets:

$$\frac{1}{r}\left[\frac{\partial\left(U_r r\right)}{\partial r}\right] = \left(\frac{1-2\eta}{1+\eta}\right)\left[\frac{\beta e^{-\beta z/H_0} U}{H_0\left(1-e^{-\beta}\right)}\right] \tag{F.9}$$

Integrating above equation with respect to *'r'*, and rearranging one gets:

$$U_r = \left\{\left(\frac{1-2\eta}{1+\eta}\right)\left[\frac{\beta e^{-\beta z/H_0} U r}{2H_0\left(1-e^{-\beta}\right)}\right] + \frac{K_3}{r}\right\} \tag{F.10}$$

Substituting boundary conditions above, the constant of proportionality is given as:

$$K_3 = \left[\frac{1-2\eta}{2(1+\eta)}\right]\left[\frac{\beta e^{-\beta z/H_0} U r_{hn}^2}{H_0\left(1-e^{-\beta}\right)}\right] \tag{F.11}$$

Substituting equation (F.11) into equation (F.10), radial velocity is given as:

$$U_r = \left[\frac{(1-2\eta)\beta e^{-\beta z/H_0} U r}{2(1+\eta)\left(1-e^{-\beta}\right)H_0}\right]\left(1-\frac{r_{hn}^2}{r^2}\right) \tag{F.12}$$

Therefore, velocity field and strain rates during open-die sinter-forging of hollow preform are given as:

$$U_r = \left[\frac{(1-2\eta)}{2(1+\eta)}\right]\left[\frac{\beta e^{-\beta z/H_0} U r}{\left(1-e^{-\beta}\right)H_0}\right]\left[1-\left(\frac{r_{hn}}{r}\right)^2\right] \tag{F.13}$$

$$U_z = -\left(\frac{e^{-\beta} - e^{-\beta z/H_0}}{1-e^{-\beta}}\right)U \tag{F.14}$$

$$U_\theta = 0 \tag{F.15}$$

$$\dot{\varepsilon}_{rr} = \left[\frac{(1-2\eta)\beta e^{-\beta z/H_0} U}{2(1+\eta)(1-e^{-\beta})H_0}\right]\left[1+\left(\frac{r_{hn}}{r}\right)^2\right] \quad \text{(F.16)}$$

$$\dot{\varepsilon}_{zz} = \frac{\partial U_z}{\partial z} = -\left[\frac{\beta e^{-\beta z/H_0} U}{(1-e^{-\beta})H_0}\right] \quad \text{(F.17)}$$

$$\dot{\varepsilon}_{\theta\theta} = \left[\frac{(1-2\eta)\beta e^{-\beta z/H_0} U}{2(1+\eta)(1-e^{-\beta})H_0}\right]\left[1-\left(\frac{r_{hn}}{r}\right)^2\right] \quad \text{(F.18)}$$

$$\dot{\varepsilon}_{rz} = -\left[\frac{(1-2\eta)\beta^2 e^{-\beta z/H_0} Ur}{4(1+\eta)(1-e^{-\beta})H_0{}^2}\right]\left[1-\left(\frac{r_{hn}}{r}\right)^2\right] \quad \text{(F.19)}$$

$$\dot{\varepsilon}_{r\theta} = \dot{\varepsilon}_{\theta z} = 0 \quad \text{(F.20)}$$

APPENDIX G

The standard orthogonal contrast coefficient table for 2^4 full-factorial experimental design as considered in the Chapter 6 is given as below:

Table G.1: Standard orthogonal contrast coefficient table for 2^4 full-factorial experimental design.

	A	B	AB	C	AC	BC	ABC	D	AD	BD	ABD	CD	ACD	BCD	ABCD
1	-	-	+	-	+	+	-	-	+	+	-	+	-	-	+
a	+	-	-	-	-	+	+	-	-	+	+	+	+	-	-
b	-	+	-	-	+	-	+	-	+	-	+	+	-	+	-
ab	+	+	+	-	-	-	-	-	-	-	-	+	+	+	+
c	-	-	+	+	-	-	+	-	+	+	+	-	+	+	-
ac	+	-	-	+	+	-	-	-	-	+	-	-	-	+	+
bc	-	+	-	+	-	+	-	-	+	-	-	-	+	-	+
abc	+	+	+	+	+	+	+	-	-	-	+	-	-	-	-
d	-	-	+	-	+	+	-	+	-	-	-	-	+	+	-
ad	+	-	-	-	-	+	+	+	+	-	+	-	-	+	+
bd	-	+	-	-	+	-	+	+	-	+	+	-	+	-	+
abd	+	+	+	-	-	-	-	+	+	+	-	-	-	-	-
cd	-	-	+	+	-	-	+	+	-	-	+	+	-	-	+
acd	+	-	-	+	+	-	-	+	+	-	-	+	+	-	-
bcd	-	+	-	+	-	+	-	+	-	+	-	+	-	+	-
abcd	+	+	+	+	+	+	+	+	+	+	+	+	+	+	+

The multiple linear regression equation of second order in generalized form for analysis of *'Interaction Effect'* between factors *'A'* and *'D'* on *'Inertia Factor'* during open-die sinter-forging of hollow disc preform based on *'Response Surface Methodology'* technique is given as follows:

$$Y = \beta_0 + \beta_1 a + \beta_2 d + \beta_3 a^2 + \beta_4 d^2 + \beta_5 a d + \beta_6 a^2 d^2 \qquad (G.1)$$

The values of inertia factor for possible combinations of two-level factors *'A'* and *'D'* as considered in table 6.2 of chapter 6 is shown below in table G.2.

Table G.2: Inertia factor values for possible combinations of two-level factors *'A'* and *'D'* during sinter-forging of hollow disc preform.

Shape Complexity Factor *'A'*	Die Velocity *'D'* (m/s)	Inertia Factor *'Y'* (%)
1.2	0.01	0.0718
2.0	0.01	0.471
1.2	10	4.985
2.0	10	24.928

The regression equation (G.1) may be expressed in matrix form as follows:

$$Y = X\beta \tag{G.2}$$

Where:

$$X = \begin{matrix} \beta_0 & \beta_1 & \beta_2 & \beta_3 & \beta_4 & \beta_5 & \beta_6 \end{matrix} \begin{bmatrix} 1 & 1.2 & 0.01 & 1.44 & 0.0001 & 0.012 & 0.000144 \\ 1 & 2.0 & 0.01 & 4.0 & 0.0001 & 0.02 & 0.0004 \\ 1 & 1.2 & 10 & 1.44 & 100 & 12.0 & 144.0 \\ 1 & 2.0 & 10 & 4.0 & 100 & 20.0 & 400.0 \end{bmatrix} \tag{G.3}$$

$$Y = \begin{bmatrix} 0.718 \\ 0.471 \\ 4.985 \\ 24.928 \end{bmatrix} \tag{G.4}$$

$$\text{and } \beta = \begin{bmatrix} \beta_0 & \beta_1 & \beta_2 & \beta_3 & \beta_4 & \beta_5 & \beta_6 \end{bmatrix}^T \tag{G.5}$$

The solution of regression equation (G.2) is given as follows:

$$\beta = (X^{/} X)^{-1} X^{/} Y \tag{G.6}$$

Substituting equations (G.3) to (G.5) into equation (G.6) and solving, the coefficients of the multiple linear regression equation of second order is computed as follows:

$$\beta = \begin{bmatrix} 6.273 & -90.156 & -2.012 & -90.682 & 0.142 & 26.60 & -0.802 \end{bmatrix}^T \tag{G.7}$$

Substituting the coefficients from equation (G.7) into equation (G.1), the multiple linear regression equation of second order depicting the interaction effect *'A-D'* on *'Inertia Factor'* during open-die sinter-forging of hollow disc preform is given as follows:

$$\left|Y_{ad}\right|_{\text{inertiafactor}} = 6.273 - 90.156A - 2.012D - 90.682A^2 + 0.142D^2 + 26.6AD - 0.802A^2D^2 \tag{G.8}$$

REFERENCES

Agrawal M. *et al.*, High-speed forging of hollow metal powder preforms, Journal of Production Engineering, I. E. (India), vol. 80 (1999) pp. 8-15.

Akgerman N. & Altan T., Modular analysis of geometry and stresses in closed-die forging: application to a structural part, Transactions of the Journal of Engineering for Industry, ASME, vol. 94, Series B, (November-1972) p. 1025.

Akgerman N. *et al.*, Preform design in closed-die forging, Metallurgia and Metalforming, vol. 26 (May-1973) p. 135.

Akisanya A.R. *et al.*, The yield behavior of metal powders, International Journal of Mechanical Sciences and Engineering, ASME, vol. 39 (1997) p. 1215.

Alexander J.M. *et al.*, On the isostatic compaction and hydrostatic extrusion of iron powder, Proceedings of the 12th International MTDR Conference, Birmingham, UK, 1971, p. 51.

Allen M.M. *et al.*, Application of powder metallurgy to superalloy forging, ASM Source Book on Powder Metallurgy, Compiled by Bradbury S., Ohio, US, 1979, pp. 88-98.

Altan T. & Fiorentino R.J., Prediction of loads and stresses in closed-die forging, Transactions of the Journal of Engineering for Industry, ASME, vol. 93 (May-1971) p. 477.

Altan T. & Henning H.J., Closed-die forging of round shapes flash design and material savings, Metallurgia and Metalforming, vol. 24 (March-1971) p. 83.

Altan T., Computer simulation to predict load, stress and metal flow in an axisymmetric closed-die forging, Metalforming: Interrelation Between Theory and Practice, Edited by Hoffmanner A.L., Plenum Publishing Corporation, 1971, p. 249.

Antes H.W., Powder forging fundamentals, ASM Source Book on Powder Metallurgy, Compiled by Bradbury S., Ohio, US, 1979, pp. 144-160.

Antes H.W., Powder metallurgy hot-formed gears, ASM Source Book on Powder Metallurgy, Compiled by Bradbury S., Ohio, US, 1979, pp. 136-143.

Antes H.W., Present status and potential of powder metallurgy forming, Powder Metallurgy in Defense Technology, vol. 3 (1977) p. 29.

Antony J. *et al.*, Experiments in quality, Manufacturing Engineer, IEE, vol. 76/6 (December-1997) pp. 272-275.

Antony J. *et al.*, Improving the process quality using statistical design of experiments: a case study, Quality Assurance, vol. 6/2 (April-1998) pp. 87-96.

Biner S.B. & Spitzig W.A., Densification of iron compacts with various initial porosities under hydrostatic pressure, Acta. Metall., vol. 38 (1990) pp. 603-610.

Biswas S.K. & Rooks B.W., Application of a computer simulation technique to estimate load and energy in axisymmetric closed die forging, Proceedings of the 12th International MTDR Conference, Birmingham, UK, 1971, p. 371-381.

Borland W. *et al.*, Effect of purity on sintering behavior and properties of iron compacts produced from fine powders, Powder Metallurgy, No. 3 (1980) p. 146.

Brakpool J., The effect of material characteristics on the compaction behavior of metal powders, International Journal of Powder Metallurgy, vol. 48 (1992) p: 423.

Brown G.T. & Jones P.K., Experimental and practical aspects of powder forging process, International Journal of Powder Metallurgy, vol. 6, No. 4 (1970) pp. 29-42.

Brown G.T., Development of alloy system for powder forging, ASM Source Book on Powder Metallurgy, Compiled by Bradbury S., Ohio, US, 1979, p. 474.

Chitkara N.R. & Bhutta M.A., Dynamic heading of triangular, hexagonal, and octagonal shaped heads at high impact velocities: some experiments and an analysis, International Journal Advanced Manufacturing Technology, vol. 18 (2001) pp. 332-347.

Chitkara N.R. & Liaghat G.H., Working pressure, deformation modes and fracture in open-piercing of cylindrical disks made of compacted sintered aluminium powder, International Journal Advanced Manufacturing Technology, vol. 17 (2001) pp. 889-909.

Choi S., Upper-bound analysis of the rotary forging of a cylindrical billet, International Journal of Materials Processing Technology, Elsevier, vol. 67 (1997) pp. 78-82.

Cook J.P., Manganese steels for powder metallurgy hot forming, International Journal of Powder Metallurgy and Powder Technology, vol. 10, No. 1 (1974) p. 345.

Cull G.W., Mechanical and metallurgical properties of powder forging, International Journal of Powder Metallurgy, vol. 13/26 (1970) p. 156.

Davies R. & Mark J.B., The production of components by forging of powder preforms, Proceedings of 13th International MTDR Conference, Birmingham, UK, 1972, p.463.

Dean T.A. *et al.*, Dynamic effects during high-velocity compression testing, Proceedings of the 12th International MTDR Conference, Birmingham, UK, 1971, p. 363-369.

Dean T.A., The influence of billet inertia and dry friction in forging processes-a simple energy approach, Proceedings of the 11th International MTDR Conference, Birmingham, UK, 1970, p. 761.

Derringer G. & Suich R., Simultaneous optimisation of several response variables, Journal of Quality Technology, vol. 12/4 (1980) pp. 214-219.

DeSilva M.G. & Ramesh K.T., The rate-dependent deformation of porous pure iron, International Journal of Plasticity, vol. 13 (1997) p. 587.

Difai M.A., The effect of presintering conditions on the cold forgeability of powder preform, Proceedings of the 15th International MTDR Conference, Birmingham, UK, 1974, p. 651.

Doloi B.N. *et al.*, Response surface methodology based parametric analysis on electrochemical discharge machining of silicon nitride ceramics, Proceedings of 20th AIMTDR, Ranchi, India, (2003) pp: 248-253.

Downey C.L. & Kuhn H.A., Deformation characteristics and plastic theory of sintered powder materials, International Journal of Powder Metallurgy, vol. 7 (1971) pp. 15-21.

Downey C.L. and Kuhn H.A., Designing powder metallurgy preforms for forging axisymmetric parts, ASM Source Book on Powder Metallurgy, Compiled by Bradbury S., Ohio, US, 1979, pp. 129-135.

Dunkley J.J. & Causton R.J., The powder metallurgy extrusion of tool steel bar, International Journal of Powder Metallurgy and Powder Technology, vol. 13, No. 1 (1977).

Elrich U. & Neubert H., Powder forged parts for applications in gearboxes, Metallurgia, vol. 59 (1992) p. 11.

Elwakil S.D. & Davies R., High-speed compaction of metal powders, Proceedings of the 13th International MTDR Conference, Birmingham, UK, 1972, pp. 435-440.

Elwakil S.D., A plane strain analogue for the extrusion of sintered billets, Proceedings of 20th International MTDR Conference, Birmingham, UK, September-1979, p. 229.

Elwakil S.D., Plasticity of sintered iron powder compacts, Proceedings of 15th International MTDR Conference, Birmingham, UK, September-1974, p. 68.

Fereshteh-Saniee F. & Jaafari M., Analytical, numerical and experimental analyses of the closed die forging, International Journal of Materials Processing Technology, Elsevier, vol. 125-126 (2002) p. 334-340.

Fischmeister H.F. *et al.*, Deformation and densification of porous preforms in hot forging, International Journal of Powder Metallurgy, vol. 14, No. 27 (1971) p. 144.

Fischmeister H.F., Powder compaction: fundamentals and recent developments, Proceedings of Institution of Mechanical Engineers, UK, vol. 196 (1982) p. 105.

Forguson B.L. *et al.*, Fatigue of iron base powder metallurgy forgings, Modern Development in Powder Metallurgy, Princeton, vol. 9 (1977) p. 51.

Galanty M. *et al.*, Consolidation of metal powders during the extrusion process, International Journal of Material Processing Technology, Elsevier, vol. 125-126 (2002) pp. 491-496.

Gokler M.I. *et al.*, Analysis of tapered preforms in cold upsetting, International Journal of Machine Tool Design and Research, Pergamon, vol. 39 (1999) pp. 1-16.

Green R.J., A plasticity theory for porous solids, International Journal of Mechanical Sciences and Engineering, ASME, vol. 14 (1971) pp. 215-224.

Griffiths T.J. *et al.*, Compactability equations for the powder forging processes, International Journal of Powder Metallurgy, No. 4 (1976) p. 214.

Hambli R., Design of experiment based analysis for sheet metal blanking processes optimisation, International Journal Advanced Manufacturing Technology, vol. 19 (2002) pp: 403-410.

Hamiuddin M. & Upadhyaya G.S., Effect of molybdenum during sintering of iron and iron phosphorus premix, Powder Metallurgy, No. 3 (1980b) p. 136.

Hamiuddin M. & Upadhyaya G.S., Effect of nickel during sintering of iron containing phosphorus, International Journal of Powder Metallurgy and Powder Technology, vol. 16 (January-1980a) p. 57.

Hayama M., Theoretical analysis of rotary forging of cylindrical rod, Journal of Japan Society for Technology of Plasticity, vol. 24 (1983) pp. 386-393.

Hill W.G. *et al.*, A review of response surface methodology: a literature survey, Technometrics, vol. 8 (1966) pp: 571- 590.

Hilllier M.J., Estimation of dynamic forces in very high speed impact forging, Journal of Engineering for Industry, ASME, vol. 88 (November-1966) pp. 369-372.

Huppmann W.J., The effect of powder characteristics of the sintered forging process, International Journal of Powder Metallurgy, vol. 13, No. 1 (1977) p. 36.

Hwang B. & Kobayashi S., Application of the finite element method to powdered metal compaction processes, International Journal of Machine Tool and Manufacture, Pregamon, vol. 31 (1991) p. 123.

Hwang B. & Kobayashi S., Deformation characterization of powdered metals in compaction, International Journal of Machine Tool and Manufacture, Pregamon, vol. 30 (1990) p. 309.

Ibhadode A.O.A. & Dean T.A., Corner filling characteristics in precision forging, International Journal of Machine Tool Design and Research, Pergamon, vol. 28 (1987) pp. 103-122.

Ibhadode A.O.A. & Dean T.A., The effect of billet location on completely closed cavity die forging, Journal of Mechanical Engineers, vol. 202, No. B-4 (1988) pp. 227-235.

Ibhadode A.O.A. & Dean T.A., The influence of process variables on load and accuracy when forging in a completely closed cavity die, Journal of Mechanical Engineers, vol. 202, No. B-4 (1988) pp. 237-245.

Im Y.T. & Kobayashi S., Analysis of axi-symmetric forging of porous materials by finite element method, Advanced Manufacturing Processes, vol. 1 (1986) p. 473.

Im Y.T. & Kobayashi S., Coupled thermo-viscoplastic analysis in plane-strain compression of porous materials, Advanced Manufacturing Processes, vol. 1 (1986) p. 269.

Im Y.T. & Kobayashi S., Finite element analysis of plastic deformation of porous materials, Metal Forming and Impact Mechanics, Pregamon, (1985) p. 103.

Jain S.C. & Bramley A.N., Characteristics of the high-speed hot forging process, Proceedings of 9th International MTDR Conference, Birmingham, UK, 1968, pp. 95-113.

Jha A.K. *et al.*, Compatibility of sintered materials during cold forging, International Journal of Materials Processing Technology, Elsevier, vol. 9(4/5/6) (1994) pp. 281-299.

Jha A.K. *et al.*, Dynamic effects during high-speed sinter-forging process, International Journal of Machine Tool Design and Research, Pergamon, vol. 36 (1996) p. 1109.

Jha A.K. *et al.*, Forging of metal powder preform, International Journal of Machine Tool Design and Research, Pergamon, vol. 23/4 (1983) p. 201.

Jha A.K. *et al.*, Investigations into the high-speed forgings of sintered copper powder strips, International Journal of Materials Processing Technology, Elsevier, vol. 71 (1997) p. 394.

Jha A.K. *et al.*, Production of sinter-forged components, International Journal of Materials Processing Technology, Elsevier, vol. 41 (1994) pp. 143-169.

Jolgaf M. *et al.*, Development of a CAD/CAM system for the closed-die forging process, International Journal of Materials Processing Technology, Elsevier, vol. 138 (2004) pp. 436-442.

Jones M.G. *et al.*, Estimation of dynamic forces in high-speed compression using a free-flight impact forging device, International Journal of Mechanical Sciences, ASME, vol. 13 (1971) p. 309.

Jones P.K., The technical and economic advantage of powder forged products, International Journal of Powder Metallurgy, vol. 13 (1970) p. 114.

Justino J.G. *et al.*, Constitutive model for the elastic-plastic analysis of porous sintered materials, International Journal of Machine Tools and Manufacture, Elsevier, vol. 44 (2004) pp. 1471-1479.

Kao A. & Koczak M.A., Mixing and compacting behavior of ferrous powders, International Journal of Powder Metallurgy and Powder Technology, vol. 16 (April-1980) p. 105.

Kim H.S., Densification mechanism during hot isostatic pressing of stainless steel powder compacts, International Journal of Material Processing Technology, Elsevier, vol. 123 (2002) pp. 319-322.

Kim J.Y. & Chitkara N.R., Determination of preform shape to improve dimensional accuracy of the forged crown gear form in a closed-die forging process, International Journal of Mechanical Sciences, Pergamon, vol. 43 (2001) pp. 853-870.

Kim K.T. *et al.*, Elastic-plastic responses of porous metals under triaxial loading, International Journal of Solids Structure, vol. 24 (1988) pp. 937-945.

Kim K.T. *et al.*, Elastic-plastic strain hardening responses of porous metals, International Journal of Engineering Sciences, vol. 27 (1989) pp. 767-778.

Kim K.T. *et al.*, Plastic yielding for cold isostatically pressed and sintered porous iron under tension and torsion, International Journal of Powder Metallurgy, vol. 33 (1990) pp. 321-326.

Kim K.T. *et al.*, Strain hardening response of sintered porous iron tubes with various initial porosities under combined tension and torsion, Journal of Engineering Materials and Technology, ASME, vol. 114 (1992) pp. 213-217.

Kiyota F. *et al.*, Densification of powder metallurgy value seat by cold rotary forging, Proceedings of 3rd International Conference on Rotary Metal Working Processes, Japan, 1984, pp. 101-108.

Kobayashi M., Deformation behavior in simultaneous forward-backward extrusion upsetting by rotary forging, Proceedings of 3rd International Conference on Rotary Metal Working Processes, Japan, 1984, pp. 13-22.

Kubo K. & Hirai H., Cold forging of powder preforms by the rotary forging technique, Journal of Japan Society of Technology for Plasticity, vol. 18 (1977) p. 195.

Kubo K. & Hirai H., Sinter-forging by rotary forging press, Proceedings of the 26th Conference of the Japan Society for Technology of Plasticity, 1975, pp. 393-396.

Kubo K. & Hirai H., The preliminary work on rotary forging with an experimental press, Journal of Japan Society for Technology of Plasticity, vol. 15/151 (1973) pp. 648-655.

Kubo K. & Hirai H., Warm rotary forging of thin disc, Proceedings of 3rd International Conference on Rotary Metal Working Processes, Japan, 1984, pp. 31-42.

Kuhn H.A. *et al*., Deformation characteristics of iron powder compacts, Modern Development in Powder Metallurgy, Princeton, vol. 4 (1970) p. 463.

Kumar A. *et al.*, An investigation into product defects in the hot extrusion of aluminium powder preforms, Journal of Mechanical Working Technology, Elsevier, vol. 11 (1985) p. 275.

Kumar K.S. *et al.*, Thermal mechanical processing of iron powder for high compressibility, Proceedings of Europe International Powder Metallurgy Conference, Florence, June-1982, p. 437.

Kumar S., Investigations into tribological aspects during forming of sintered preforms, Proceedings of 2nd International Conference on Industrial Tribology, Hyderabad, India 1999, pp. 324-331.

Kumar S., Principles of metalworking, Oxford, and IBH, New Delhi, 1976.

Kwan C.T., A concave circular parallelepiped element and its applications to three-dimensional closed-die forging, International Journal of Materials Processing Technology, Elsevier, vol. 123 (2002) p. 203-208.

Kwan C.T., An analysis of the closed-die forging of a general non-axisymmetric shape by the upper-bound elemental technique, International Journal of Materials Processing Technology, Elsevier, vol. 123 (2002) p. 197-202.

Lee D.N. & Kim H.S., Plastic yield behavior of porous metals, International Journal of Powder metallurgy, vol. 35 (1992) p. 275.

Lee J. *et al.*, A study on flash and flashless-precision forging by the upper-bound elemental technique, International Journal of Materials Processing Technology, Elsevier, vol. 72 (1997) pp. 371-379.

Lee P.W. & Kuhn H.A., powder metallurgy forging, ASM Source Book on Powder Metallurgy, Compiled by Bradbury S., Ohio, US, 1979, pp. 410-418.

Lewis R.W. & Khoei A.R., A plasticity model for metal powder-forming processes, International Journal of Plasticity, vol. 17 (2001) pp. 1659-1692.

Lindskog P., The effect of phosphorous additions on the tensile, fatigue and impact strength of sintered atomized iron powder, Source Book on Powder Metallurgy, ASM, 1979.

Lippmann H., On the dynamics of forging, Proceedings of the 7th International MTDR Conference, Birmingham, UK, 1966, p. 53-66.

Liu G. *et al.*, Explanation of the mushroom effect in the rotary forging of a cylinder, International Journal of Materials Processing Technology, Elsevier, vol. 151 (2004) pp. 178-182.

Majerus J.N. *et al.*, Quantitative comparison between precision closed-die forging-force data and computer simulations, Journal of Engineering Materials and Technology, ASME, vol. 114 (October-1992) p. 465-471.

Manisekar K. & Narayanasamy R., Phenomenon of barrelling in square billets of aluminium during cold upset forging, International Journal Advanced Manufacturing Technology, vol. 21 (2003) pp. 84-90.

Marciniak Z., Rotary upsetting of flanges in warm forming temperature range, Proceedings of 3rd International Conference on Rotary Metal Working Processes, Japan, 1984, pp. 23-30.

Marx J.B. *et al.*, Some considerations of the hot forging of powder preforms, International Journal of Advanced Machine Tool Design and Research, Pregamon, vol. 10 (1971) p. 456.

Matsumoto H., The powder metallurgy industry in America, International Journal of Powder Metallurgy and Technology, vol. 14/2 (1978) pp. 135-144.

Miska K.H., Aluminium powder forged parts are strong and economical and they save weight, ASM Source Book on Powder Metallurgy, Compiled by Bradbury S., Ohio, US, 1979 p. 45.

Montgomery D.C., Design and analysis of experiments, John Wiley & sons, New York, USA, 1976.

Morgan W.R. *et al.*, Isostatic compaction of metal powders, Metals and Materials, Vol. 3, No. 5 (1969) p. 85.

Morimoto K. *et al.*, Transmission gear by powder forging, Modern Development in Powder Metallurgy, Princeton, vol. 7 (1974) p. 323.

Myers R.H., Response Surface Methodology, Allyn and Bacon, Boston, USA 1971.

Nakagawa T. *et al.*, Cold forging of ferrous powder metallurgy billet, Proceedings of the 27th Symposium of Japan Society of Powder and Powder Metallurgy, Tokyo, Japan, 1971, pp. 278-290.

Nakagawa T. *et al.*, On the cold forging of sintered iron powder preforms, Proceedings of the 13th International MTDR Conference, Birmingham, UK, 1972, pp. 455-461.

Negm M. & Davies R., The hot extrusion of metal powder preforms, Proceedings of 15th International MTDR Conference, Birmingham, UK, 1974, p. 637.

Nishino Y. *et al.*, Elimination of sintering steps in powder metallurgy hot forging process, Modern Development in Powder Metallurgy, Princeton, vol. 9 (1976) p. 509.

O'Connell M. *et al.*, Flashless closed-die upset forging-load estimation for optimal cold header selection, International Journal of Materials Processing Technology, Elsevier, vol. 59 (1996) p. 81.

Osakada K. *et al.*, Mechanical properties of mild steel after cold and warm high-speed forging, Proceedings of the 12th International MTDR Conference, Birmingham, UK, 1971, p. 357-362.

Pietrocini T.W., Hot formed powder metallurgy applications, Modern Development in Powder Metallurgy, Princeton, vol. 7 (1974) p. 395.

Ranek M.N. *et al.*, Simulation of densification in powder metal forging, International Journal of Materials and Manufacturing, ASME, vol. 98 (1988) pp. 340-352.

Sagar R. & Juneja B.L., An upper bound solution for closed die forging of hexagonal shapes, International Journal of Machine Tool Design and Research, Pergamon, vol. 20 (1980) pp. 67-72.

Sagar R. & Juneja B.L., Open die forging of a four-sided irregular disc, International Journal of Machine Tool Design and Research, Pergamon, vol. 31 (1991) pp. 315-328.

Sahoo S.K. & Das N.S., Forging of a truncated cone: an upper bound analysis, Manufacturing Technology Today, CMTI, vol. 2/10 (October-2003) pp. 7-11.

Samolyk G. & Pater Z., Application of the slip-line field method to the analysis of die cavity filling, International Journal of Materials Processing Technology, Elsevier, Article in Press, 2004.

Shen G. *et al.*, Effect of flash dimensions and billet size in a closed-die forging of aluminum alloy part, Proceedings of XVII NAMRC, Ohio, May-1989, p. 34.

Shima S. & Oyane M., Plasticity theory for porous metals, International Journal of Mechanical Sciences and Engineering, ASME, vol. 18 (1976) pp. 285-291.

Shima S. *et al.*, The inter-relation between density and hardness in the isostatic compaction of powders, Proceedings of the 13th International MTDR Conference, Birmingham, UK, 1972, p. 471.

Shivpuri R., Past development and future trends in the rotary or orbital forging process, Journal of Material Shaping Technology, vol. 6 (1988) pp. 55-71.

Singh A. & Davies R., Preliminary investigations of the cold extrusion of powder preforms, Proceedings of the 13th International MTDR Conference, Birmingham, UK, 1972, pp. 450-453.

Singh S. *et al.*, A computer simulation technique to estimate die load and energy during sinter-forging process, Journal of Production Engineering, I. E. (India), vol. (2002).

Singh S. *et al.*, Sintered preforms adds better value to aerospace components, Journal of Aerospace Engineering, I. E. (India), vol. 82 (2001) pp. 1-6.

Squire P., Density relationship of iron powder compacts, Journal of Engineering Industry, ASME, vol. 171 (1947) p. 485.

Stahlberg H.U. & Keife H., A load model for closed-die forging of long components, Scandinavian Journal of Metallurgy, vol. 21 (1992) pp. 159-164.

Standring P.M. *et al.*, Theoretical investigation and analysis: powder compaction and sinter forging, Journal of Mechanical Working Technology, Elsevier, vol. 4 (1980) pp. 7-29.

Stein E.M. *et al.*, High velocity compaction of iron powder, Metal Progress, vol. 85 (April 1964) p. 83.

Stranding P.M. & Appleton E., The kinematic relationship between angled die and workpiece in rotary forging, Proceedings of 1st

International Conference on Rotary Metal Working Processes, London, UK, 1979, pp. 275-288.

Subarao V.V. *et al.*, Powder metallurgy for automotive components: status of research and development in Indian industry, Powder Metallurgy: Automotive Application, Oxford IBH, 1998.

Suh S.K. & Kuhn H.A., Fracture modes and their prevention in powder metallurgy preforms, Modern Development in Powder Metallurgy, Princeton, vol. 9 (1977) p. 407.

Sutradhar G. *et al.*, Closed die axi-symmetric forging of sintered aluminium preforms, International Journal of Materials Processing Technology, Elsevier, vol. (1997).

Sutradhar G. *et al.*, Cold forging of sintered iron-powder preforms, International Journal of Materials Processing Technology, Elsevier, vol. (1995).

Sutradhar G. *et al.*, Cold forging of sintered polygonal discs, Journal of Production Engineering, I. E. (India), vol. 76 (1995) pp. 148-152.

Tabata T. & Masaki M., A yield criterion for porous metals and analysis of axial compression of porous discs, Memories of Osaka Institute of Technology, Series-B, Science and Technology, vol. 22, No. 2 (1978) p.45.

Tabata T. & Masaki M., A yield criterion for porous metals and analysis of axial compression of porous discs, Memories of Osaka Institute of Technology, Series-B, Science and Technology, vol. 22, No. 2 (1978) p.45.

Tabata T. & Masaki M., Plain strain extrusion of porous materials, Memories of Osaka Institute of Technology, Series-B, Science and Technology, vol. 19, No. 2 (1975) p. 78.

Tabata T. & Masaki S., A compression test to determine the coefficient of friction in forging powder metallurgy preforms, International Journal of Powder Metallurgy and Powder Technology, vol. 16/2 (1980) p. 149.

Tabata T. & Masaki S., Determination of the coefficient of friction in forging of porous metals from ring compression, Journal of Mechanical Sciences and Engineering, ASME, vol. 20, No. 8 (1978) p. 505.

Tabata T. & Masaki S., Estimation of flow stress of porous sintered metals from hardness test with pyramidal and spherical indenters,

Journal of Engineering Materials and Technology, ASME, vol. 112 (January-1990) pp. 95-98.

Takemasu T. *et al.*, Investigation of metal flow and preform optimization in flashless forging of a connecting rod, International Journal of Materials Processing Technology, Elsevier, vol. 59 (1996) p. 95.

Tengzelius J. and Blande C.A., High temperature sintering of powder metallurgy steels, Proceedings of Europe International Powder Metallurgy Conference, Florence, June-1982, p. 331.

Thomas J.T., A new yield function for compressible powder metallurgy materials, International Journal of Mechanical Sciences and Engineering, ASME, vol. 26 (1984) pp. 527-535.

Tiwari H.N. *et al.*, Forgeability evaluation of iron powder preform, Proceedings of 10th International MTDR Conference, Durgapur, India, December-1982.

Tobias S.A. *et al.*, The effect of impact speed and lubricant in hot forging: Part 1. Interface friction and die cavity pressure, Proceedings of the 9th International MTDR Conference, Birmingham, UK, 1968a, pp. 341-346.

Tobias S.A. *et al.*, The effect of impact speed and lubricant in hot forging: Part 2. Metal flow and forging loads, Proceedings of the 9th International MTDR Conference, Birmingham, UK, 1968b, pp. 347-350.

Vitvaz P.A. & Roman O.V., Impulse compacting of powder materials, Proceedings of the 13th International MTDR Conference, Birmingham, UK, 1972, pp. 442-447.

Wang G., Simulation and analysis of rotary forging a ring workpiece using finite element method, Finite Elements in Analysis and Design, vol. 38 (2002) pp. 1151-1164.

Wang J.C. *et al.*, Theoretical analysis of powder compaction and density distribution in long parts, International Journal of Powder Metallurgy, vol. 37 (1981) p: 371.

Wang P.T. & Zaidi M.A., Thermomechanical deformation of powder-based porous aluminium: part I. Evolution of pore structure, International Journal of Powder Technology, vol. 66 (1991a) pp. 9-19.

Wang P.T. & Zaidi M.A., Thermomechanical deformation of powder-based porous aluminium: part II. Constitutive model including

densification and hardening, International Journal of Powder Technology, vol. 66 (1991b) pp. 21-32.

Wang S. & Davies R., Some effects of high speeds in metal powder compaction, proceedings of the 9th International MTDR Conference, Birmingham, UK, 1968, pp. 331-340.

Ward M. & Biullington J.C., Effect of zinc stearate on apparent density, mixing and compaction and ejection of iron powder compacts, International Journal of Powder Metallurgy, No. 4 (1979) p. 201.

Weaver C.H. *et al.*, Hot rolling behavior of iron powder preforms, ASM Source Book on Powder Metallurgy, Compiled by Bradbury S., Ohio, US, 1979, pp. 99-110.

Wisker J.W. & Johns P.K., The economics of powder forging relative to competing processes-present and future, Modern Developments in Powder Metallurgy, Princeton, vol. 7 (1974) p. 33.

Zape G., The mechanical properties of hot pre-compacted iron-nickel sintered alloys, International Journal of Powder Metallurgy, vol. 13, No. 26 (1970) p. 130.

Zhang M., Calculating force and energy during rotating forging, Proceedings of 3rd International Conference on Rotary Metal Working Processes, Japan, 1984, pp. 115-124.